ABSTRACT

REN, DEYAO. Laser Micromachining and Its Applications in Manufacturing of Micro Medical Devices. (Under the direction of Dr. Yuan-Shin Lee and Dr. Roger Narayan.)

As the scale of manufacturing goes smaller and smaller, micro-scale or even nano-scale manufacturing becomes a trend in many applications. Laser micromachining is a good candidate for micro-scale manufacturing. The resolution of laser micromachining can be as small as the wavelength of the laser. It is capable of fabricating accurate structures in micro-scale. Biomanufacturing needs biocompatible materials and special processes to avoid contamination during manufacturing process. As a contactless manufacturing process, laser micromachining is also a good choice for biomanufacturing. Thus, laser micromachining has great potentials in micro-scale biomedical applications. However, compared with conventional manufacturing processes, laser micromachining has lots of special issues to be addressed. First of all, laser micromachining is a material-dependent process. Different materials show different machining performances in laser micromachining. Due to irregular cutting shape and laser energy profile, machined surface errors in laser micromachining are not as straightforward as in conventional manufacturing processes.

In this research work, we will develop the machining parameters for three biocompatible polymers: poly (methyl methacrylate) (PMMA), polydimethylsiloxane (PDMS) and high density polyethylene. The effects of different laser energy, number of laser pulses per area and machining surfaces on the cutting parameters (cutting depth and width) and machining performances will be studied.

Based on the developed machining parameters, machined surface errors will be analyzed. The laser energy profile will be introduced. The sources of machined surface errors in laser micromachining will be discussed. An analytical model to calculate the machined surface errors considering the overlapping effects between two adjacent laser trajectories will be proposed. The experiment and simulation results show the model can accurately calculate and predict the machined surface errors.

Unlike conventional manufacturing process, in biomanufacturing the manufacturing techniques need to be integrated with living biological species to perform biomedical functions. In this work, an integrated biomanufacturing system will be proposed for design and manufacturing of biomedical devices in micro scale. In this proposed integrated biomanufacturing system, based on materials, input design and functional requirements, laser parameters can be selected according to our machining parameter development to achieve desirable geometric features. The process planning can be performed based on our machined surface error analysis model and input tolerance. Microstructures fabricated by the laser micromachining can be used in manufacturing of biomedical devices. Design and manufacturing of several types of biomedical devices will be discussed in this work.

Proteins play an important role in biomedical research. The interaction of Bovine Serum Albumin and laser micromachined polymer surfaces will be analyzed. With the capability of fabricating microstructures by laser micromachining and adsorption of proteins on laser micromachined surfaces, microstructures can be fabricated to guide the adherence and adsorption of protein on material surfaces. Since some proteins can facilitate cell attachment and growth, this kind of devices may be used as bio-interfaces or delivery tools to provide protein supply.

Electrical properties are usually interpreted as indicators for biosensors to detect and measure biological activities. Design and manufacturing of portable biomedical devices to characterize electrical properties of biological species will be discussed. The electrical properties of magnetotactic bacteria will be characterized by using this device.

In the general, this research work will discuss the laser micromachining techniques and explore the applications of laser micromachining in design and manufacturing of biomedical devices in micro scale. At the end of this work, future research work will be discussed.

Laser Micromachining and Its Applications in Manufacturing of Micro Medical Devices

by
Deyao Ren

A dissertation submitted to the Graduate Faculty of
North Carolina State University
in partial fulfillment of the
requirements for the Degree of
Doctor of Philosophy

Industrial Engineering

Raleigh, North Carolina

2009

APPROVED BY:

_____	_____
Dr. Yuan-Shin Lee Chair of Advisory Committee	Dr. Roger Narayan
_____	_____
Dr. Robert E. Young	Dr. Thomas L. Honeycutt

DEDICATION

To my parents, Huaxia and Shangbang

BIOGRAPHY

Deyao Ren was born in Henan province in China in 1979. He is a PhD student in the Edward P. Fitts Department of Industrial and Systems Engineering at North Carolina State University, USA. He received his B.S. and M.S. degree in Mechanical Engineering from Huazhong University of Science and Technology, Wuhan, Hubei, P.R. China. His research areas include laser micromachining and its applications in manufacturing of biomedical devices, Computer-aided Design and Manufacturing (CAD/CAM), 3D modeling for design, manufacturing and bio-science, database applications in manufacturing industries, and haptic interfaces for education, design, manufacturing and medical simulations.

ACKNOWLEDGEMENTS

I would like to express my deep appreciation and gratitude to my advisors, Dr. Yuan-Shin Lee and Dr. Roger Narayan for their patience, suggestion and encouragement during my academic and research work at North Carolina State University. Without their guidance and continuous support, I would never have finished my study. I would like to thank Dr. Robert Young and Dr. Thomas Honeycutt for their support and service on my PhD dissertation Committee.

I greatly appreciate, and would like to thank, my research group members or former research group members: Yingjie Li, Apichart Boonma, Plawut Wongwiwat, Eui Seok Kim, Ronald L. Aman, Shiyong Lin, Dr. Yongfu Ren, and Dr. Susana K. Laiyuen, for their valuable consultation, suggestions, advice and help during my research.

Finally, I greatly appreciate my parents for their love, encouragement and support.

TABLE OF CONTENTS

LIST OF FIGURES

LIST OF TABLES

CHAPTER 1

INTRODUCTION

1.1 Motivations

Human being has benefited from manufacturing for thousands of years. Nowadays, the scale of manufacturing has gone to smaller and smaller. Micro-scale or even nano-scale manufacturing is making something impossible into possible, making something you cannot image into reality, just like hundreds of years ago people couldn't image we can fly in the sky.

As one of the areas driving manufacturing to this direction, biomamufacturing has huge potentials and applications. Same as other manufacturing, material and process are two key issues in biomanufacturing. Biocompatible materials, which can be used in living tissue environment with no or little harm to human body, are the typical materials in manufacturing for biomedical applications. Avoiding contamination becomes one of the most important factors in process consideration other than process capability.

Laser micromachining is a contactless process. Its resolution could be as small as the wavelength of the laser theoretically and can reach to tens of microns easily. Laser micromachining has an extensive material selection including metals, ceramics and polymers. Polymers show the best machining performances in laser micromachining. Also polymers own the best biocompatible properties among these three categories. These merits make laser micromachining a natural candidate for micro-scale manufacturing, especially for biomedical applications. So the research of laser micromachining on polymers for biomedical application is worthwhile and meaningful.

1.2 Research Scope and Objectives

There are many research topics in laser micromachining ranging from fundamental

research on laser ablation mechanism to advanced laser system development. Our work will focus on the laser micromachining for prototyping and manufacturing purpose, machined surface error analysis in laser micromachining and their applications to fabricate micro medical devices. Three issues will be addressed in this work.

1) **Machining parameter development**

Due to the material-dependent cutting performance in laser micromachining, machining parameters are needed to be developed for each individual material for prototyping and manufacturing. In this work, we will develop machining parameters via our lab-built excimer laser system for three biocompatible polymers: poly (methyl methacrylate) (PMMA), polydimethylsiloxane (PDMS) and high density polyethylene. The relationship between laser parameters and machining parameters will be built for prototyping and manufacturing purposes.

2) **Machine surface error analysis**

In manufacturing, the machined surface quality is one of the key issues for product realization. Compared with traditional machining process, there are some new problems to be addressed in laser micromachining. The machined surface errors will be analyzed and calculated. This can assist the process planning for laser micromachining.

3) **Design and manufacturing of biomedical devices in proposed integrated biomanufacturing system**

In biomanufacturing , structures with desirable geometric feature have to be integrated with biological tissues to perform biomedical functions. Design and manufacturing of several biomedical devices will be discussed. Adsorption of protein on laser micromachined surfaces will be studied. Biomedical devices that can be used to guide adherence and growth of protein and deliver protein will be discussed. A biosensor to measure electrical properties of magnetotactic bacteria will be also introduced.

1.3 Dissertation Organization

This dissertation consists of eight chapters. The remaining of this dissertation is organized as follows:

- *Chapter 2* Literature review: in this chapter, the related work will be reviewed including the research in laser micromachining, materials used for biomanufacturing, CAD/CAM systems in laser micromachining, design and machining process in biomufacturing.
- *Chapter 3* Machining parameter development of Laser micromachining on biocompatible polymers for prototyping and manufacturing: machining parameters will be developed in this chapter for manufacturing purposes on three biocompatible materials. The effects of laser energy, machining surfaces, number of laser pulses per area on machining parameters (cutting depth and width) will be studied.
- *Chapter 4* Machined surface error analysis in laser micromachining: in this chapter, the machined surface errors in laser micromachining will be analyzed. The sources of machined surface errors will be introduced. A numerical model is proposed for analysis and calculation of machined surface errors.
- *Charter 5* Integrated biomanufacturing system for micro medical devices based on laser micromachining: an integrated biomanufacturing system utilizing laser micromachining and biological species to fabricate micro biomedical devices will be proposed based on the techniques we present earlier. The modules and their functionality in this system will be discussed in this section.
- *Chapter 6* Adsorption of bovine serum albumin on laser micromachined material surface and its application in biomedical devices: adsorption of BSA on laser micromachiend polyethylene and PDMS surfaces is analyzed by Energy-dispersive X-ray spectroscopy on Scanning Electron Microscope and fluorescent images. With the ability of adsorption of protein on laser micromachiend surfaces, biomedical devices will be fabricated to guide the growth and adherence of protein. They can be also used as delivery devices to carry protein solution from reservoir to desirable spots.
- *Chapter 7* Design and manufacturing of biomedical devices to characterize electrical properties of biological species: a biomedical device to characterize the electrical properties of biological species will be discussed. Electrical properties of

magnetotactic bacteria will be measured in this device.

- *Chapter 8* Conclusions and future work: conclusions will be drawn and future research work will be discussed.

CHAPTER 2

LITERATURE REVIEW

In this chapter, we will review the literatures in laser micromachining including the fundamentals of laser micromachining, its capabilities and application, materials used in laser micromachining, numerical modeling for laser ablation, CAD/CAM tools for laser micromachining, biocompatible materials and the research work in biomanufacturing.

2.1 Laser Micromachining

Micro-scale manufacturing has been a popular trend for manufacturing technologies as various industries develop including telecommunication, biomanufacturing , MEMS and more and more demands for biomedical applications in manufacturing. In those industries, sub-micrometer or even smaller resolution in manufacturing is required. Not only scale, some other factors are also of great importance such as cleanness, contamination during process, biocompatibility and so on. New materials and processes are definitely necessary to be developed for those new manufacturing requirements. Laser is one of these new tools that are ideal for micromachining and drew more and more research interests.

2.1.1 Definition of laser micromachining

Laser micromachining is based on the removal of material with short but intense laser pulses. Specific patterns, surface patterns or 3D structures, can be achieved by controlling motion of parts or mask image projection. In general typical feature seizes are in the order of micrometer. The scope of laser micromachining covers non-ablative process such as laser etching in a chemical active medium and pulsed laser ablation. In this research, our discussion is based on laser ablation micromachining. The laser ablation refers the removal

of material due to interaction between materials and strong laser irradiation.

2.1.2 Mechanism of laser ablation

In one word, ablation is due to the absorption of laser energy into the materials. When a laser beam is being shot onto the material surface, an electromagnetic wave enters material and the material will absorb some radiation by vibration or electronic excitations. If the fluence of the laser beam shooting onto the material surface is high enough to reach or surpass some threshold value (F_{th}) which is required for materials to decompose, the material decomposition will occur. Since the duration of laser pulse is very short (in ns range or less), the decomposition process will also happen in very small time frame comparable with one laser pulse. Material particles are ejected from material surface during decomposition. Some ejected particles will then redeposit around the ablated areas.

According to the Beer-Lambert law, beam intensity will drop exponentially along the propagation path inside materials. Beer-Lambert law can be described as follow when $F_0 \geq F_{th}$:

$$F(x) = F_0 e^{-\alpha x} \tag{2.1}$$

where: F_0 (w/cm^2) is the initial beam intensity;

α (cm^{-1})is the absorption coefficient;

x (cm) is the depth below the material surface (cm).

Beer-Lambert law is assuming a 1-photon absorption process. With assumption of linear absorption, it is valid for by most materials over a limited range of fluences. Some much more complex models have been discussed considering thermal diffusion, moving of ablation interface, plume absorption, material properties changing during ablation, incubation and precursor effects. Although those models are trying to explore the ablation mechanism as accurately as possible and are good for us to totally understand the ablation process, more complex models are far beyond our discussion since Beer-Lambert law is still a good approximation to describe the laser ablation. In Beer-Lambert law, α depends on the material properties including thermal absorption of material and its thermal conductivity. The laser

wavelength, pulse duration, intensity and material properties are main factors to determine the machining performance.

Based on Beer-Lambert law, we can calculate the etched depth given a material and laser beam influece. Since ablation only occurs if a minimum pulse fluence F_{th} is reached, the etch depth d when $F > F_{th}$ is

$$d = \frac{1}{\alpha} \ln((1 - R)\frac{F}{F_{th}}) \qquad (2.2)$$

where R is the reflective percentage of the laser intensity. The ablation will automatically stop at the depth where the local fluence drops below F_{th}.

It is generally accepted that two phenomena happen during the ablation process: photochemical ablation and photothermal ablation [Paterson, 1999]. Photochemical ablation means the absorbed photons leading directly to bond breaking in the material without any intermediate heat dissipation. In photothermal ablation, deposited energy will be converted to heat and decomposition happens since heating vaporizes materials.

According to the Beer-Lambert law, for materials with low F_{th}, ablation can happen easier under lower laser radiance. Low absorption rate α will result in deeper ablation depth. F_{th} and α depend on material properties. High ablation rates can be achieved for materials with low α at sufficiently high fluence.

2.1.3 Advantages and applications of laser micromachining

Laser micromachining is a contactless process. It will not damage material surface except the pile-up effects for metal materials, debris redeposition for polymers and cracks due to additional heating stress. But those effects can be avoided by some pre-process, post-process and deliberately setting machining conditions. The laser micromachining can be operated under atmospheric condition and at room temperature. Due to the contactless characteristics, there is no tool wearing in laser micromachining like conventional machining methods. Also laser machining is suitable for rapid prototyping even with complex geometric patterns because of its flexibility.

Pulsed laser can reach peak irradiance over the ablation threshold in very short time. So

the ablation happens in a very short time. For materials with high absorption rate, the energy is spatially confined in a very thin layer beneath the surface. Also, part of the energy leaves the material surface along with the ejected material particles. These factors determine that heating will not damage the areas surrounding the ablated cavity.

The applications of laser micromachining could include but not constrain to laser via drilling in PCBs, laser-assisted chemical etching, laser-LIGA, wiring of Fiber Bragg grating, photopolymerization, microlenses fabrication, UV lithography, waveguide writing in galss with ultrafast lasers, inkjet nozzle drilling, ablation of fluid capillaries for lab-on-chip purpose, refractive surgery, fiber and wire stripping and pulse laser deposition.

2.1.4 Laser beam shape and its energy profile

There are many types of lasers with different gases available in the market including high power infrared Nd: YAG and CO_2 lasers which are mainly used in industry and excimer lasers which emit in the UV range 157-355 nm depending on gases. The most commonly used gases for excimer lasers are ArF in 193nm and KrF in 248nm. Other gases include F_2 in 157nm, XeCl in 308nm and XeF in 351nm. The parameters regarding to laser include pulse energy ($E[mJ]$), fluence ($F=E/Spot\ [J/cm^2]$), intensity ($I[W/cm^2]$), pulse length ($\tau[ns]$), repetition rate ($f[Hz]$), output power ($P=fE[W]$), wavelength ($\lambda[nm]$), and beam quality (M^2). For UV lasers which are operated with pulses of nanosecond duration, the ablation is a photochemical process with little photothermal phenomenon. While for high power lasers such as CO_2 lasers, the ablation always happens in both ways. Compared with CO_2 lasers, UV-lasers can generate smaller structures due to the smaller wavelength. Another advantage of UV laser is that heat effects are confined in a very limited volume since only part of ablation happens due to photothermal phenomenon and pulse duration is very short.

One big concern about the laser is the shape and energy profile of output laser beam. The shape and energy profile of laser beam directly determine the shape of etched cavity. The structure of cavities, just like the cutter shape in conventional machining, will have effects on process planning and surface finishing. Some lasers including CO_2, Copper vapor, Ti: Sapphire and Nd: YAG emit normally distributed or nearly normally distributed circular

beam. The energy profile of the laser beam is shown in Fig.2.1(a) like a bell-shape curve. The fluence on the energy profile can be approximately defined as:

$$F = F_{\max} e^{-\frac{x^2}{2\sigma^2}} \tag{2.3}$$

where F is the fluence on one point of the curve;

F_{max} is the maximal fluence in this laser beam;

x is the x value along one direction on the cross section of laser beam in Fig.2.1(a);

σ is the range that laser beam spread over. In this case $\sigma = \frac{x_{\max} - x_{\min}}{6} = D/6$, where D is the diameter of the laser beam.

For these lasers, the laser beam can be focused to a very small spot. It's flexible to control and make complex geometric patterns. However, due to the small spot, it is very time-consuming when you are trying to machining large areas which need bulky materials removed.

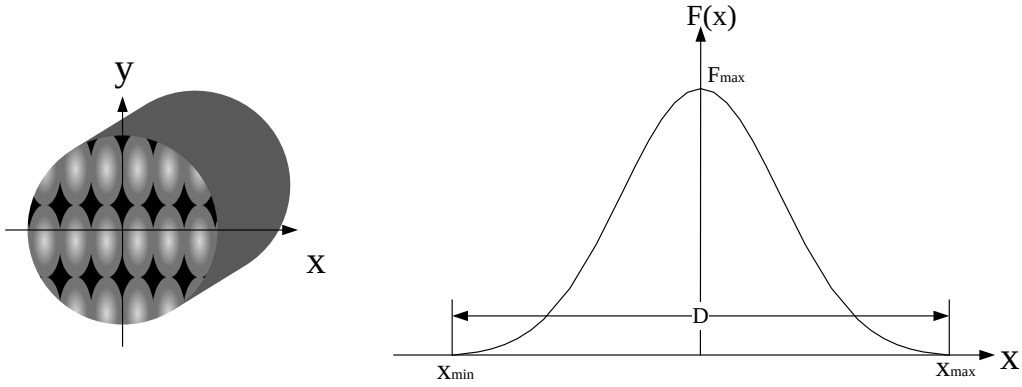

(a) Laser beam (b) Normally distributed energy profile

Fig.2.1 Laser beam and normally distributed energy profile

For TEA CO_2 and excimer laser, the shape of the beam is a rectangle and the energy profiles in two directions are different. In one direction the energy profile is normal distribution or like normal distribution. In the other direction, the energy profile can be approximately described as the top-flat function as equation (2.4).

$$F = \begin{cases} F_{\max} & x^- \le x \le x^+ \\ F_{\max} e^{-\frac{(x-x^-)^2}{2\sigma^2}} & x_{\min} \le x \le x^- \\ F_{\max} e^{-\frac{(x-x^+)^2}{2\sigma^2}} & x^+ \le x \le x_{\max} \end{cases} \tag{2.4}$$

where $\sigma = \frac{x_{\max} - x^+}{3} = \frac{x_{\min} - x^-}{3}$. With this type of energy profile, the laser beam can not be focused on one small circular spot but a rectangular-like shape with oval on both ends. So it is difficult to machine complex geometry. However, it's suitable to remove material in large areas due its relative large focused beam size. For some channels or reservoir patterns this laser beam and energy profile even naturally fit.

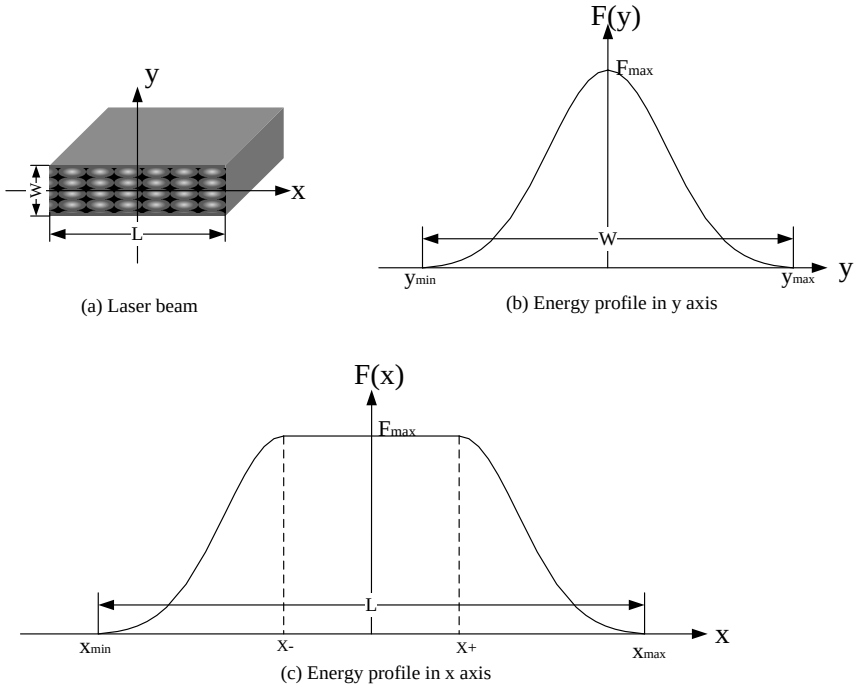

Fig.2.2 TEA CO_2, excimer laser beam and energy profile

Since the laser beam with multimodal energy profile is not favorable for complex geometric patterns and normally distributed energy profile is time-consuming for bulky material removal, some homogonous optical devices are utilized to make the energy distribute more evenly and take advantage of both energy profiles. Beam homogenizer is one

of those devices. It can change energy profile in a laser beam to a more evenly distribution almost without much energy loss via reducing the standard deviation of laser energy over the beam area. Homogenizers split up the beam and then superimpose them in the mask plane by using optical devices. The homogenized energy profile is very similar to top-flat function in equation (2.4) but more evenly distributed with large flat area. If aperture is utilized only to filter out the part of laser beam with evenly distributed energy, the side wall could be vertical. Thus, via homogenizer device, we can acquire well-formed circular focused spot with much more evenly distributed energy profile.

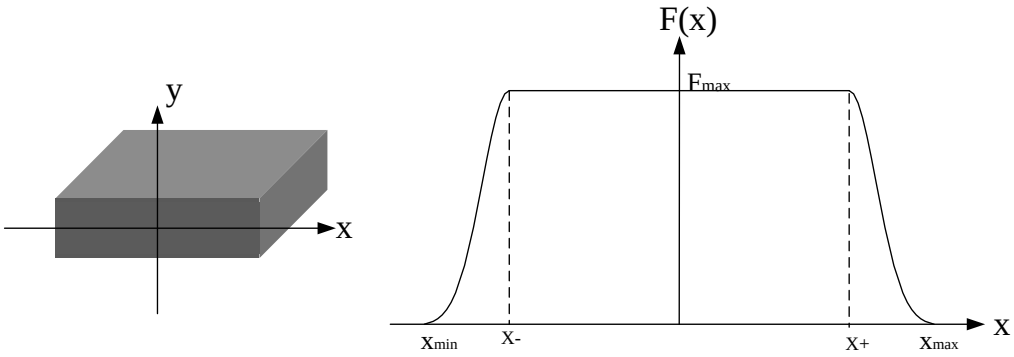

(a) Laser beam (b) Energy profile in both directions

Fig.2.3 Homogenized laser beam and energy profile

2.1.5 Laser delivery systems

Laser delivery systems for laser micromachining are to deliver the laser beam from the laser emitting source to machining platform under some specific requirements and spatial limitation. A basic laser delivery system consists of high reflective mirrors, lenses, apertures and objective lens.

HR mirror is to change the direction laser beam. To reduce the beam size without losing energy, a set of lenses with a positive and a negative lens separated by the sum of their focal lengths (FL_2+FL_1) can be put between laser source and machining platform. The output beam diameter reduces proportionally to FL_2/FL_1 and the beam fluence changes with a factor of $(FL_2/FL_1)^2$ correspondingly. Aperture is used to further reduce the laser beam size. However, it also reduces the laser radiance by block part of laser beam. Objective lens

focuses laser beam onto material surface to achieve high fluence. The demagnification of objective lens and the size of incoming laser beam determine the laser spot size onto material surface. Some other optical accessories include homogenizer, attenuator and so on.

A typical laser delivery system is illustrated in Fig.2.4.

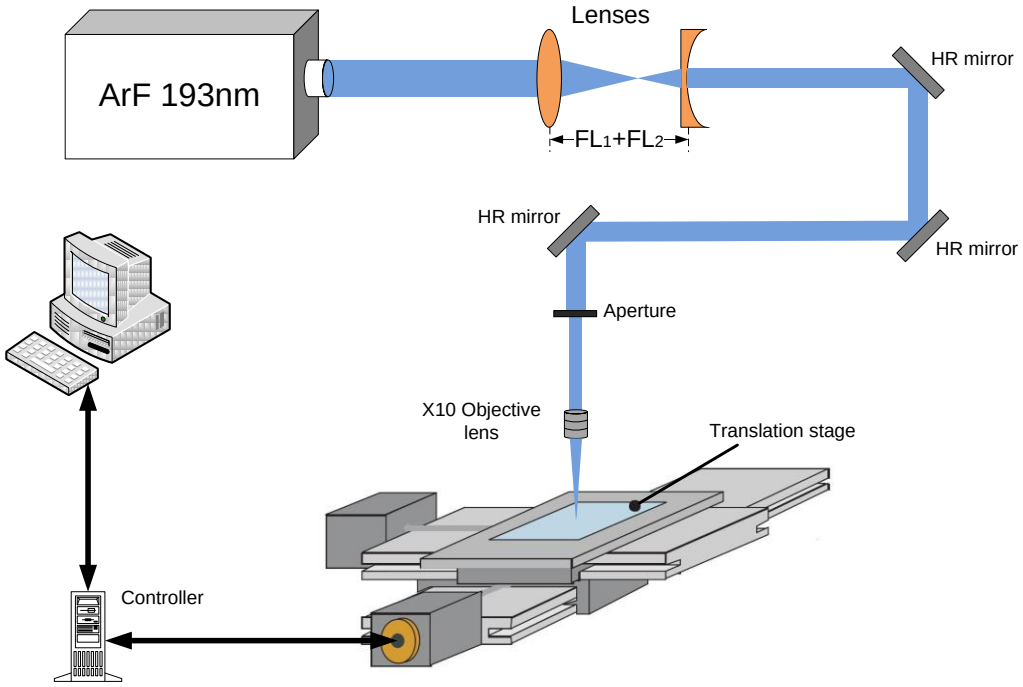

Fig.2.4 Lab-built laser micromachining system

2.1.6 Materials for laser micromachining

There are abroad materials available for laser micromachining including ceramics, glasses, organic materials, polymers, metals and semiconductors. This is one of the advantages of laser micromachining. The machining efficiency and quality of particular materials depend on reflectivity, absorption for particular wavelength, thermal conductivity, enthalpy of evaporation, bond energy, and defect density of those materials. Some criterion to evaluate the machining performance include smoothness of machined surfaces, damage to surrounding materials, depth of ablation, and the edge of ablation (e.g. pile-up effects).

A comparison of different materials in laser micromachining is shown in the following table.

Table 2.1 Comparison of machining performance of different materials for laser micromachining

Materials	Absorption	Thermal conduct	Reflectivity	Depth of ablation
Metals	High	High	High	Low, nm range
Semiconductors	High	High	High	Low, nm range
Ceramics	High(lower than metal)	Fair	High	Fair
Glasses	High(lower than metal)	Fair	High	Fair
polymers	High	Low	Low	Relative high, μm range

Materials	Edge effects	Surface quality
Metals	Bad, pileup effect, burr edge	Bad, melting effect on surface, recast
Semiconductors	Bad, pileup effect, burr edge	Bad, melting effect on surface, recast
Ceramics	Better than metal	Cracks due to stresses
Glasses	Better than metal	Cracks due to stresses
polymers	Good for excimer laser, redecomposition, no thermal damage	Good for excimer laser, redecomposition, no thermal damage

2.1.7 Strategies in laser micromachining

In general, there are two different strategies to make 3D or 2D patterns with complex geometric features. One is to use a specific mask having the same pattern of desired structure. The patterned mask is projected onto material surface. Via deliberately controlling the demagnifying factor, desired structuring can be achieved. The other strategy is to use simple patterned mask (e.g. aperture). This simple mask is scanned under specific motion determined the designed structure.

For 3D structures, we can achieve different ablation depth on different parts of materials either by controlling the pulse number in each area or by controlling the fluence of laser beam. However, it's hard to accurately control the energy level of laser beam or size of laser beam synchronously with motion of translation stage. Second approach is not feasible to implement.

2.2 Research on Laser Micromachining

There is lots of research in laser micromachining. Three of them are closely related to our work. First one is the numerical modeling to study the behavior of laser ablation to gain better understanding on laser micromachining. Due to the material-dependent machining performance, the study on different materials in laser micromachining is another popular topic in this area. To improve the accuracy and efficiency of laser micromachining, integrating the CAD/CAM into laser micromachining system shows its potentials in the future.

2.2.1 Numerical modeling of laser ablation process

Although laser micromachining has lots of advantages, its drawbacks impede its further applications. Due to the uncertain energy loss, irregular cutting shape, various cutting behaviors depending on different materials and equipments, and extremely complex phenomenon occurring in machining process, it is very hard to do quantitative analysis on the process of laser micromachining. However, the great potentials to have better understanding on laser micromachining attract many people working in this area. The numerical modeling research mainly includes two issues: the fundamental mechanism of laser micromachining and modeling on cutting behavior.

1) Numerical modeling on mechanism of laser ablation

Beer-Lambert law is generally accepted as the principle to guide the research in this area. But its limitation is assuming only 1-photon absorption occurs, absorption and etching happens separately and no heat conduction happens in the process. It is only valid in some range of laser fluence [Naessens 2003]. Some research focused on more precise description on the mechanism of laser ablation. In [Krajnovich 1997] a more accurate model considering the plume expansion was established. The plume expansion further reduces the laser fluence when laser propagates into materials. In [Naessens 2003, Srinivasan 1986 & Schmidt 1998], better models taking both thermal and non-thermal features into account in the ablation process were developed. The effect of laser pulse duration on the ablation process was

studied in [Taylor 1987]. Incubation effect was considered in the models in [Naessens 2003]. In [Gai 1992], authors studied the mechanism of interaction between laser radiation and materials. It exploited quantum mechanical process of ultraviolet photon absorption and molecular dynamics techniques to obtain a model for ablation of polymer surface. Their model shows repulsive antibonding electronic potential energy surfaces is crucial to understand the ultraviolet ablation process at 193 nm wavelength compared with other effects like intense local heating of material by longer wavelength lasers.

2) Numerical modeling on interaction of laser pulses and materials

The research mentioned above focused on the fundamental mechanism of laser ablation process. Some research worked on higher level to model the interaction of laser pulses and materials. [Kahiert 1992] is one of the earlier research on modeling of effects of laser illumination and image optics parameters on microstructure formed by laser pulses. In [Patterson 1999], a numerical model had been built to predict cutting behavior of the materials including cutting depth and wall angles of trench structure ablated. This two-stage model involved calculation of the radiation distribution incident on the surface of the partially formed structure and modeling of the ablation and removal of materials from the surface. This model considered the surface propagation by continuous laser pulses, which is normal in laser micromachining. The experimental results and predicted results had been compared. They agreed with each other very well except lowest and highest energy. In [Galantucci 1998], a simulation of laser cutting shape and size by means of a photo-ablation approach was developed. Experiments were performed to determine the threshold fluence and other material parameters.

2.2.2 Laser micromachining on different materials

Laser micromachining has extensive material selections including metals, ceramics and polymers. This is one of the reasons why laser micromachining are applied into so many areas. On the other side, due to the material-dependent parameters like absorption coefficient and threshold value and different thermal properties on materials, different materials show greatly various performances in laser micromachining. So many research studied the laser

cutting performance on different materials. Studies on different materials have been reported including polymers [Baudach 2000, Cheng 2004 & Klank 2002], silicon [Ren 2005 & Barsch 2003] and ceramics [Dear 2008]. In [Cheng 2004], the laser micromachining on PMMA by CO_2 has been study and thermal annealing was applied to improve the surface smoothness. Another study of CO_2 laser on PMMA was introduced in [Klank 2002] for rapid production of microfluidic systems. In [Roberts 1997] UV excimer laser micromachining on polystyrene, polycarbonate, cellulose acetate, and poly (ethylene terephthalate) by mask pattern was studied. In those work, the quantity relationship between laser ablation parameters and laser parameters for specific materials is rarely setup especially for manufacturing purpose.

2.2.3 CAD/CAM tools for laser micromachining

1) CAD/CAM systems for laser micromachining

Integrating the CAD/CAM into laser micromachining system shows great potentials and becomes more and more popular in laser micromachining. CAD/CAM can help laser micromachining discard the trial-error method to obtain desirable structure. Instead, a more efficient and accurate approach can be provided by CAD/CAM tools. In almost all the current laser micromachining system, basic CAD/CAM is carried. Along with high resolution controller, the CAD/CAM module in laser micromachining system, which generally accepts G-code as input, can provide accurate positioning and motion in a predefined pattern. Some advanced CAD/CAM tools and numerical models for CAD/CAM purpose are also developed for special uses. In [Choi, 2004], mask was utilized to control the laser energy shooting on material surface. Through the various sizes of holes on mask, different cutting depth can be achieved. A numerical model has been built to represent the relationship between size of holes on mask and cutting depth. So given a depth in 3 dimension, a hole diameter will be calculated on 2 dimensional mask based on numerical model. In [Mutapcic 2006], a CAD/CAM system for excimer laser micromachining was introduced. The function of CAD/CAM system is very similar to convention CAD/CAM system including importing standard CAD files, triangulation of object surfaces, slicing the CAD models and generating NC code for tool path and mask layout design. By exploiting the

system, authors studied the laser influence, pulse repetition frequency and the number of shots per area to optimize the wall angle and ablation depth. This paper also investigated the stitching error in laser micromachining. To minimize the stitching error, the overlap size was calculated and various shapes of masks were tested. In [Böhlen 2003], a CAD/CAM software has been developed that automatically generated the tool paths according to a CAD drawing of the MEMS device.

2) Machined surface error analysis in laser micromachining

In traditional CAD/CAM research, surface error analysis is one of the major parts of the work. Surface roughness is directly determined by surface errors. Surface error analysis can help the process planning decision. A systematic methodology was proposed in [Lee 1996&1997] for surface error analysis in 5-axis machining. This method provided a general solution for surface error analysis considering different cutter shapes, part surface geometry, and orientation of cutters. The machined surface error analysis in laser micromachining has not been fully addressed yet. The overlapping effects and stitched error were discussed in [Mutapcic 2003&2006]. In [Mutapcic 2003] machined surface errors caused by overlapping between two adjacent pulses for UV laser ablation on polycarbonate surfaces were studied. The overlay peak errors which are the materials left on part surfaces and overlay trough errors which are caused by penetration into part surfaces by laser pulses were investigated. The overlapping, wall angle, and number of shots per area are the main parameters to determine the peak and overlay errors. However, they didn't give a general numerical model to predict the machined surface errors for most natural laser energy profile. They also didn't consider the smaller number laser pulses per area. Their model needs lots of experiments to find the optimal parameters resulting in the minimal machined surface errors. In [Mutapcic 2006], they applied this method in a CAD/CAM tool.

2.3 Research on Biomaterial and Its Applications

2.3.1 Definition and properties of biomaterials

According to the definition in [Black 1992], a biomaterial is natural or man-made

material comprising whole or part of a living structure or biomedical device which performs, auguments, or replaces a natural function. As applied in implants and medical devices, biomaterials are used to replace or help to restore function of disease tissues or to facilitate the biomedical research.

A lot of factors are needed to be considered to select a biomaterial. Based on the specific application, to select chemically and biologically suitable material surface to host tissues, we can pick a bioinert material or bioactive one, biostable one or biodegradable one. Mechanical properties comparable with where the material will be used are also important for biomaterials. Due to the complex geometric requirements, ease for manufacturing is another increasing concern.

2.3.2 Comparison of different biomaterials

Numerous biomaterials can be divided into three categories: metals and alloy, ceramics and glasses, and polymers including synthetic and natural polymers [Ramakrishna 2001].

Metals and alloys used as biomaterials include gold, tantalum, titanium, stainless steel, Co-Cr, nitinol, Ti alloy and so on. Alumina, titania, zirconia, bioglass, carbon, hydroxyapatite (HA), and calcium phosphate are examples of ceramics and glasses. Metals and alloys have good mechanical strength, ductility and wear resistance but suffer low biocompatibility, high density and too high stiffness for biomedical applications. While ceramics and glasses are good in biocompatibility and resistance to corrosion and compression but they are very brittle with low fracture and low resilience and difficult to be fabricated. Polymers can be easily fabricated into complex geometry and have excellent biocompatibility. Numerous synthetic and natural polymers with various biocompatible properties are available for different biomedical applications. Although structural and mechanical properties are shortcomings for polymers, through deliberately designed volume fraction and reinforcement procedure favorable mechanical properties can be achieved by polymers composite materials for applications which need good strength [Lin 1997].

2.3.3 Application of biocompatible polymers

Due to development of polymer science and engineering, a wide variety of polymers and polymer composite materials have been developed for extensive biomedical applications [Ramakrishna 2001] including bone fracture repairing, joint replace, bone cement, bone replacement, dentistry (dental implants, dental restorative materials and dental prostheses [Salernitano 2003]), oral and maxillofacial surgery, functional load-carrying and supporting implants (tendons, ligaments and vascular grafts) [Ramakrishna 2001], and bulk space fillers. Except the implant applications, polymers are also used to developed medical devices such as drug delivery devices, ardiovascular devices and bone fracture internal devices [Salernitano 2003]. Good biodegradability or bioresorbability, ease to be fabricated, and favorable surface chemistry for cellular attachment of polymers make them very competitive candidates for scaffold materials to facilitate cellular growth in tissue engineering. Aliphatic polyesters such as polyglycolic acid (PGA),polylactic acid (PLLA), their copolymers (e.g. PLGA) and polycaprolactone (PCL) are the most commonly used polymers for tissue engineering scaffold applications [Sachlos 2003]. In [Liu 2004], Medpor porous polyethylene was applied in the skull implants. Compared with conventional materials used in surgery like methyle methacrylate, titanium mesh, the porous character of polyethylene allows rapid fibrovascular and soft tissue and bone ingrowth, which strengthens the implants and decreases the risk of defection.

2.4 Design and Machining Process for Medical Devices

2.4.1 Scope of biomanufacturing

Generally biomanufacturing includes biotechnology, whose activities focuse on or contribute to the use of living cells or their process to make product or solve problems, pharmaceutics and medical device. According to the definition from FDA, “A medical device is any healthcare product that does not achieve its principle intended purpose by chemical action or by being metabolized”. From the manufacturing perspective, the current research

focuses on implant design and manufacturing, tissue engineering and biomedical device.

2.4.2 Research on design of medical device

After many years development, implant design have improved from standard design [Ducheyne 1977, Bobyn 1982 & Tuner 1989] to customized design [Jajal 2003, Harrysson 2001 & 2007]. Customers' CT/MR scanning date can be imported to CAD software to be reconstructed into 3D models. The concept of custom-designed bone implants can be also seen in [Sathasivam 1999 & Thoma 2000]. In [Fang 2005], a multi-scale design scheme was developed for design of bone structure both in macroscopic and microscopic levels. A multi-scale voxel modeling approach was presented to model the bone structure both in macroscopic and microscopic levels. In [Harrysson 2007], standard-designed and custom-designed bone implants were analyzed and compared via Finite Element Analysis. In [Scharver 2004], a haptic interface was developed for implant model design, repairing and reconstruction.

2.4.3 Machining processes for fabrication of medical device

Any raw materials are needed to be shaped into particular geometric structures for specific applications to meet functional requirements. Generally there are three ways to manufacture complex geometric structures: CNC machining, molding and layer-based rapid prototyping. CNC machining and molding can produce complex structures with high surface finishing, dimensional accuracy and good mechanical property. Molding processes can be only cost-effective when production volume is large and suffer geometry constraints especially small geometric features. Design changes in molding process are expensive due to high setup cost of molds. Thus molding is not appropriate for the occasions that customized design is necessary. CNC machining is very flexible and capable of making complex geometric features, but it's only efficient for produce low production volume. Layer-based RP techniques can make complex geometric structures with low cost when production volume is low but poor surface finish and mechanical properties. Some procedures are

needed to apply during or after manufacturing processes to keep clean and avoid contamination. Each of these processes can apply into limited number materials, which becomes a factor to select manufacturing process. Those manufacturing process have been extensively used for biomedical applications. Some robotic systems have been developed for bone implants manufacturing [Fadda 1998, Pokrandt 1997]. A robotic system can perform complex cutting operations for freeform surfaces with tool path generated based upon CAD models. A 3-aixs CNC milling method for skull plant manufacturing was proposed in [Hieu 2002b]. Electron Bean Melting (EBM) was employed in [Harrysson 2003] for bone implants manufacturing by Titanium (Ti6A14V). In [Suwanprateeb 2006] a 3D printing process was developed to fabricate the bone implants using porous polyethylene. In [Fang 2005], a direct-fabrication process planning was also developed based on their proposed voxel model of bone structure. Since those approaches are contact processes, contamination should be avoided in those processes. In [Suwanprateeb 2006] a 3D printing process was developed to fabricate the bone implants using porous polyethylene. A contactless process will be very attractive for biomedical applications. Laser micromachining is one of the contactless processes. Although the machining capability is limited for laser micromachining, it offers great advantages especially in micro scale compared with those process mentioned above which are not capable of or difficult for generating such small geometric features.

2.5 Summary

In this chapter, we reviewed the related work in laser micromachining, biomaterials and their applications, and the design and machining process for medical devices. Some research focused on the machining performance on different materials and modeling for laser ablation. However, the research on machining performance is rarely for manufacturing purpose and it is still lack of number models to analyze the machined surface errors in laser micromachining. In the following chapters, we will develop the machining parameters on biocompatible polymers for prototyping and manufacturing purposes and propose a numerical model to calculate the machined surface errors in laser micromachining.

CHAPTER 3

MACHINING PARAMETER DEVELOPMENT OF LASER MICROMACHINING ON BIOCOMPATIBLE POLYMERS FOR PROTOTYPING AND MANUFACTURING

Laser micromachining has been extensively applied in many areas. With its contactless and flexible characteristics, laser micromachining is an attractive technique for rapid prototyping in biomedical applications. In this chapter we will try to develop a flexible scheme for rapid prototyping via laser micromachining integrated with CAD/CAM technologies. Three biocompatible polymers, poly (methyl methacrylate) (PMMA), polydimethylsiloxane (PDMS) and high density polyethylene, have been studied for this purpose. The effects of laser fluence, laser beam dimension, and number of laser pulses per area on laser cutting performance have been experimentally analyzed. This chapter provides a fundamental platform for rapid prototyping and manufacturing.

3.1 Introduction

3.1.1 Materials for biomedical applications

As the progress made by medical practice, more and more materials are utilized for biomedical purposes especially for implants and medical devices. According to the definition in [Black 1992], a biomaterial is natural or man-made material comprising whole or part of a living structure or biomedical device which performs, auguments, or replaces a natural function. As applied in implants and medical devices, biomaterials are used to replace or help to restore function of disease tissues or to facilitate the biomedical research.

1) Properties of biomaterials for biomedical applications

Although many aspects should be considered to select one material for a particular application, due to the fact that biomaterials perform their function inside living bodies or interact with biological tissues and medium, biocompatibility becomes a vital criterion to evaluate the performance of biomaterials. Biocompatibility means the ability of a biomaterial to perform its desired functions with respect to a specific application without having toxic or injurious undesirable effects on the recipient or beneficiary biological systems [Williams 1999 & 2000]. Based on the specific application, to select chemically and biologically suitable material surface to host tissues or medium, we can pick a bioinert material or bioactive one, biostable one or biodegradable one. Except biocompatible properties, mechanical properties comparable with intended sites where the material will be used are also important for biomaterials. Due to the complex geometric requirements, ease for manufacturing is another increasing concern. Numerous biomaterials can be divided into three categories: metals and alloy, ceramics and glasses, and polymers including synthetic and natural polymers [Ramakrishna 2001].

2) **Comparison of different categories of biomaterials**

Metals and alloys have good mechanical strength, ductility and wear resistance but suffer low biocompatibility, high density and too high stiffness for biomedical applications. While ceramics and glasses are good in biocompatibility and resistance to corrosion and compression but they are very brittle with low fracture and low resilience and difficult to be fabricated. Polymers can be easily fabricated into complex geometry and have excellent biocompatibility. Numerous synthetic and natural polymers with various biocompatible properties are available for different biomedical applications. Although structural and mechanical properties are shortcomings for polymers, through deliberately designed volume fraction in synthetic polymers or proper reinforcement procedure favorable mechanical properties can be achieved by polymers composite materials for applications which need good strength [Lin 1997].

3) **Biocompatible polymers and their applications**

Due to development of polymer science and engineering, a wide variety of polymers

and polymer composite materials have been developed for extensive biomedical applications [Ramakrishna 2001] including bone fracture repairing, joint replace, bone cement, bone replacement, dentistry (dental implants, dental restorative materials and dental prostheses [Salernitano 2003]), oral and maxillofacial surgery, functional load-carrying and supporting implants (tendons, ligaments and vascular grafts) [Ramakrishna 2001], and bulk space fillers. Except the implant applications, polymers are also used to develope medical devices such as drug delivery devices, ardiovascular devices and bone fracture internal devices [Salernitano 2003]. Good biodegradability or bioresorbability, ease to be fabricated, and favorable surface chemistry for cellular attachment also make polymers very competitive candidates for scaffold materials to facilitate cellular growth in tissue engineering. PGA, PLLA, PLGA and PCL are the most commonly used polymers for tissue engineering scaffold applications [Sachlos 2003].

3.1.2 Laser micromachining for biomedical applications

1) Advantages of laser micromachining for biomedical applications

Any raw materials are needed to be shaped into particular geometric structures for specific applications to meet functional requirements. As one of the contactless processes, laser micromachining is very attractive for some biomedical applications since contamination during the process is not a problem any more. Although the machining capability is limited for laser micromachining, it offers great advantages especially in micro scale compared with CNC machining, molding and layer-based rapid prototyping techniques which are not capable of or difficult for generating such small geometric features. Another merit of laser micromachining is the extensive material selections. Almost all of the materials including metals, ceramics and polymers are good for laser micromachining. Polymers show the best performance among those three categories in laser micromachining. As micro-sale manufacturing becomes a trend in various industries including biomedical applications, laser micromachining draws more and more attention from academia and industry.

2) **Mechanism of laser micromachining**

Laser micromachining is based on the removal of material with short but intense laser

pulse due to the absorption of laser energy into the materials. When a laser beam is being shot onto the material surface, if the fluence of the laser beam shooting onto the material surface is high enough to reach or surpass the threshold value (F_{th}) which is required for material to decompose, the material decomposition will occur. According to the Beer-Lambert law, beam intensity will drop exponentially along the propagation path inside materials. Beer-Lambert law can be described as follow when $F_0 \geq F_{th}$:

$$F(x) = F_0 e^{-\alpha x} \tag{3.1}$$

where: F_0 (w/cm^2) is the initial beam intensity;

α (cm^{-1})is the absorption coefficient of material;

x (cm) is the depth below the material surface (cm).

The etched depth by laser beam can be calculated by

$$d = \frac{1}{\alpha} \ln(\frac{F}{F_{th}}) \tag{3.2}$$

Since the threshold value F_{th} and the absorption coefficient α are dependent on the material, machining behavior for each individual material is different. Simply speaking, for laser beam with normally distributed energy profile which is natural for most of lasers, the materials with smaller values of F_{th} result in bigger opening of cavities ablated by laser pulses and materials with smaller absorption coefficient will be etched deeper under the same condition. Therefore, to understand the process of laser micromachining quantitatively, we have to examine each material we are using under a specific setup of laser equipment. For manufacturing purpose, the etched depth by laser beam and the dimension of the cavity etched on material are the parameters which we care about.

3) **Related work in laser micromachining**

There is quite some research on laser micromachining. Studies on different materials have been reported including polymers [Baudach 2000, Cheng 2004 & Klank 2002], silicon [Ren 2005 & Barsch 2003] and ceramics [Dear 2008]. In [Cheng 2004], the laser micromachining on PMMA by CO_2 has been study and thermal annealing is applied to improve the surface smoothness. Another study of CO_2 laser on PMMA is introduce in [Klank 2002] for rapid production of microfluidic systems. In [Roberts 1997] UV excimer

laser micromachining on polystyrene, polycarbonate, cellulose acetate, and poly (ethylene terephthalate) by mask pattern is studied. In those work, the quantity relationship between laser ablation parameters and laser parameters for specific materials is rarely setup especially for manufacturing purpose. Also PMMA, PDMS and polyethylene by excimer laser for biomedical application has not been seen too much. In this chapter, we will develop a flexible laser micromachining prototyping scheme for biocompatible polymers. Machining parameters for these materials will be studied for three different materials. Relationship between machining parameters and laser parameters will be setup given our lab-built laser micromachining system. Biomedical and chemical studies will be applied on the machined surfaces. This work will provide the foundation for our future work on medical device development and prototyping by laser micromachining.

3.2 Materials Used for the Study of Machining Performance by Laser Micromachining

Three polymers will be studied in this work regarding to laser micromachining performance. They are poly (methyl methacrylate) (PMMA), polydimethylsiloxane (PDMS) and polyethylene.

1) PMMA and its biomedical applications

PMMA, sometimes called acrylic glass or acrylic, is the synthetic polymer of methyl methacrylate. Its density varies from 1150 to 1190 kg/m3. PMMA can be made by almost all of common molding process including injection molding, compression molding, extrusion and cell casting. Upon laser cutting, PMMA vaporizes to gas compounds showing good laser machining performance. PMMA has relatively high impact strength and good biocompatible properties with human tissues. It's inert in neutral aqueous solution and no hydrolysis occurs during application [Cheng 2004]. Due to the mechanical and biocompatible characteristics, PMMA has numerous biomedical applications. It can be used for replacing intraocular lenses in eyes in the treatment of cataracts. PMMA-based porous composite structure has been developed as the drug delivery tool in bone implant site [Arcos 2001]. In this drug delivery

system, the materials release antibiotic locally while show bioactive properties to avoid osteomielitis incidence. In orthopaedics, PMMA bone cement is used to affix implants and remodel lost bone. Bone cements require high fracture toughness, high creep resistance as well as good bioactive property to allow the adherence of bone cement to bone. PMMA bone cement provides good mechanical properties and bioactivation of PMMA bone cement by using bioactive filter will help the adherence of bone cement to bone and improve the strength of bone-cement interface [Mousa 2000]. PMMA is also used to make dental implant with much lower cost compared with high cost and time consuming metals and ceramics.

2) PDMS and its biomedical applications

PDMS ($(H_3C)_3SiO[Si(CH_3)_2O]_nSi(CH_3)_3$) is a widely used silicone-based synthetic organic polymer with repeating units of silicon and oxygen. It is transparent, inert, non-toxic and non-flammable. Its biomedical applications range from contract lenses, medical device to implants. PDMS is one of the most commonly used materials for microfluid chips, which can be used in areas of optical telecommunication or biomedical research [Fujj 2002]. Cross-linked networks of PDMS were used as the material for cochlear implants [Abbasi 2006]. Another implant application can be seen in [Klenkler 2005]. PDMS whose surfaces were modified with epidermal growth factor (EGF) to improve the growth of corneal epithelial cells is used as the material for artificial cornea application. PDMS-based material was used as the agent for drug delivery. It showed excellent long-term biostability in the unloaded state [Simmons 2008].

3) High density polyethylene (HDPE) and its biomedical applications

Polyethylene is a thermoplastic consisting of long chains of the monomer ethylene. Polyethylene has different forms based on its density and branching including UHMWPE, WLMWPE, HMWPE, HDPE, MDPE and so on. Polyethylene is one of the popular materials used in hip and knee joint replacement due to its biocompatible properties. To enhance its mechanical properties such as stiffness and strength, usually some reinforcement procedures are needed to apply [Ramakrishna 2001]. Using HA particles for reinforcement is one of those approaches. Polyethylene is also used from bulky space fillers in head and neck and mostly used material in tendons and ligaments repairing. In [Liu 2004], Medpor porous high

density polyethylene is applied in ocular, orbital, nasal, malar, chin, cranial ear and mandibular implants (Porex Surgical, Inc.). Compared with conventional materials used in surgery like PMMA and titanium mesh, the porous character of polyethylene allows rapid fibrovascular, soft tissue and bone ingrowth, which strengthens the implants and decreases the risk of defection.

All of three materials are provided by Goodfellow Inc., USA.

3.3 Methods to Study the Effects of Laser Parameters on Machining Performance

3.3.1 Lab-built excimer laser micromachining system

The dimension of laser-ablated structures depends on both properties of materials used as mentioned above and the optical and mechanical setup of laser systems. A commercial laser scriber (COMPexPro 201, Coherent, Inc.) is employed in our experiments. This ArF laser emits laser pulses with wavelength at 193 nm and maximum average power of 4 W. The energy of output laser beam can be adjusted up to 400 mJ and the maximum repetition rate is 10/sec. A lab-built laser delivery system including a set of lens, three high UV reflection mirrors, and objective lens carries the laser beam from the laser scriber to material surface. A CCD camera is installed above the objective lens to monitor the machining process. A 3-aixs translation stage (A3200, Aerotech Inc.) is used to provide 3-axis synchronized translation motion for machining parts. The whole lab-built system is demonstrated in Fig. 3.1.

In Fig. 3.1, high UV reflection mirrors are used to change the direction laser beam. To reduce the beam size without losing energy, a set of lenses consisting of a positive and a negative lens separated by the sum of their focal lengths (FL_2+FL_1) can be put between laser source and machining platform. The output beam diameter reduces proportionally to FL_2/FL_1 and the beam fluence changes with a factor of $(FL_2/FL_1)^2$ correspondingly. An aperture is used to further reduce the laser beam size. However, it also reduces the laser radiance by

block part of laser beam. Objective lens focuses laser beam onto material surface to achieve possible highest fluence. The demagnification of objective lens and the size of incoming laser beam determine the laser spot size onto material surface.

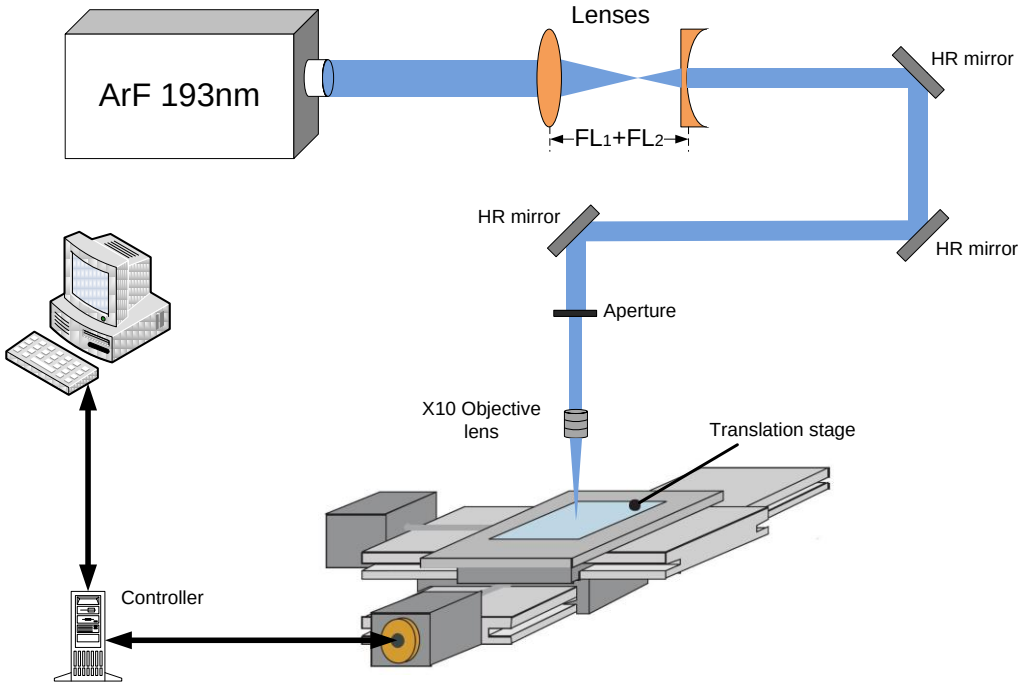

Fig.3.1 Lab-built laser micromachining system

3.3.2 G-code in laser micromachining systems

G-code is a numerical control programming language. By using G-codes, we can position objects to a desired location and control the objects moving in a predefined pattern. Although there is slight difference among different versions which sometimes causes compatible problems, G-code has become a standard in industry and is widely used and accepted in most CAD/CAM software. The A3200 series accept G-code as the input to control the motion of translation stage. Like some other software, A3200 series have some special functions which need non-standard commands. A program was developed to generate G-code based on the input 3D or 2D patterns accommodating the special commands required by A3200 controller.

3.3.3 Experiment design for study on the machining performance by laser micromachining

Our objective is to develop laser micromachining parameters for Poly (methyl methacrylate) (PMMA), Polydimethylsiloxane (PDMS) and high density polyethylene. Via building the relationship between machining parameters (e.g. cutting depth and width) and laser parameters (laser fluence, number of pulses per area and so on), we can find optimal laser setup parameter for different applications to achieve desired machining performance.

We designed three experiments to study the effects of laser parameters on machining performance. In these experiments, microchannels will be machined on material surfaces. Three channels will be made with each set of laser parameters. Cutting depth and width of these micro channels are observed and measured through profilometer and Scanning Electron Microscope (AIF, NC State University). The average value and standard deviation are calculated.

1) Experiment to study the effects of machining surfaces on cutting performance

The first experiment is to study the machining performance if we put machining surface beyond or below the focal plane of objective lens. Micro channels will be machined on the surfaces below or above the focal plane. The nominal laser energy is set to E=100mJ, the opening of aperture is set to A=2 and the number of laser pulses per area is 20.

2) Experiment to study the effects of laser energy on cutting performance

The second one is to investigate the effects of laser beam fluence on machining parameters (cutting depth and width) of three materials. The varying laser fluence will be achieved by two approaches: changing nominal energy of laser beam and adjusting the aperture opening. Nominal energy value can be changed through inputting different value from 0 to 400 mJ via control panel of the laser scriber. To avoid the unstable laser radiance near to the limit value, we set laser energy to 8 levels: *100, 125, 150, 175, 200, 225, 250* and *275* mJ. By adjust the opening of aperture, we can control the portion of laser beam going through and shooting onto material surface. The opening of aperture has been linearly discretized into 9 levels (*A=0, 1, 2, 3, 4, 5, 6, 7* and *8*). The number of laser pulses per area is

10 for polyethylene and 20 for PMMA and PDMS.

3) **Experiment to study the effects of number of pulses per area on cutting performance**

In the third experiment, we are trying to reveal the relationship between number of pulses per area and machining performance of these three materials. Nominal laser energy will be set to 100 mJ and aperture will be set to A=2. number of laser pulses per area will be varying from 5, 10, 15, 20, 30, 40, 50 to 60.

3.4 Preliminary Results and Discussions

3.4.1 Spot size measurement

Laser fluence $F(J/cm^2)$ is calculated using laser energy divided by spot size shooting laser on material surface $(F=E/A_{spot})$. Thus, we need to measure both spot size and laser energy we can achieve for machining.

In our laser system, laser beam has been reduced by set of lenses and aperture and then focused by objective lens onto material surface. Therefore, the spot size is dependent on dimension of laser beam coming into objectives, which is determined by focal length of both lenses (FL_1 and FL_2) and the opening size of aperture, and demagnification factor of objective lens. Both focal length and demagnification factor have been specified after we choose optical devices. So in our experiments, we change the spot size by varying the opening of aperture. Aperture opening has been discretized into 9 levels. On each level we shot single pulse onto thermal paper which is put on focal plane of objective lens. Through measuring the spot on thermal paper created by one laser pulse, we can calculate the area. Results have been listed in the table and figure below.

Aperture size	Spot size (cm^2)
A=0	3.17×10^{-4}
A=1	3.69×10^{-4}
A=2	4.61×10^{-4}
A=3	5.43×10^{-4}
A=4	6.06×10^{-4}
A=5	7.29×10^{-4}
A=6	7.80×10^{-4}
A=7	8.32×10^{-4}
A=8	8.50×10^{-4}

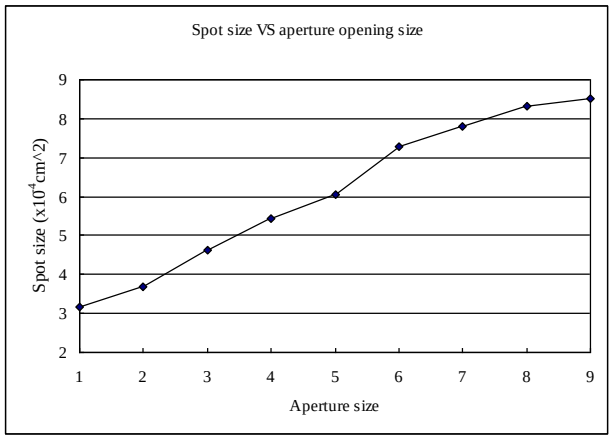

Fig.3.2 Spot sizes under different opening of aperture

3.4.2 Energy measurement

Energy losses are unavoidable during the transferring process from laser scriber to material surface. Reflection and diffusion by optical devices and absorption by air are the main sources causing energy losses.

Due to the uncertain energy losses from the laser scriber to material surface, we need to know the laser energy value right above the material surfaces. This energy is what we can achieve for machining purposes. We measure the energy above the material surface by a laser energy meter. The average value and standard deviation are calculated and listed in Table 3.1. Relationship between the nominal energy and actual energy is shown in Fig.3.3 and Fig.3.4. Actual energy values under same aperture size and different nominal energy is shown in Fig.3.3. While actual energy values under different aperture sizes and same nominal energy are presented in Fig.3.4.

Table 3.1 Actual laser energy under different nominal energy and aperture opening

Nominal Energy (mJ)		100	125	150	175	200	225	250	275
A=0	AVG	0.110	0.130	0.152	0.168	0.182	0.199	0.216	0.228
	STD	0.001	0.001	0.001	0.001	0.004	0.003	0.001	0.004
A=1	AVG	0.329	0.388	0.451	0.501	0.548	0.601	0.643	0.683
	STD	0.001	0.003	0.003	0.001	0.001	0.003	0.001	0.001
A=2	AVG	1.106	1.305	1.534	1.708	1.876	2.062	2.210	2.356
	STD	0.003	0.006	0.008	0.002	0.006	0.003	0.005	0.001
A=3	AVG	1.907	2.257	2.667	2.960	3.283	3.610	3.870	4.137
	STD	0.006	0.006	0.006	0.010	0.012	0.010	0.010	0.029
A=4	AVG	2.970	3.553	4.240	4.757	5.297	5.827	6.247	6.680
	STD	0.010	0.012	0.010	0.012	0.015	0.006	0.031	0.035
A=5	AVG	4.170	4.987	5.943	6.697	7.480	8.297	8.960	9.573
	STD	0.044	0.023	0.050	0.006	0.020	0.006	0.026	0.015
A=6	AVG	5.430	6.523	7.893	8.907	9.947	11.110	11.947	12.833
	STD	0.035	0.040	0.021	0.021	0.023	0.036	0.025	0.580
A=7	AVG	6.953	8.333	10.097	11.460	12.770	14.310	15.550	16.707
	STD	0.090	0.047	0.076	0.044	0.035	0.046	0.010	0.035
A=8	AVG	7.560	9.270	11.287	12.903	14.507	16.277	17.590	18.897
	STD	0.026	0.036	0.085	0.055	0.032	0.021	0.070	0.15

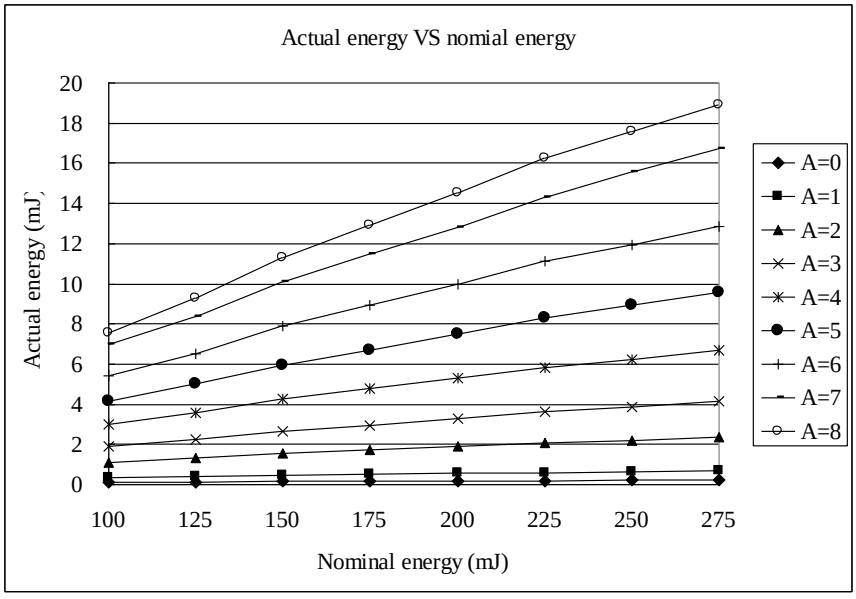

Fig.3.3 Actual energy VS nominal energy

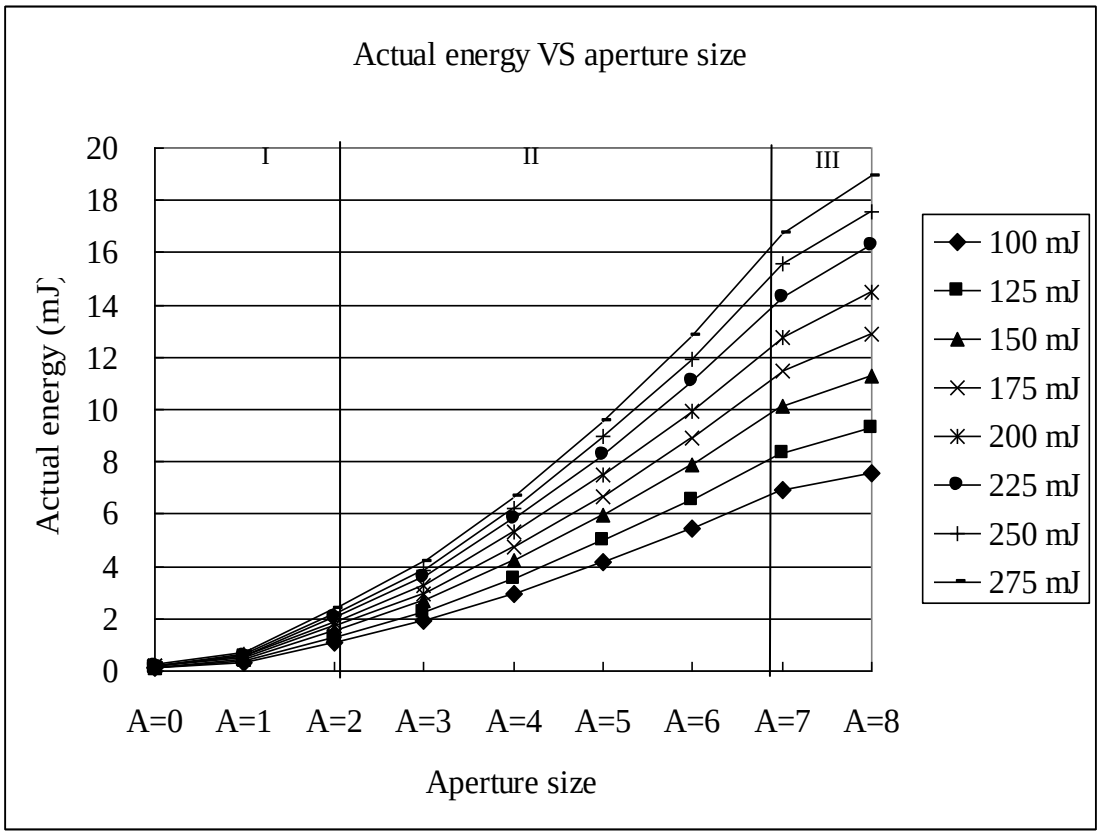

Fig.3.4 Actual energy VS aperture opening

From the experiment to measure the actual laser energy value above the material surfaces, we can clearly see actual energy is linearly dependent on the nominal energy since the energy loses caused by laser delivery system is linear. While the actual energy doesn't increase linearly when the opening of aperture increases. At the beginning when opening of aperture becomes larger, the actual energy increases lowly as shown in region I of Fig.3.4. Then actual energy increases much faster in region II. In region III of Fig.3.4, the increasing of actual energy slows down. This nonlinear pattern is due to the energy profile of excimer laser. Excimer laser presents a multimode energy profile in different direction. In the direction along *x*-axis in Fig.3.5 (a), the laser energy is normally distributed. In the direction of *y*-axis, the energy distribution is like top-flat in the middle and normal distribution in both ends. In region I and III in Fig.3.5 (b) the laser fluence increase slowly as opening of aperture becomes larger which is corresponding to the region I and III in Fig.3.4. While in region II in

Fig.3.5 (b) the rate of fluence change is faster than region I and III.

3.4.3 Calculation of laser fluence

Based on the actual energy and spot size we have measured, the maximum laser fluence (J/cm^2) used for ablating materials can be calculated. Results under different spot sizes and nominal energy value are listed as follows. The relationship between aperture size, nominal energy and maximum fluence are shown in Fig.3.6 and Fig.3.7 respectively.

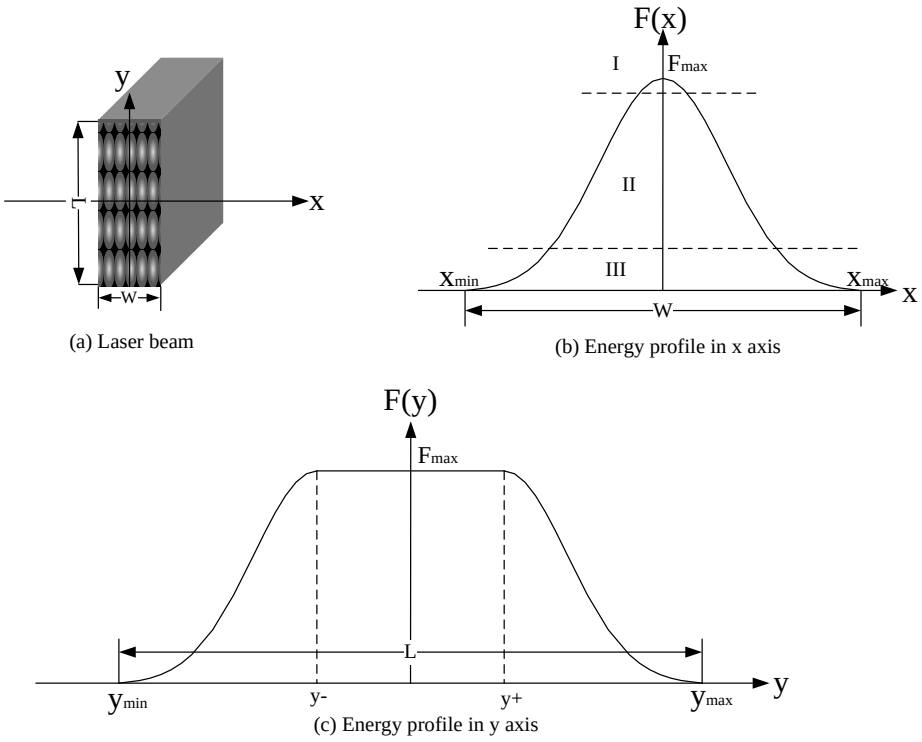

Fig.3.5 Laser energy profile of excimer laser

Table 3.2 Laser fluence (J/cm^2) under different nominal energy and aperture opening

Nominal energy (mJ)	100	125	150	175	200	225	250	275
A=0	0.35	0.41	0.48	0.53	0.57	0.63	0.68	0.72
A=1	0.89	1.05	1.22	1.36	1.49	1.63	1.74	1.85
A=2	2.40	2.83	3.33	3.71	4.07	4.47	4.80	5.11
A=3	3.51	4.15	4.91	5.45	6.04	6.65	7.13	7.62
A=4	4.90	5.87	7.00	7.85	8.74	9.62	10.31	11.03
A=5	5.72	6.84	8.15	9.18	10.26	11.38	12.29	13.13
A=6	6.96	8.36	10.12	11.42	12.75	14.25	15.32	16.46
A=7	8.36	10.02	12.14	13.78	15.35	17.21	18.70	20.09
A=8	8.89	10.90	13.27	15.17	17.06	19.14	20.68	22.22

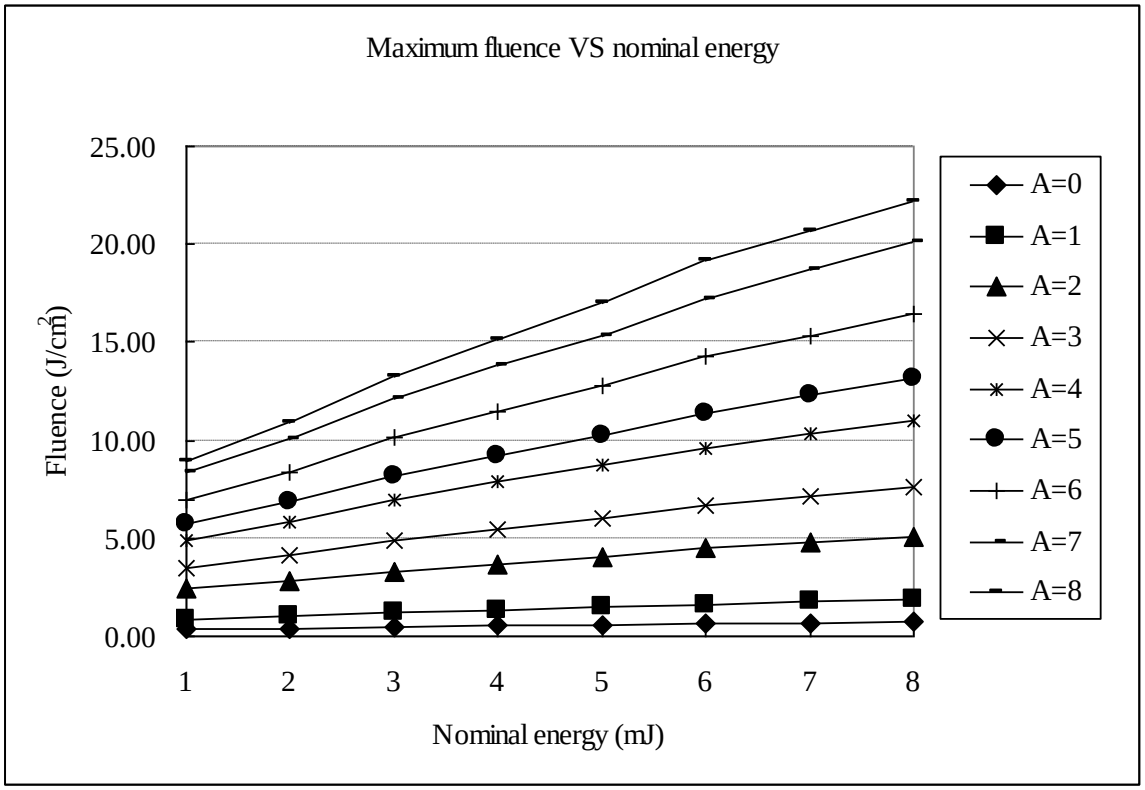

Fig.3.6 Fluence VS nominal energy

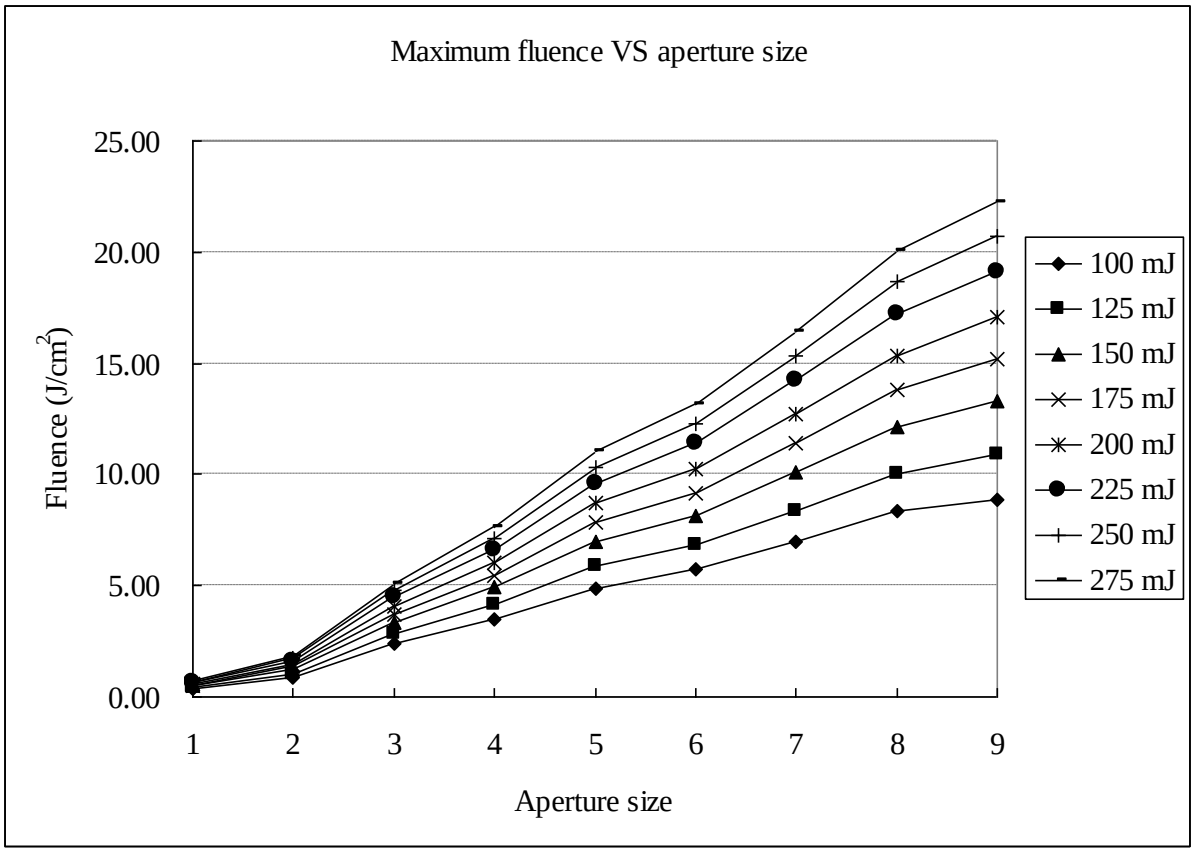

Fig.3.7 Fluence VS aperture opening

3.4.4 Effects of different machining planes on cutting depth and width

In our laser delivery system shown in Fig.3.1, the objective lens focuses the incoming laser beam to a small spot. On the focal plane, the maximal laser fluence and smallest spot size can be achieved. On the other machining surfaces below and above focal plane, we can observe different machining performance. The cutting depth and width of polyethylene, PMMA and PDMS on the different machining plane are listed in Table 3.3, 3.4 and 3.5 respectively along with the distance to the focal plane. As expected, the largest cutting depth and smallest width can be achieved on focal plane. While below and above the focal plane, the cutting depth becomes smaller and the opening of the channels becomes wider as the distance to focal plane increases. The changing trend of the cutting depth and width on

different machining planes is presented in Fig.3.8, Fig.3.9 and Fig.3.10 for polyethylene, PMMA and PDMS respectively.

Table 3.3 Cutting depth and width on different machining planes (polyethylene)

Distance to focal plane		400	300	200	100	0	-100
Depth	AVG	54.90	58.77	66.50	69.89	62.27	54.90
	STD	0.21	0.63	0.55	1.38	0.21	0.42
Width	AVG	106.04	93.11	87.67	82.10	77.27	81.98
	STD	0.46	0.83	0.56	0.91	0.36	0.96
Distance to focal plane		-200	-300	-400	-500	-600	
Depth	AVG	49.70	46.92	44.01	42.44	30.39	
	STD	0.00	0.55	0.21	0.36	17.11	
Width	AVG	85.13	93.59	102.17	115.23	127.21	
	STD	0.91	0.73	0.21	1.17	0.84	

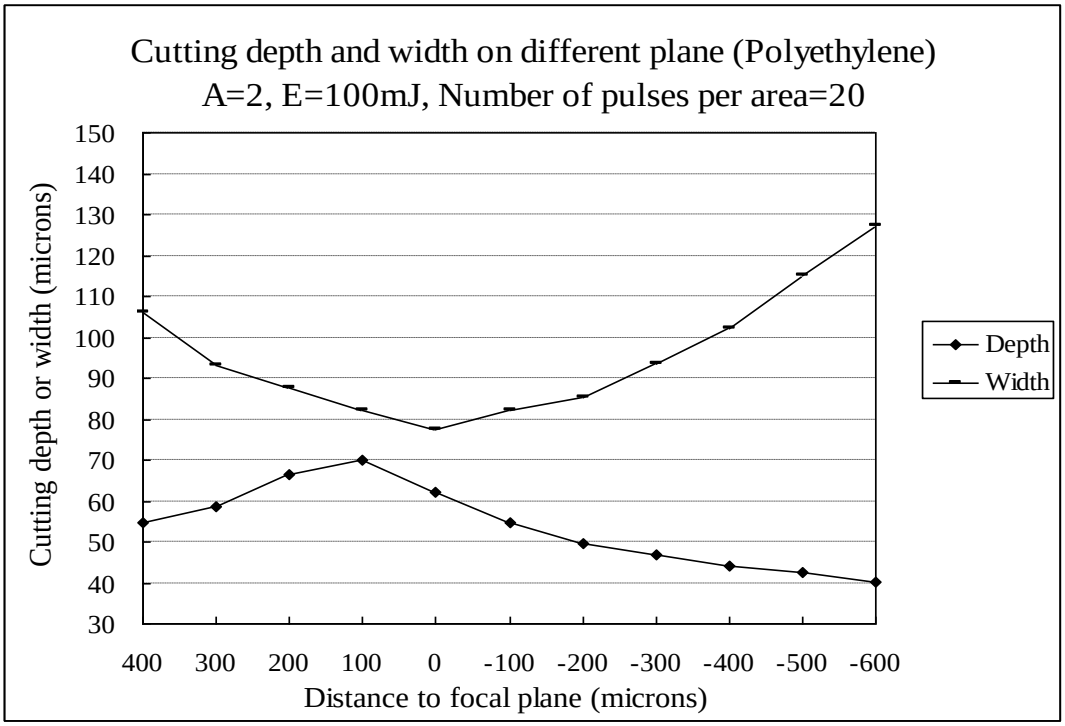

Fig.3.8 Cutting depth and width on different machining planes (polyethylene)

Table 3.4 Cutting depth and width on different machining planes (PMMA)

Distance to focal plane		300	200	100	0
Depth	AVG	50.122	78.748	109.733	110.277
	STD	3.655	5.189	3.158	1.008
Width	AVG	64.942	53.745	45.533	43.727
	STD	1.667	2.290	3.625	0.711
Distance to focal plane		-100	-200	-300	-400
Depth	AVG	90.076	72.547	54.634	52.781
	STD	4.519	4.436	2.028	2.085
Width	AVG	47.516	58.852	69.584	74.524
	STD	2.808	2.134	4.809	1.972

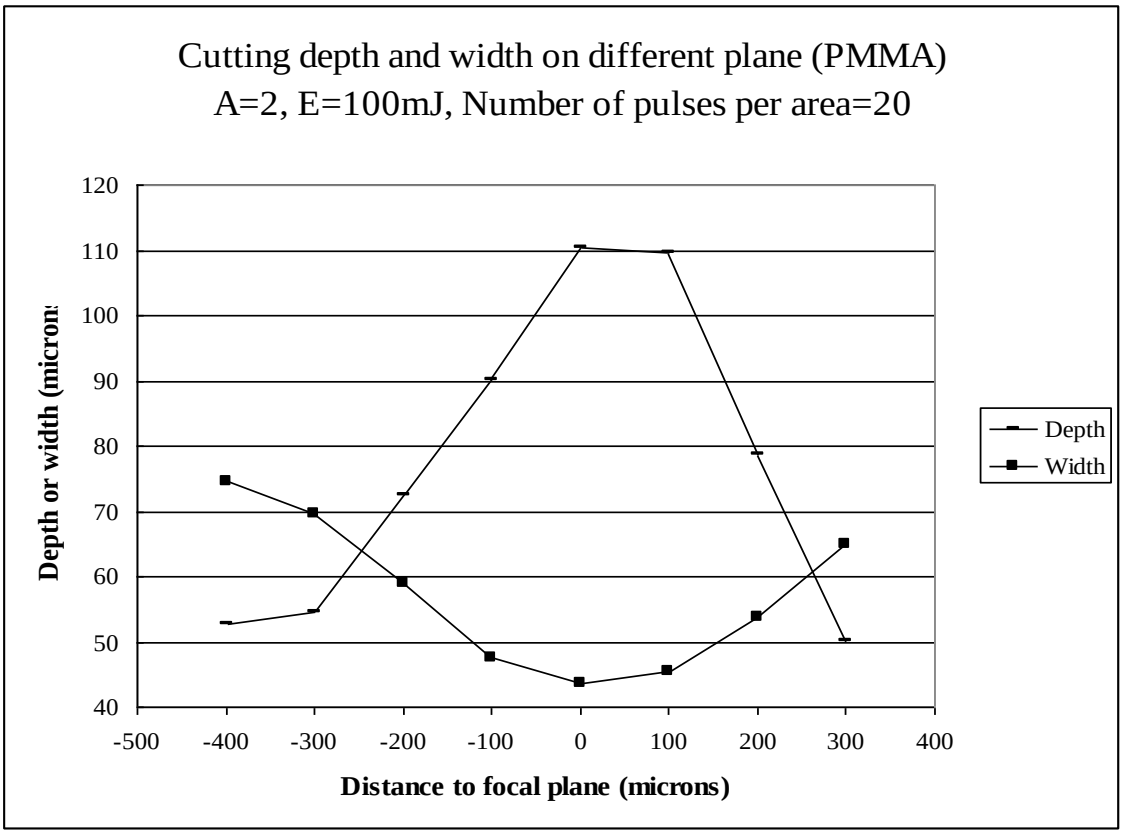

Fig.3.9 Cutting depth and width on different machining plane (PMMA)

Table 3.5 Cutting depth and width on different machining planes (PDMS)

Distance to focal plane		500	400	300	200	100	0	-100
Depth	AVG	22.73	27.57	46.43	73.63	78.72	77.39	71.22
	STD	0.21	0.63	3.08	0.52	4.41	0.76	1.86
Width	AVG	82.59	72.43	58.40	43.71	39.90	40.51	46.79
	STD	0.91	0.55	2.05	1.80	1.31	1.11	2.02
Distance to focal plane		-200	-300	-400	-500	-600	-700	
Depth	AVG	39.18	30.35	24.32	20.56	19.59	18.50	
	STD	1.45	2.06	0.37	0.76	0.63	0.51	
Width	AVG	53.93	67.11	78.48	89.48	106.47	116.83	
	STD	1.51	1.88	1.72	1.68	0.26	2.06	

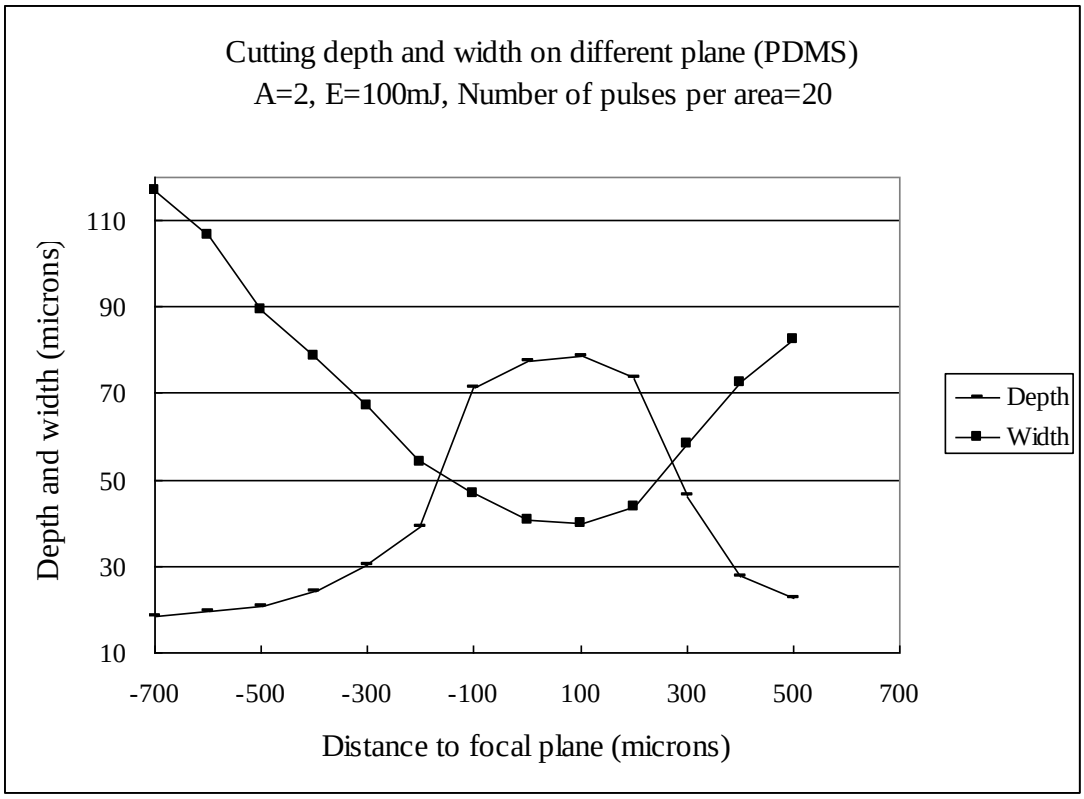

Fig.3.10 Cutting depth and width on different machining planes (PMMA)

Even though we can achieve the deepest cut on focal plane, it doesn't mean it is optimal

when we select the machining parameters. Along with the cutting depth and width, some other factors like surface quality should be considered. Some SEM images for polyethylene and PDMS are shown in Fig.3.11 and Fig.3.12. Those micro channels were machined on different planes in our experiments. The distances from those machining planes to focal plane vary from 500 to -700 microns approximately. On the machining planes close to focal plane, some cracks can be observed on the bottom of the channels. Those cracks may be caused by two reasons. For the machining planes above the focal plane, the focus of laser beam is below the machining plane. Thus, higher laser energy on the focus of laser beam will further cut a small cavity on the bottom of the channel, which can be seen in Fig.3.11(b)-(d). Another reason resulting in the cracks may come from the high heat concentration on focal plane or on the machining planes close to focal plane. As illustrated in Fig.3.11, around 100-200 microns below focal plane we can achieve very clean cut on polyethylene surfaces.

Similar to polyethylene, we can achieve good surface quality below the focal plane for PMMA and PDMS. We chose 200 microns below focal plane for PMMA and 300 microns below focal plane for PDMS respectively. Compared with polyethylene and PMMA, surface quality of PMDS is not as good as other two materials even though micro channels are machined on the planes far below the focal plane. The comparison of surface quality of polyethylene and PDMS can be seen in Fig.3.11 and Fig.3.12.

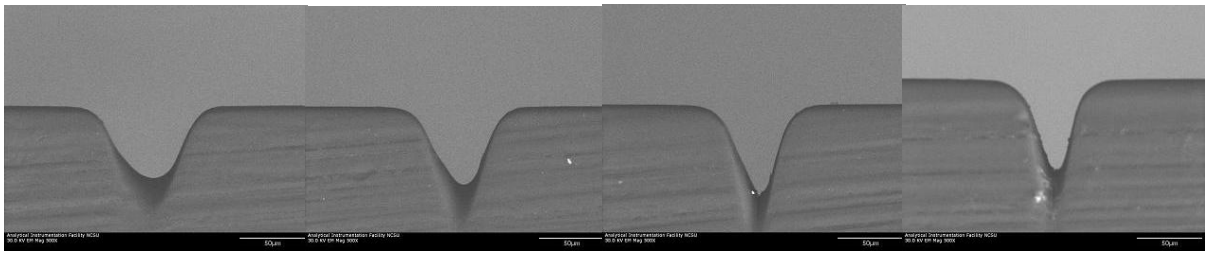

(a) 400 (b) 300 (c) 200 (d) 100

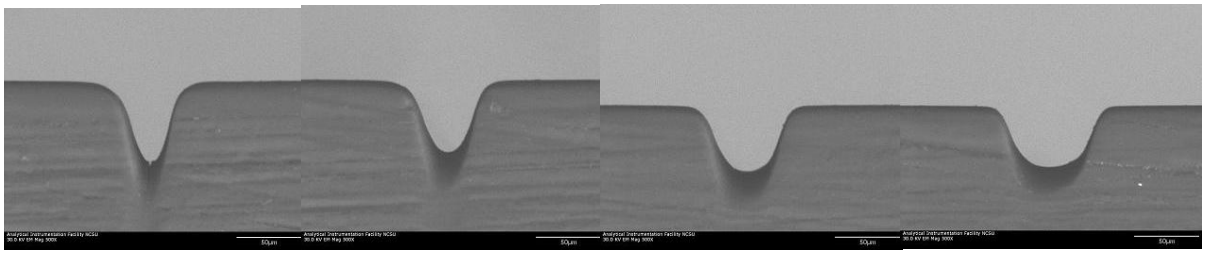

(e) 0 (f) -100 (g) -200 (h) -300

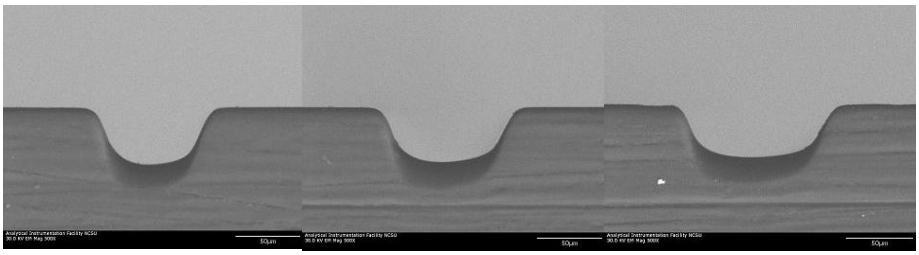

(i) -400 (j) -500 (k) -600

Fig.3.11 SEM micrograph for micro channels machined on different machining planes from 400 microns above focal plane to 600 microns below focal plane:
(a), (b), (c), (d), (e), (f), (g), (h), (i), (j), and (k) represent the microchannels on the machining planes with distance to focal plane of 400, 300, 200, 100, 50, -100, -200, -300, -400, -500, and -600 respectively (polyethylene)

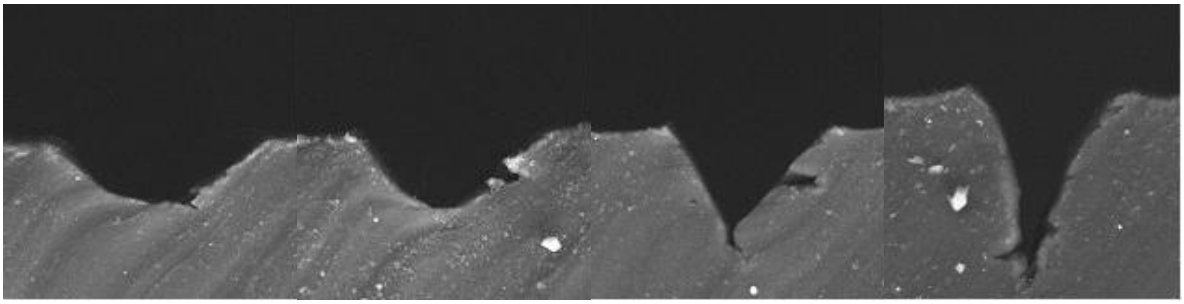

(a) 500 (b) 400 (c)300 (d)200

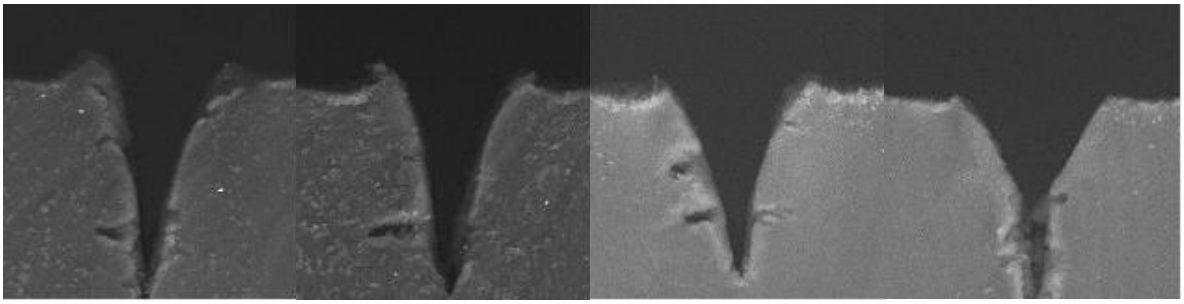

(e)100 (f)0 (g)-100 (h)-200

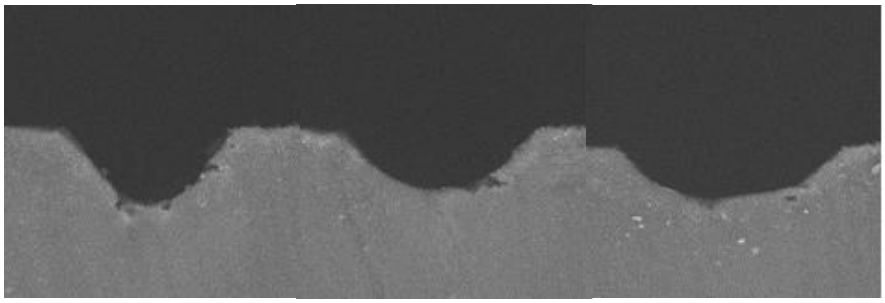

(i)-300 (j)-400 (k)-500

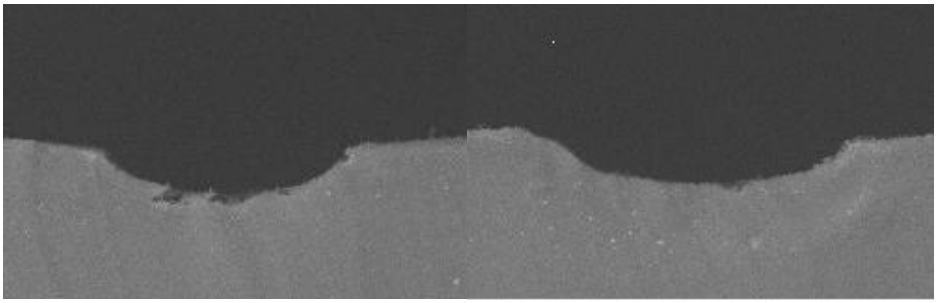

(l)-600 (m)-700

Fig.3.12 SEM micrograph for microchannels machined on different machining planes from 500 microns above focal plane to 700 microns below focal plane (PDMS): (a), (b), (c), (d), (e), (f), (g), (h), (i), (j), (k), (l) and (m) represent the microchannels on the machining planes with distance to focal plane of 500, 400, 300, 200, 100, 50, -100, -200, -300, -400, -500, -600 and -700 respectively

3.4.5 Effects of number of laser pulses per area on cutting depth and width

To study the effects of number of laser pulses per area on machining performance, we set the opening of aperture to *A=2* and varied numbers of laser pulses per area as from 5, 10, 15, 20, 30, 40, 50 to 60. The average value and standard deviation of cutting depth and width for polyethylene and PMMA are listed in Table 3.6.

Table 3.6 Cutting depth and width with different number of pluses per area (polyethylene, A=2, E=100mJ)

Number of pulses per area		5	10	15	20	30	40	50	60
Depth(цm)	AVG	17.47	29.93	41.71	54.90	76.54	99.03	117.89	141.83
	STD	1.21	0.48	0.31	1.51	0.36	0.62	2.74	0.96
Width(цm)	AVG	64.30	68.56	73.22	78.97	83.68	87.37	89.73	92.42
	STD	0.13	2.45	0.64	2.35	0.42	0.58	1.82	0.32

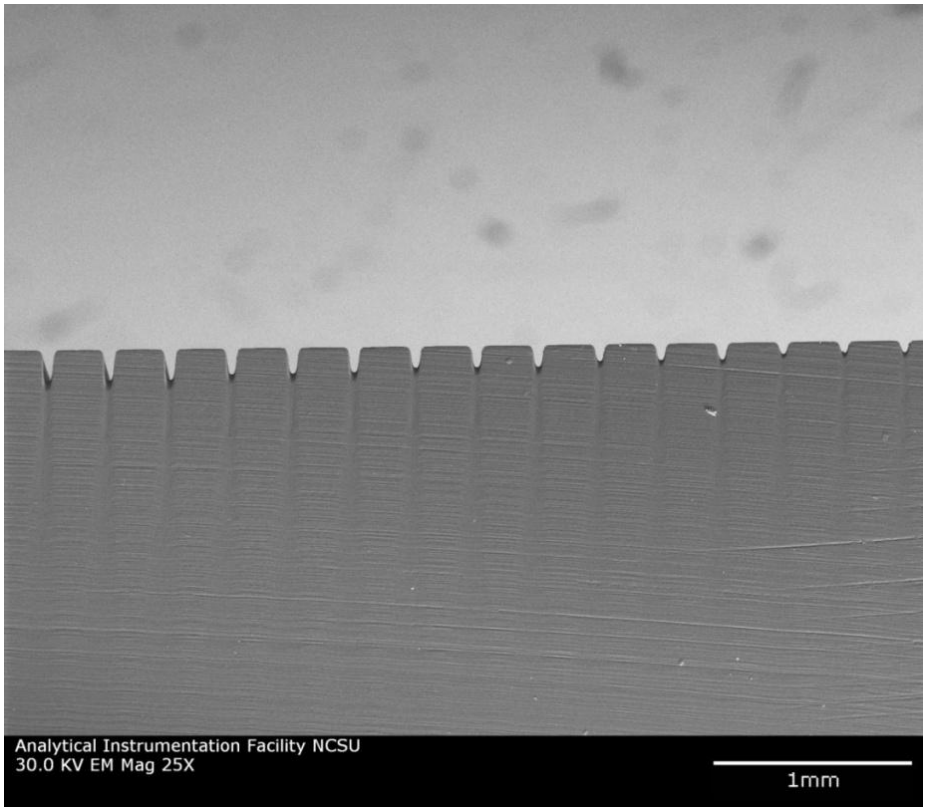

Fig.3.13 Overview of micro channels cut by different number of pulses per area: from left to right the number of pulses per area is 60, 50, 40, 30 and 20.

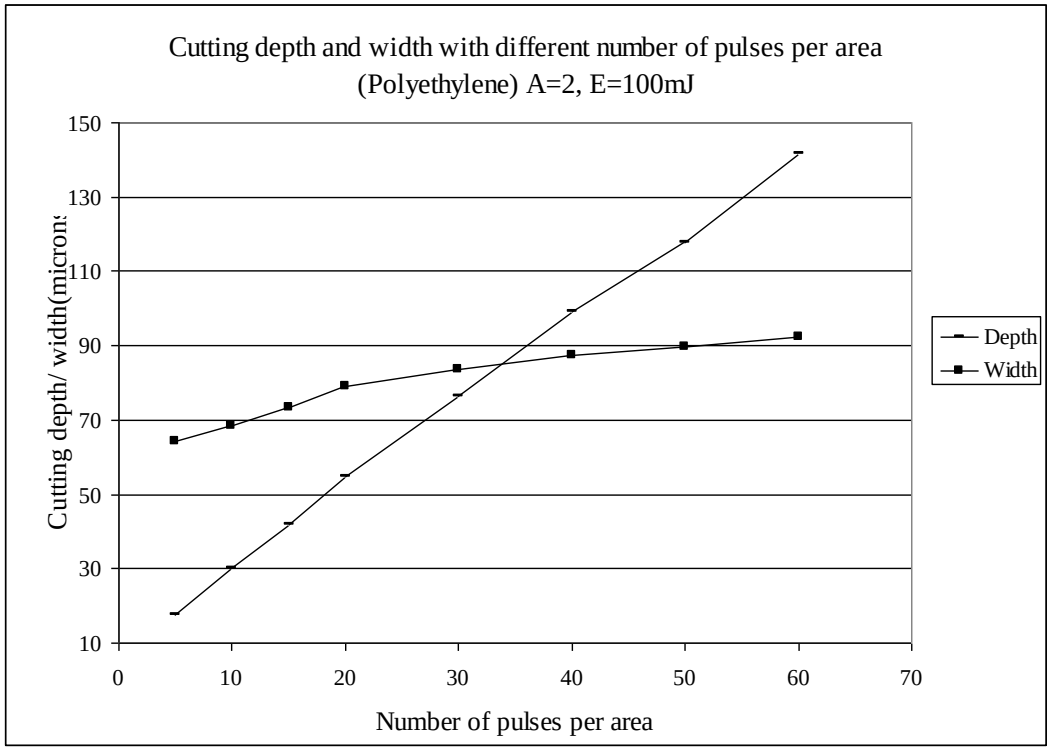

Fig.3.14 Cutting depth and width with different number of pulses per area (polyethylene)

Table 3.7 Cutting depth and width with different number of pluses per area (PMMA, A=2, E=100mJ)

Number of pulses per area		10	15	20	30	40	50	60
Depth(цm)	AVG	19.15	28.79	38.62	50.84	66.63	78.35	93.33
	STD	0.16	0.98	5.70	3.65	1.16	0.82	1.97
Width(цm)	AVG	74.99	76.03	78.50	82.07	85.09	87.17	87.64
	STD	1.62	1.15	0.62	0.16	0.49	1.81	2.13

Table 3.8 Cutting depth and width with different number of pluses per area (PDMS, A=2, E=100mJ)

Number of pulses per area		5	10	15	20	30	40	50	60
Depth(цm)	AVG	7.86	12.15	17.78	21.40	31.56	41.72	52.36	60.94
	STD	0.38	0.48	0.36	0.36	0.73	1.58	1.79	3.68
Width(цm)	AVG	79.98	84.97	86.69	88.27	89.96	92.50	92.38	92.77
	STD	2.82	0.86	0.36	0.55	0.96	0.73	0.55	1.59

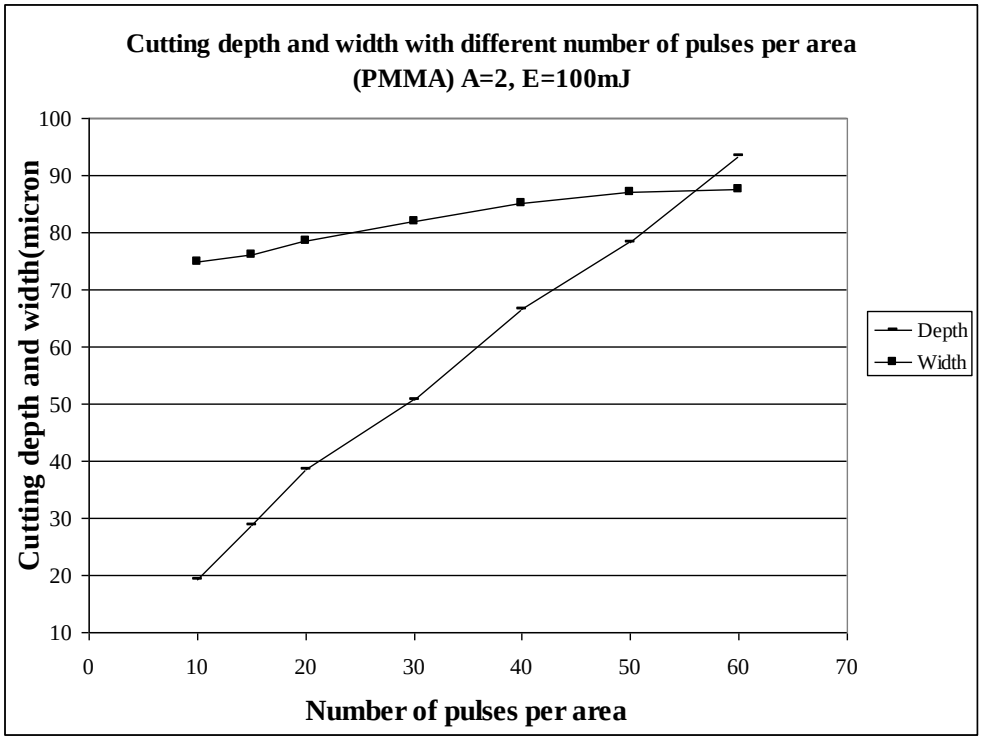

Fig.3.15 Cutting depth and width with different number of pulses per area (PMMA)

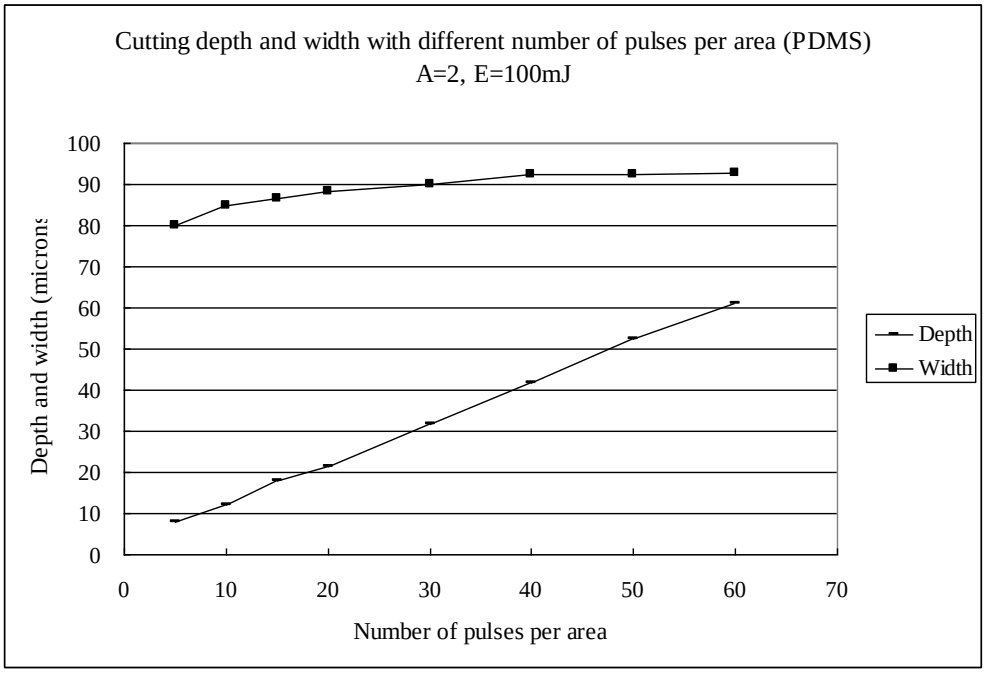

Fig.3.16 Cutting depth and width with different number of pulses per area (PDMS)

According to the statistical results, cutting depth is linearly dependent on the number of pulses per area as shown in Fig.3.14 for polyethylene, Fig.3.15 for PMMA and Fig.3.16 for PDMS. This means the effect of multiple laser pulses on cutting depth can be directly accumulated. The total cutting depth can be calculated as $d = A \bullet N$, where *N* is the number laser pulses per area and *A* is the cutting depth by one laser pulse. While the cutting width is not linearly changing as the number of pulses per area increases. The increasing rate of cutting width slows down as the number of pulses per area becomes larger and larger as shown in Fig.3.14, Fig.3.15 and Fig.3.16. Cutting width almost keeps constant when number of pulse per area is 50 and 60. The cross section of microchannels cut by different number of pulses per area can be seen in Fig.3.17, Fig.3.18 and Fig.3.19 for polyethylene, PMMA and PDMS respectively.

This observation can be explained by the energy profile of laser beam and the characteristic of laser ablation. The laser energy profile in one direction of laser beam as shown in Fig.3.5 (b) can be approximately defined as:

$$F(x) = F_{\max} e^{-\frac{x^2}{2\sigma^2}} \qquad (3.3)$$

where *F(x)* is the fluence on one point of the laser profile curve;

F_{max} is the maximal fluence in this laser beam which is the center of cross section plane;

x is the *x* value along one direction on the cross section of laser beam in Fig. 3.5(a);

σ is the range that laser beam spread over. In this case $\sigma = \frac{x_{\max} - x_{\min}}{6} = W/6$, where *W* is the dimension of the laser beam along *x*-axis. Outside *W*, laser energy is small enough to be neglected.

As we know, the laser ablation happens when the laser fluence reaches a threshold value (F_{th}) of the material. Assuming that when $x \in [-x_{th}, x_{th}]$ the laser fluence is equal to or more than F_{th}, we have

$$F_{th} = F_{\max} e^{-\frac{x_{th}^2}{2\sigma^2}}. \qquad (3.4)$$

x_{th} can be calculated as:

$$x_{th} = \sigma\sqrt{2\ln\frac{F_{\max}}{F_{th}}} \tag{3.5}$$

If the cutting width is *w*, $w = 2x_{th}$. Thus, $W = 2\sigma\sqrt{2\ln\frac{F_{\max}}{F_{th}}}$. As we discussed earlier, the cutting depth is linearly dependent on number of pulses per area. The cutting effects by multiple laser pulses can be treated as the accumulation of singles pulse and laser fluence by multiple pulses can be calculated as $F_{\max} = N \bullet F_s$ where F_m is the laser fluence by multiple laser pulses, F_s is the laser fluence by one single pulse and *N* is the number of laser pulses per area. Thus, as more the number of laser pulses per area which increases the F_{max} linearly, the increasing rate of *w* becomes smaller and smaller.

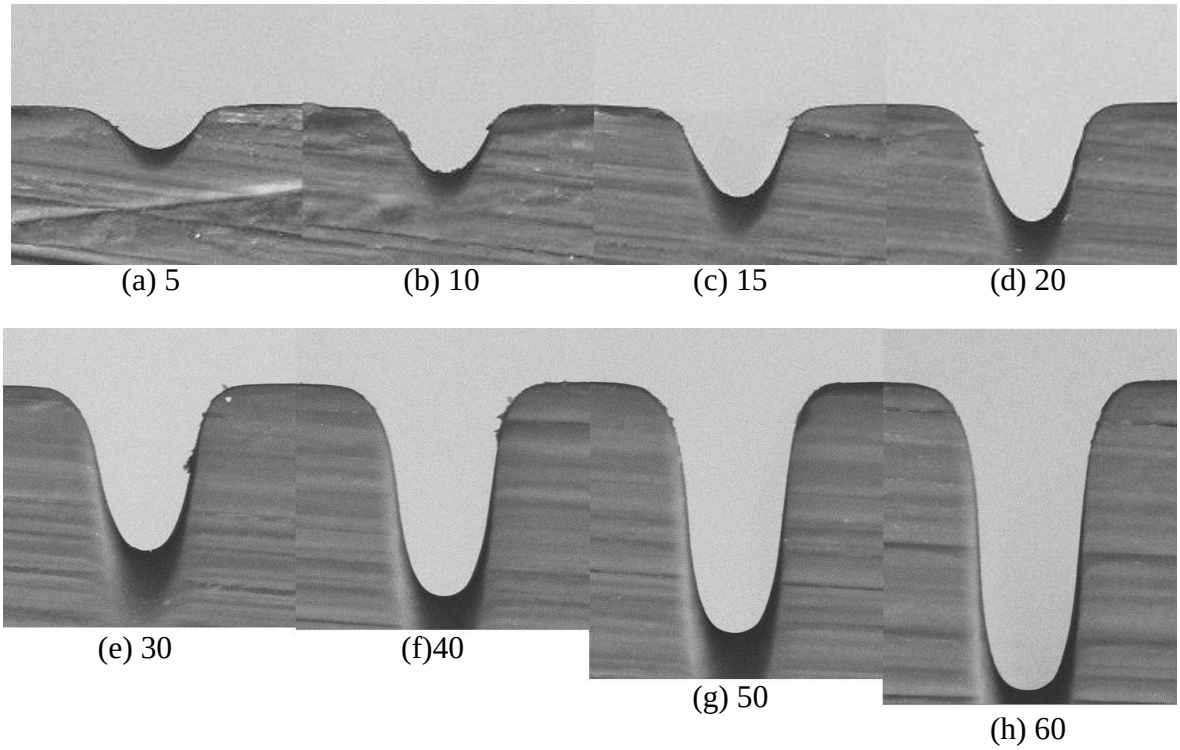

Fig.3.17 SEM images for microchannels cut by different number of pulses per area (polyethylene): (a) P=5; (b) P=10; (c) P=15; (d) P=20; (e) P=30; (f) P=40; (g) P=50; (h) P=60.

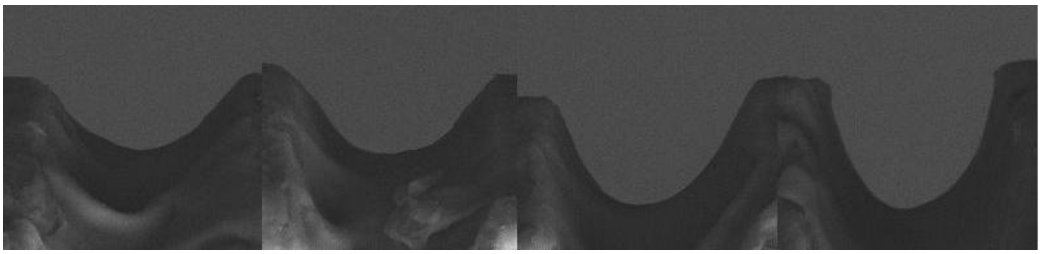

(a) 10 (b) 15 (c) 20 (d) 30

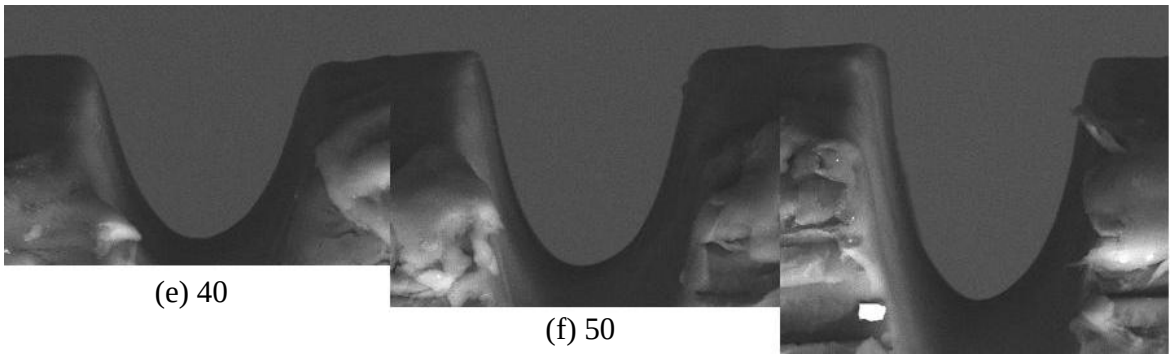

(e) 40 (f) 50 (g) 60

Fig.3.18 SEM images for microchannels cut by different number of pulses per area (PMMA): (a) P=10; (b) P=15; (c) P=20; (d) P=30; (e) P=40; (f) P=50; (g) P=60.

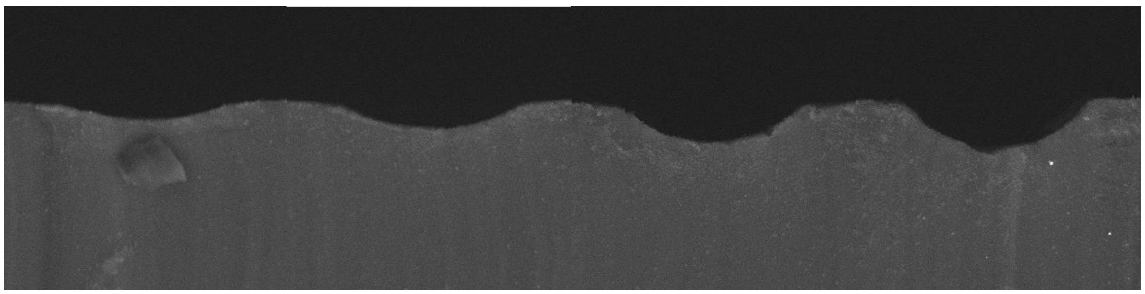

(a) 5 (b) 10 (c)15 (d) 20

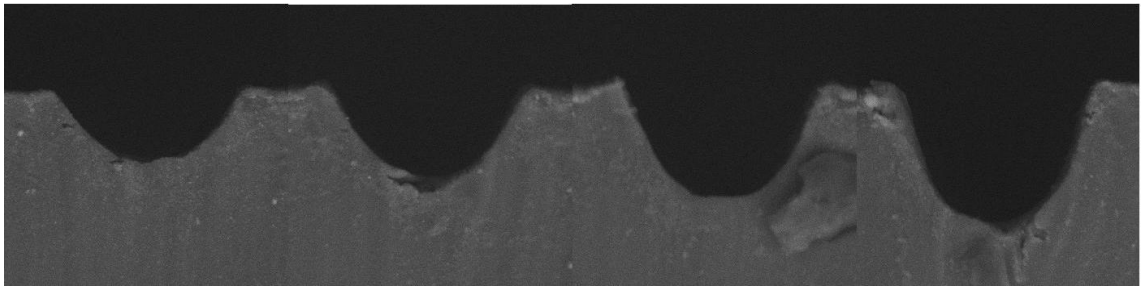

(e)30 (f) 40 (g) 50 (h) 60

Fig.3.19 SEM images for microchannels cut by different number of pulses per area (PDMS): (a) P=10; (b) P=15; (c) P=20; (d) P=30; (e) P=40; (f) P=50; (g) P=60.

3.4.6 Effects of laser energy on cutting depth and width

Actual laser energy shooting on material surface can be adjusted via changing nominal energy values and aperture openings. To study the effects of laser energy on machining performance, micro channels are machined under different combination of nominal energy values and aperture openings.

For polyethylene, the nominal laser energy ranges from 100, 125, 150, 175, 200, 225, 250 to 275 mJ; while the aperture opening varies from A=0, 1, 2, 3, 4, 5, 6, 7, to 8. The cutting depth and width by each combination of laser energy and aperture opening are measured via SEM images and the results are listed in Table 3.9 and Table 3.10 respectively. The relationship between cutting depth/width and nominal laser energy/aperture opening can be seen graphically from Fig. 3.20 to Fig. 3.23.

From the numerical and graphical results, we can see that at the beginning when energy is low, the cutting depth is linearly dependent on the nominal energy values. When energy value is over 150 and 175 mJ, the increasing rate of cutting depth will slow down as the energy value linearly increases. When the aperture opening is large, the cutting width changes accordingly while cutting depth doesn’t change too much.

Proper laser parameters can be selected or plotted on those diagrams to achieve desired machining parameters. Fig.3.24 and Fig. 325 show some SEM images of micro channels on polyethylene surface generated by different laser parameter. In Fig.3.24, the aperture opening was set to 0 and the nominal energy values varied from 100 mJ to 275 mJ; while in Fig.3.25 laser energy was fixed to 100 mJ and aperture openings ranged from 0 to 7.

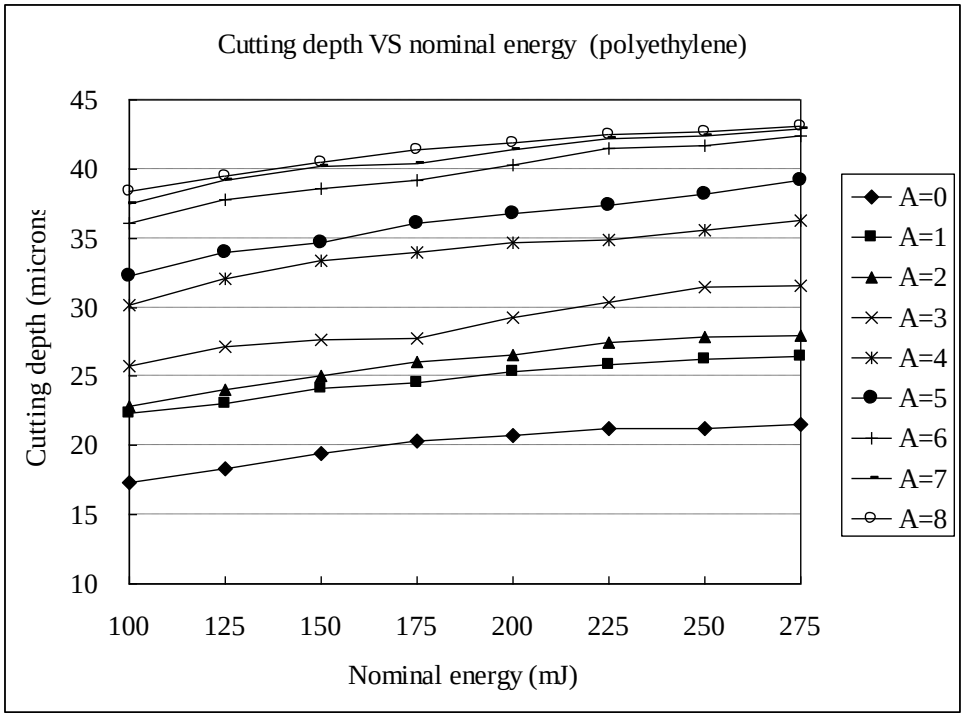

Fig.3.20 Cutting depth VS nominal energy (polyethylene)

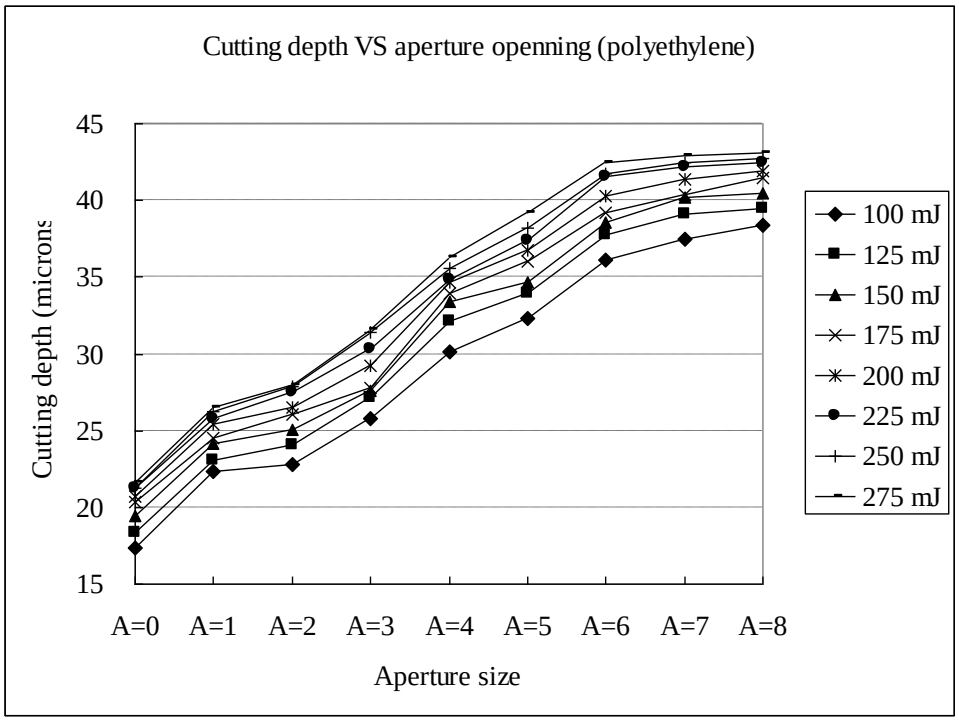

Fig.3.21 Cutting depth VS aperture opening (polyethylene)

Table 3.9 Cutting depth by different nominal energy and aperture opening (polyethylene)

Energy (mJ)		100	125	150	175	200	225	250	275
A=0	AVG	17.35	18.32	19.41	20.37	20.75	21.22	21.28	21.58
	STD	0.55	0.00	0.18	0.64	0.31	0.26	0.10	0.25
A=1	AVG	22.37	23.03	24.18	24.55	25.39	25.82	26.24	26.48
	STD	0.42	0.31	0.28	0.10	0.48	0.28	0.38	0.36
A=2	AVG	22.79	24.03	25.09	26.06	26.54	27.47	27.87	27.93
	STD	0.28	0.13	0.45	0.45	0.28	0.45	0.46	0.96
A=3	AVG	25.76	27.12	27.60	27.79	29.23	30.35	31.44	31.55
	STD	0.96	0.13	1.14	0.80	0.19	1.37	1.47	0.34
A=4	AVG	30.17	32.10	33.37	33.98	34.70	34.82	35.55	36.28
	STD	0.28	0.26	0.36	0.21	0.42	0.36	0.36	0.73
A=5	AVG	32.29	33.92	34.70	36.04	36.76	37.36	38.21	39.18
	STD	0.36	0.26	0.21	0.84	0.55	0.36	0.21	0.51
A=6	AVG	36.07	37.79	38.59	39.20	40.31	41.51	41.72	42.42
	STD	0.63	0.43	0.46	0.70	0.17	0.35	0.30	0.46
A=7	AVG	37.48	39.15	40.20	40.41	41.41	42.22	42.42	42.94
	STD	0.30	0.64	0.30	0.18	0.30	0.35	0.17	0.01
A=8	AVG	38.35	39.50	40.47	41.42	41.94	42.46	42.72	43.10
	STD	0.26	0.21	0.40	0.45	0.26	0.26	0.26	0.18

Table 3.10 Cutting width by different nominal energy and aperture opening (polyethylene)

Energy (mJ)		100	125	150	175	200	225	250	275
A=0	AVG	53.75	58.95	61.79	64.75	68.08	70.56	72.67	73.91
	STD	0.21	0.18	0.55	0.63	0.75	1.79	1.11	0.38
A=1	AVG	73.39	76.48	79.38	82.71	85.61	87.42	90.14	92.21
	STD	0.53	0.46	0.73	1.42	0.48	0.31	1.45	1.43
A=2	AVG	105.02	110.37	114.69	118.93	120.39	123.21	127.60	128.07
	STD	1.13	0.13	0.99	0.27	0.91	1.09	1.41	0.02
A=3	AVG	132.53	134.95	136.03	137.60	139.54	141.48	142.68	146.19
	STD	1.11	3.70	0.63	0.55	1.27	1.92	0.21	7.57
A=4	AVG	143.34	146.03	154.29	155.38	156.83	158.04	160.09	160.82
	STD	1.18	2.66	1.72	1.11	1.47	0.22	0.92	1.51
A=5	AVG	157.92	162.75	166.50	170.13	173.63	176.29	178.35	182.46
	STD	0.55	0.55	1.09	0.36	1.83	1.58	0.56	3.59
A=6	AVG	190.86	194.59	199.22	201.34	204.57	207.49	209.50	211.31
	STD	0.97	1.27	0.31	0.52	0.17	0.47	0.31	0.61
A=7	AVG	209.39	211.61	217.25	224.72	229.14	231.87	233.08	234.81
	STD	0.46	0.29	0.46	0.62	0.52	0.30	0.80	1.19
A=8	AVG	235.79	241.14	243.35	246.67	250.82	256.68	259.09	259.64
	STD	1.87	1.67	1.53	0.51	2.38	1.82	0.93	0.54

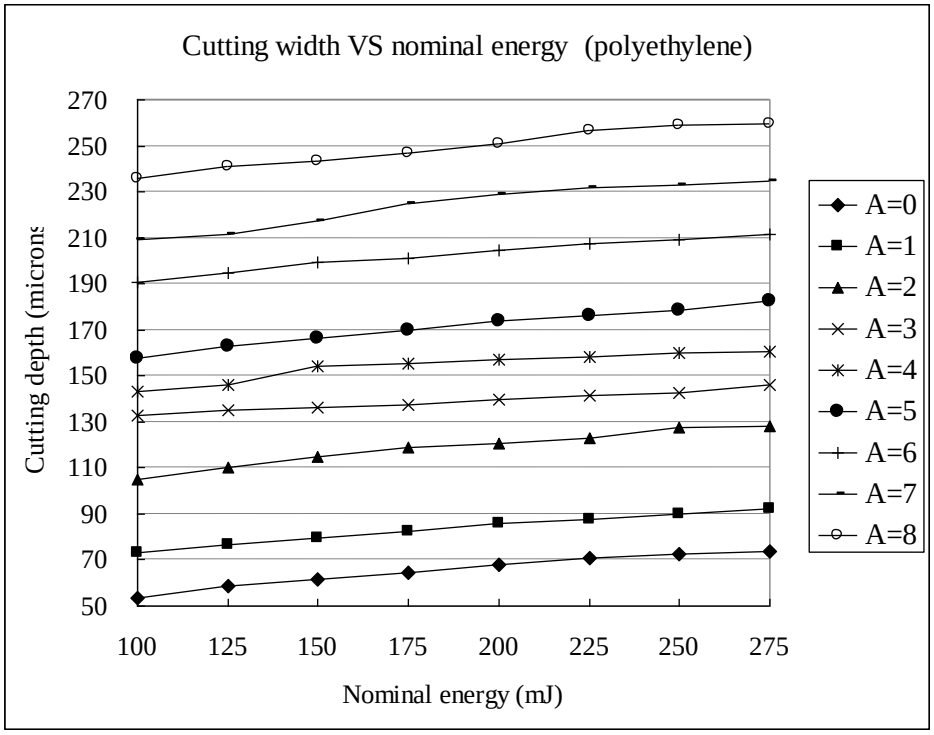

Fig.3.22 Cutting width VS nominal energy (polyethylene)

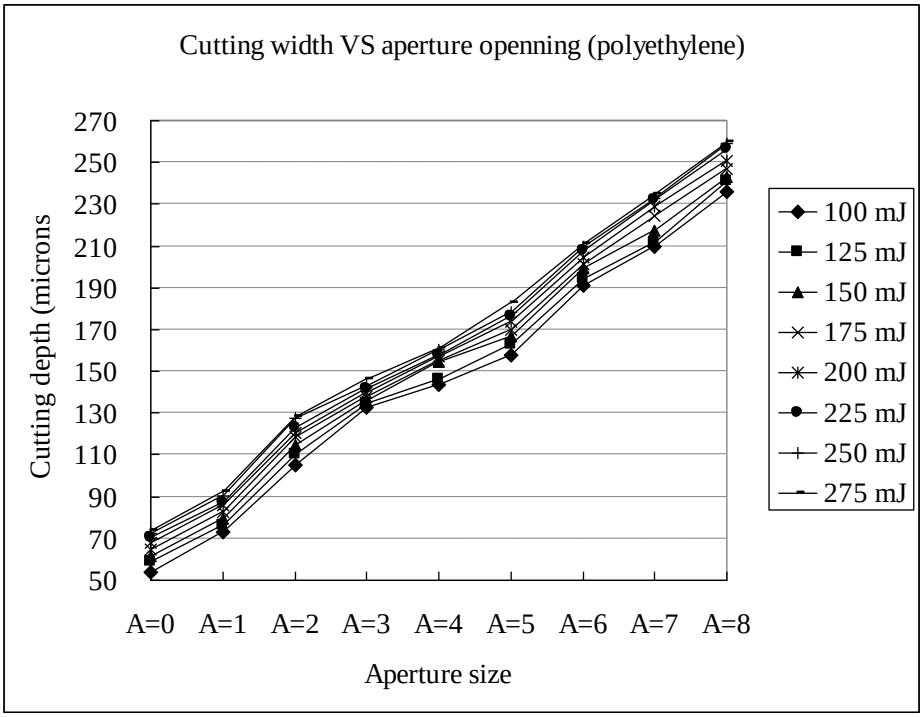

Fig.3.23 Cutting width VS aperture opening (polyethylene)

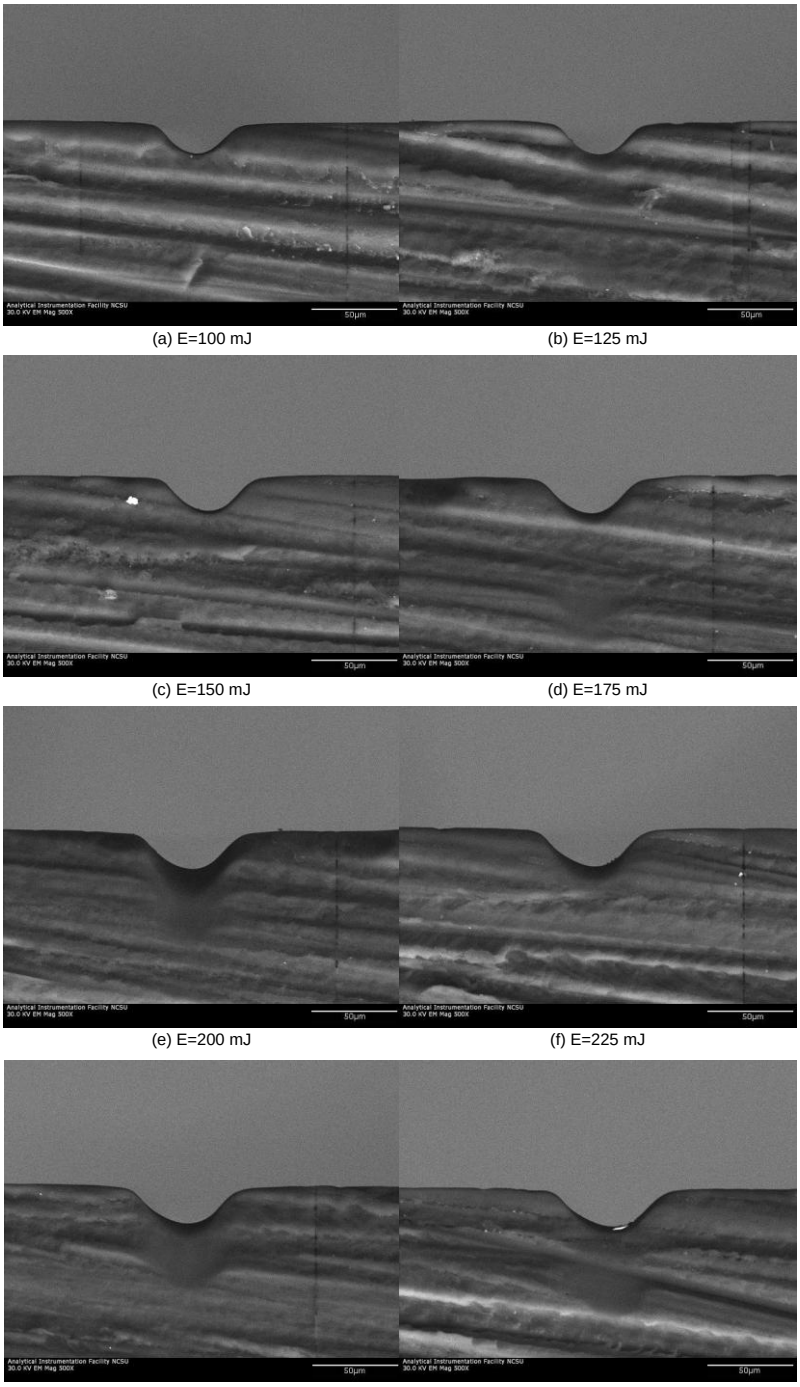

(a) E=100 mJ (b) E=125 mJ

(c) E=150 mJ (d) E=175 mJ

(e) E=200 mJ (f) E=225 mJ

(g) E=250 mJ (h) E=275 mJ

Fig.3.24 SEM images for microchannels on polyethylene (A=0 number of pulse per area=10 and nominal energy ranging from 100mJ to 275mJ):
(a) E=100mJ; (b) E=125mJ; (c) E=150mJ; (d) E=175mJ; (e) E=200mJ; (f) E=225mJ; (g) E=250mJ; (h) E=275mJ. All images are in X500 magnification.

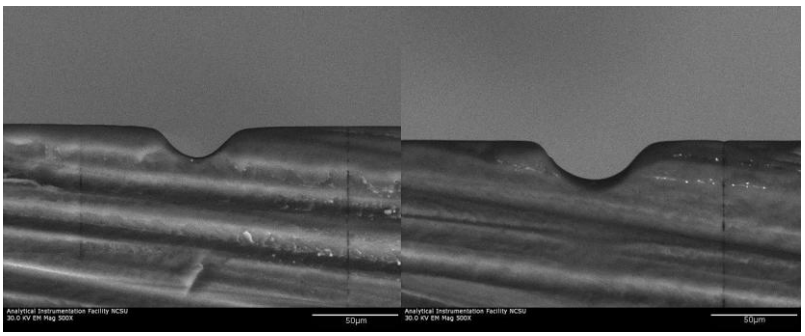

(a) A=0 (b) A=1

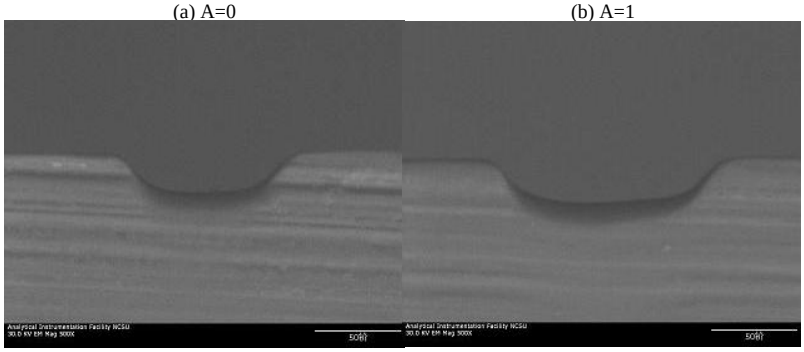

(c)A=2 (d) A=3

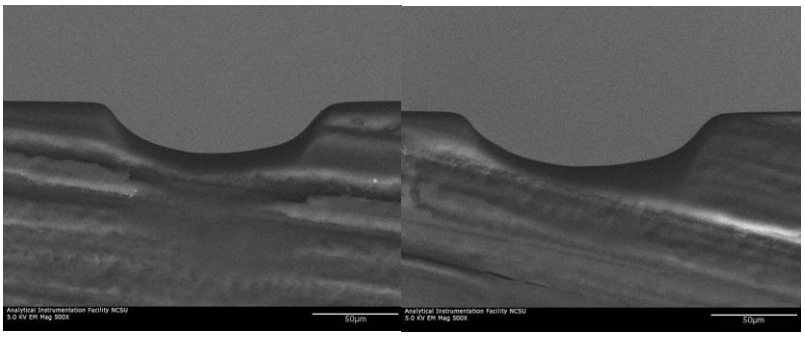

(e) A=4 (f) A=5

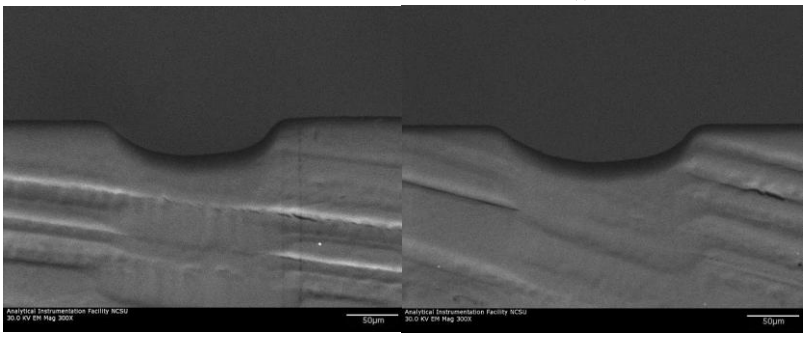

(g) A=6 (h) A=7

Fig.3.25 SEM images for microchannels on polyethylene (E=100mJ, number of pulse per area=10 and aperture opening varying from 0 to 7): (a) A=0; (b) A=1; (c) A=2; (d) A=3; (e) A=4; (f) A=5; (g) A=6; (h) A=7. (g) and (h) are in 300 magnification; while others are in 500 magnification

Similar experiments are carried on PMMA and PDMS, in which the nominal laser changes from 100, 150, 200, to 250 mJ, the aperture openings are adjusted from A=1, 3, 5, to 7 and number laser pulse area is 20. Experiment results can be seen numerically and graphically as follows. Fig.3.30 and Fig.3.37 show an overall view of a set of micro channels on PMMA and PDMS respectively.

Table 3.11 Cutting depth with different laser energy and Aperture opening(PMMA)

Energy (mJ)		100	150	200	250
A=1	AVG	24.25	31.67	37.30	39.37
	STD	0.76	1.57	1.38	0.94
A=3	AVG	41.53	45.83	48.97	53.23
	STD	0.51	2.90	0.96	1.24
A=5	AVG	47.16	52.96	56.95	60.82
	STD	1.44	1.32	2.21	1.28
A=7	AVG	52.00	59.26	62.03	64.45
	STD	2.72	4.12	2.54	2.06

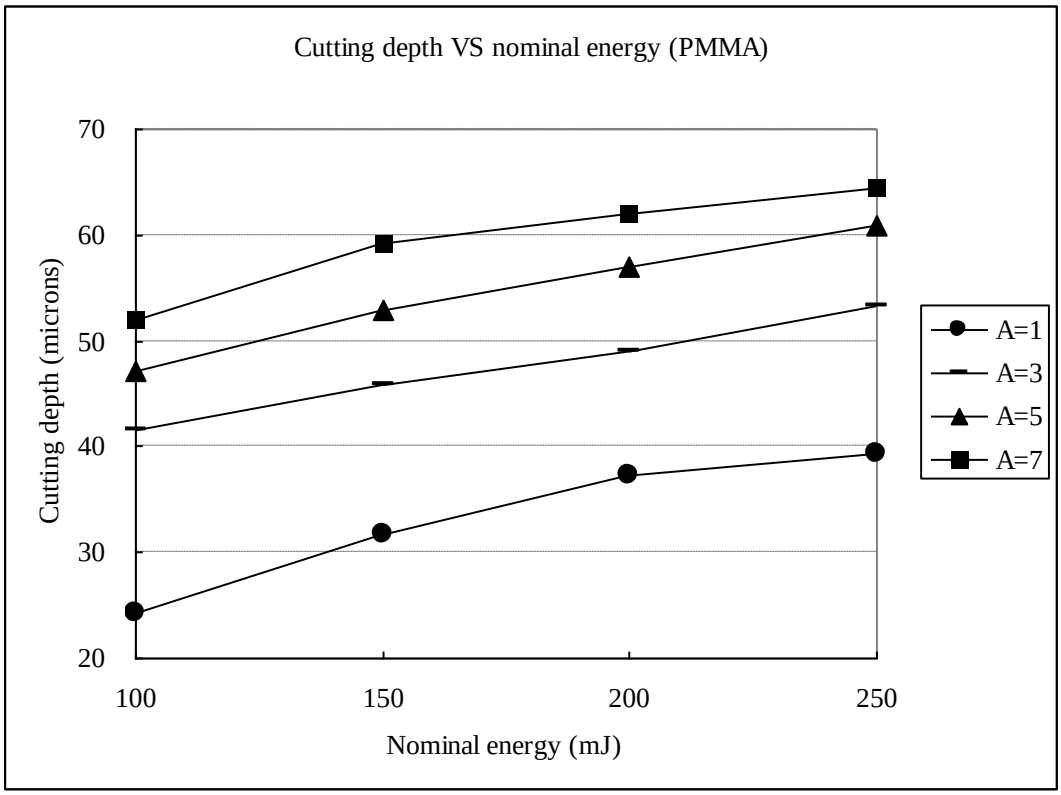

Fig.3.26 Cutting depth VS nominal laser energy(PMMA)

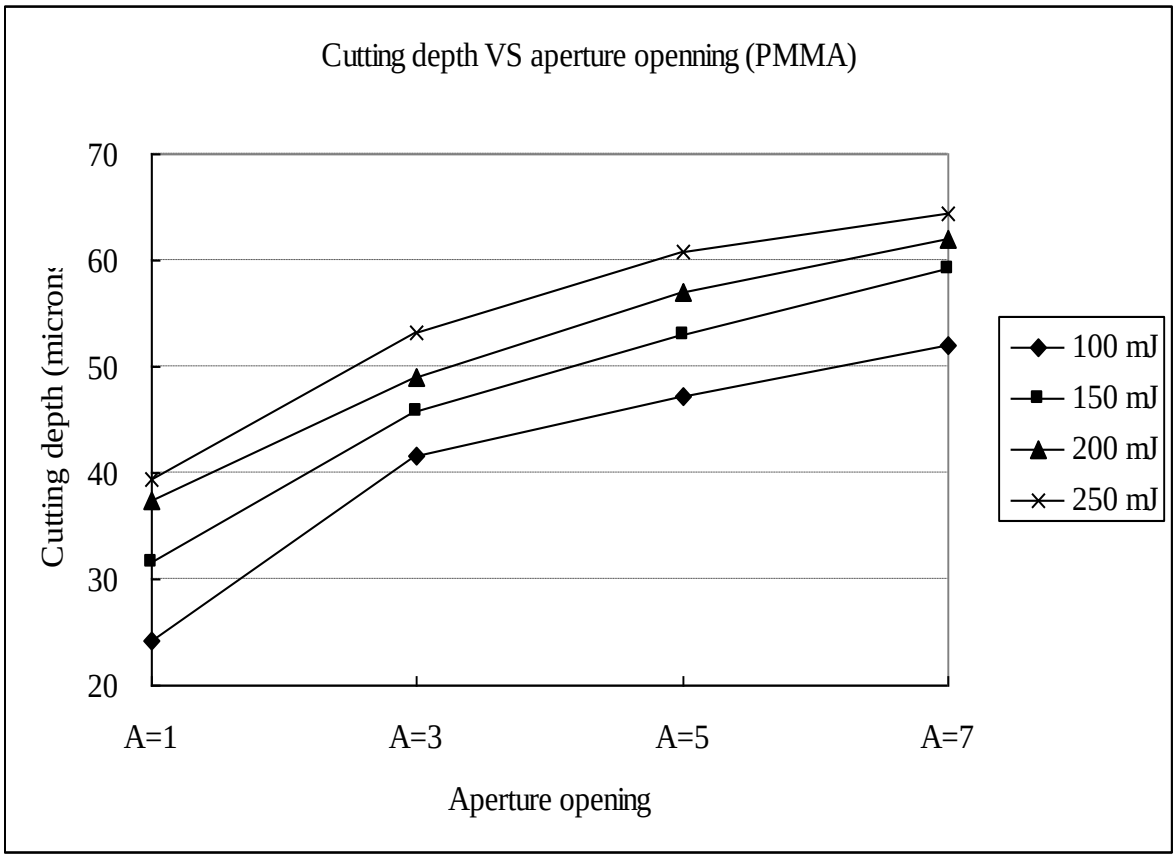

Fig.3.27 Cutting depth VS aperture opening (PMMA)

Table 3.12 Cutting width with different laser energy and Aperture opening (PMMA)

Energy (mJ)		100	150	200	250
A=1	AVG	46.71	55.18	61.07	62.58
	STD	1.11	1.38	2.24	1.42
A=3	AVG	94.71	101.36	104.74	112.05
	STD	1.78	0.36	1.16	1.08
A=5	AVG	132.57	148.49	154.58	161.52
	STD	1.15	1.40	2.88	2.12
A=7	AVG	188.33	192.86	194.95	199.05
	STD	4.34	8.37	1.49	3.46

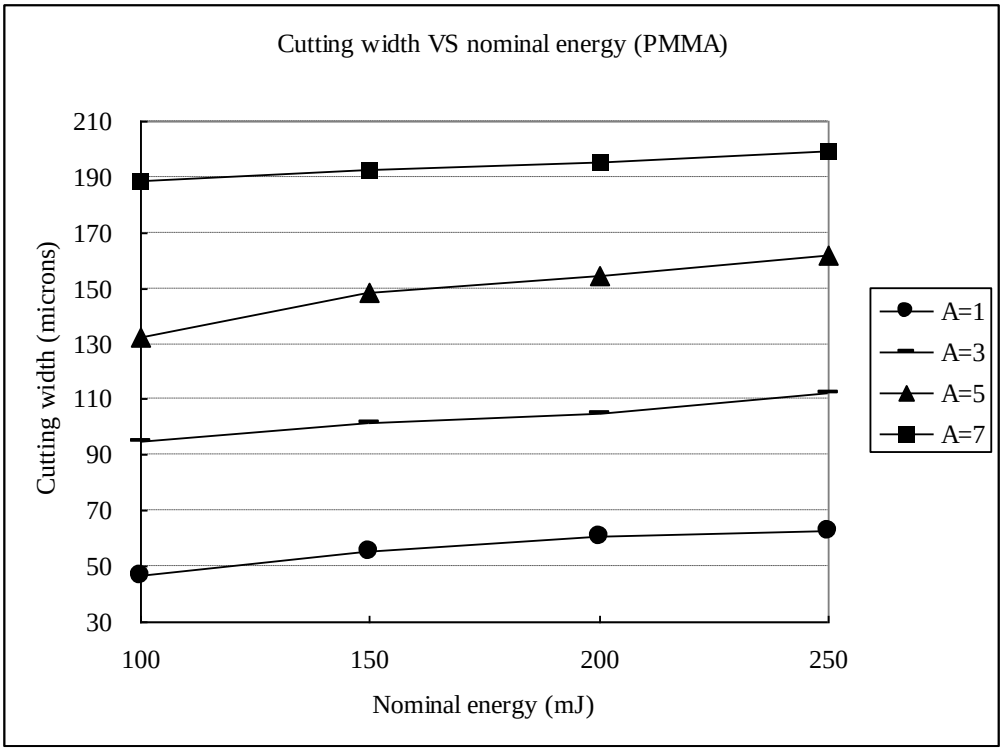

Fig.3.28 Cutting width VS nominal laser energy(PMMA)

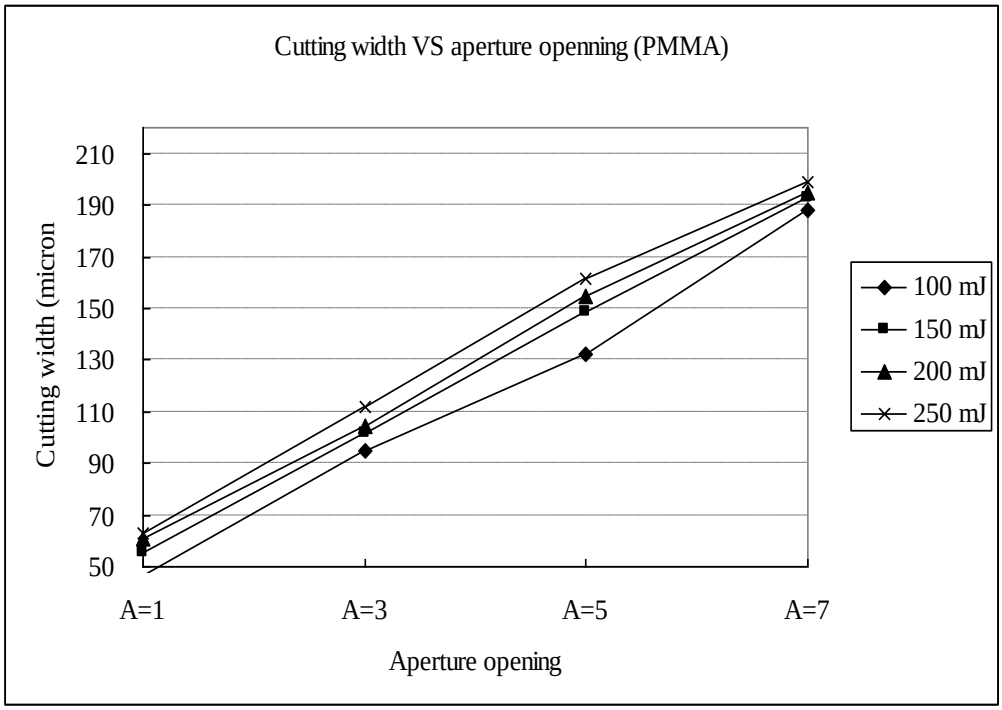

Fig.3.29 Cutting width VS aperture opening (PMMA)

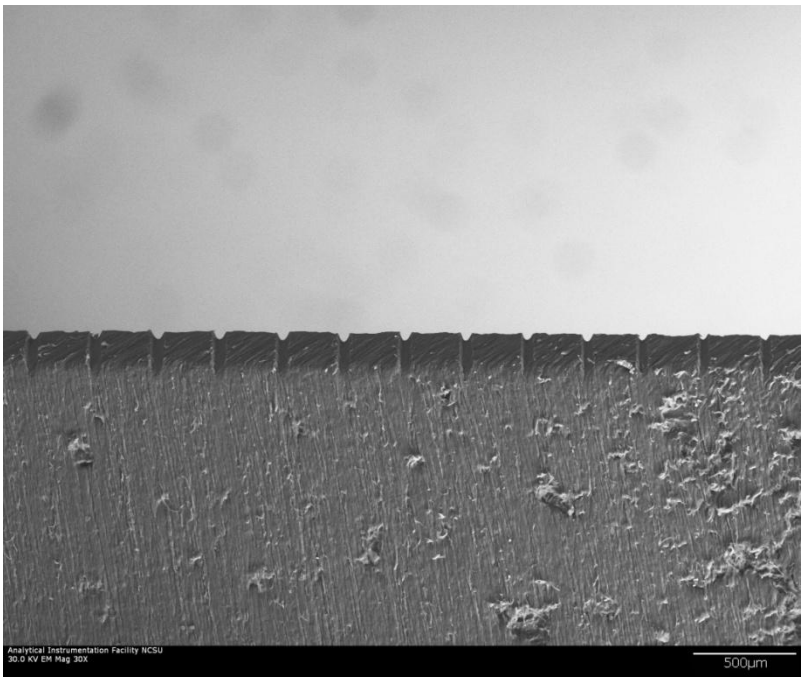

Fig.3.30 Microchannels on PMMA surface: A=1. (from right to left energy ranging from 100, 150, 200 to 250 mJ; there channels made by same energy)

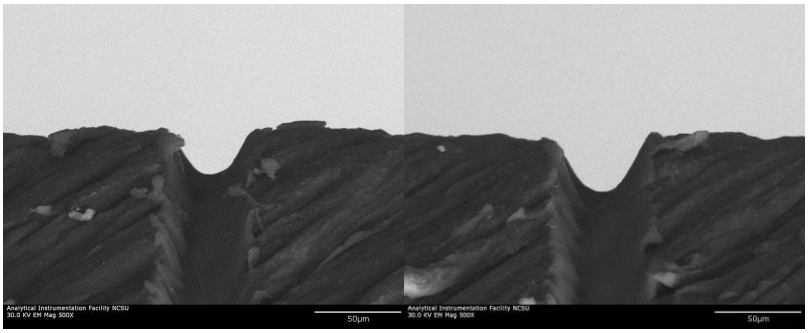

(a) E=100 mJ (b) E=150 mJ

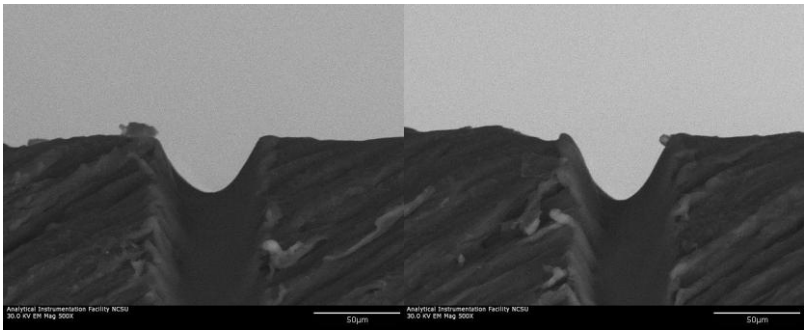

(c) E=200 mJ (d) E=250 mJ

Fig.3.31 SEM images for microchannels on PMMA surface (A=1): (a) E=100mJ; (b)E=150mJ; (c) E=200mJ; (d) E=250mJ.

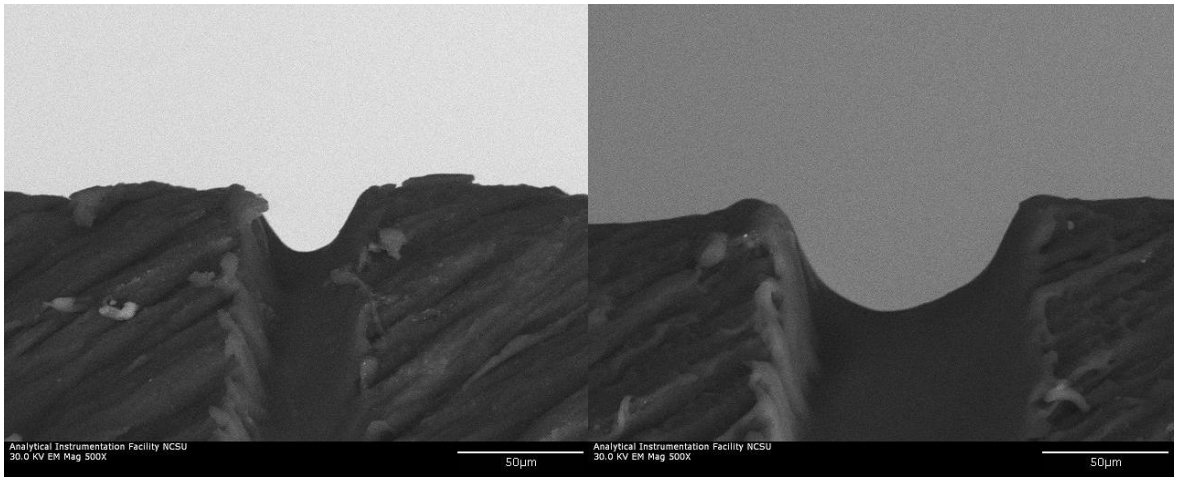

(a) A=1 (b) A=3

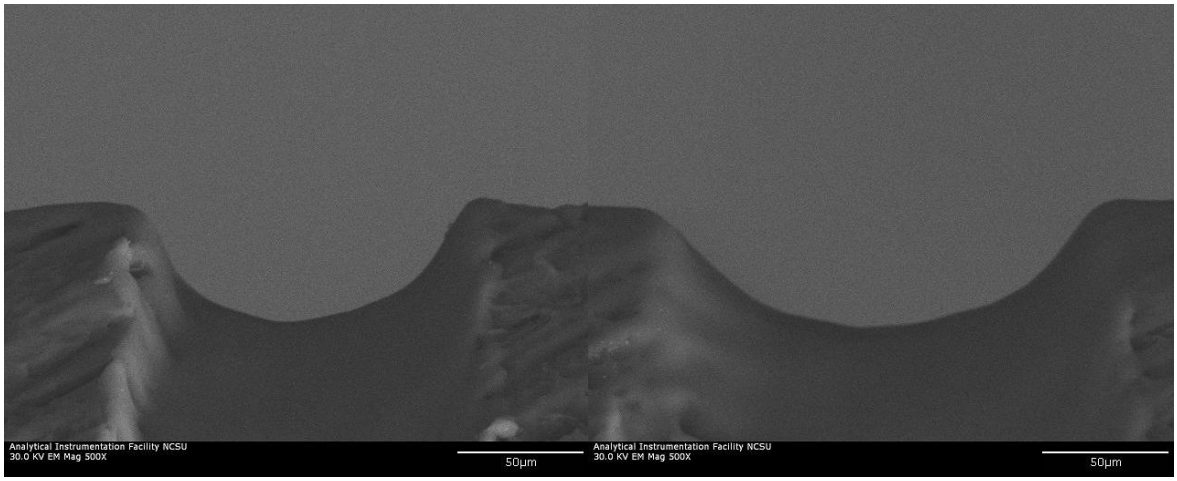

(c) A=5 (d) A=7

Fig.3.32 SEM images for microchannels on PMMA(E=100mJ): (a) A=1; (b) A=3; (c) A=5; (d) A=7

Table 3.13 Cutting depth with different laser energy and Aperture opening (PDMS)

Energy (mJ)		100	150	200	250
A=1	AVG	16.02	20.25	23.76	27.45
	STD	0.64	1.05	0.77	0.28
A=3	AVG	26.66	33.55	40.02	45.28
	STD	0.31	0.77	1.51	0.28
A=5	AVG	35.31	44.07	48.97	54.05
	STD	0.91	1.80	0.96	1.31
A=7	AVG	42.08	52.42	57.31	65.78
	STD	0.72	2.82	1.82	0.92

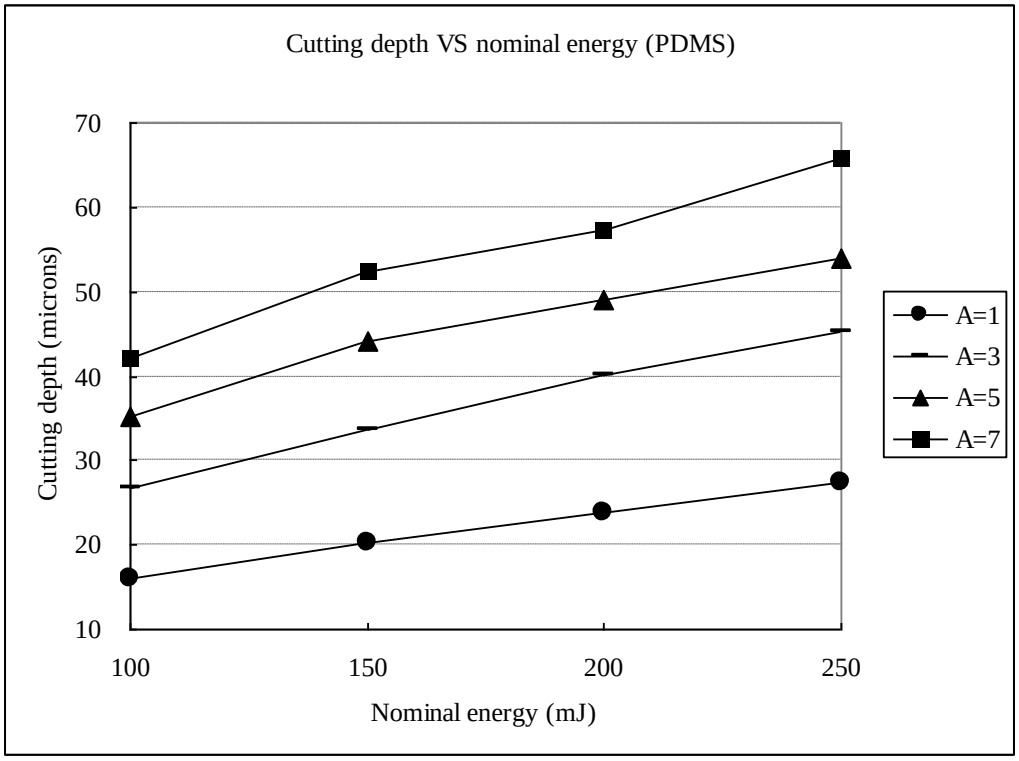

Fig.3.33 Cutting depth VS nominal laser energy (PDMS)

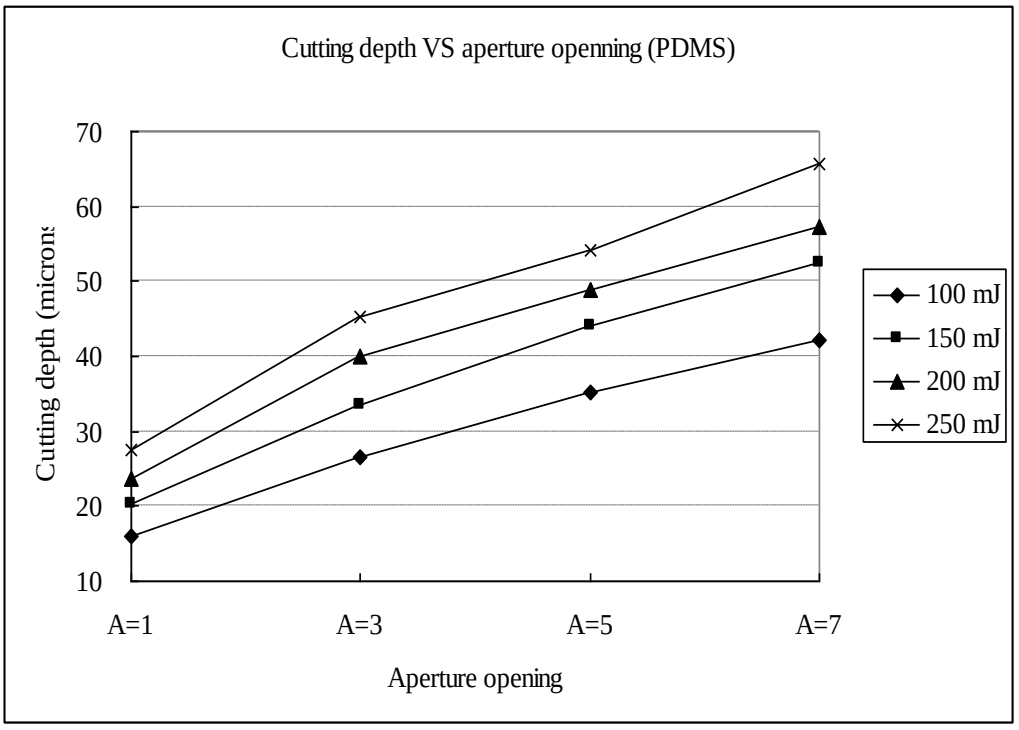

Fig.3.34 Cutting depth VS aperture opening (PDMS)

Table 3.14 Cutting width with different laser energy and Aperture opening (PDMS)

Energy (mJ)		100	150	200	250
A=1	AVG	57.50	63.61	67.47	70.92
	STD	0.79	0.42	0.51	2.14
A=3	AVG	104.05	110.28	114.63	118.01
	STD	0.93	0.52	0.63	1.27
A=5	AVG	152.23	156.71	161.31	164.68
	STD	1.17	0.52	1.47	2.20
A=7	AVG	197.94	201.90	207.61	210.87
	STD	0.76	1.75	1.17	1.79

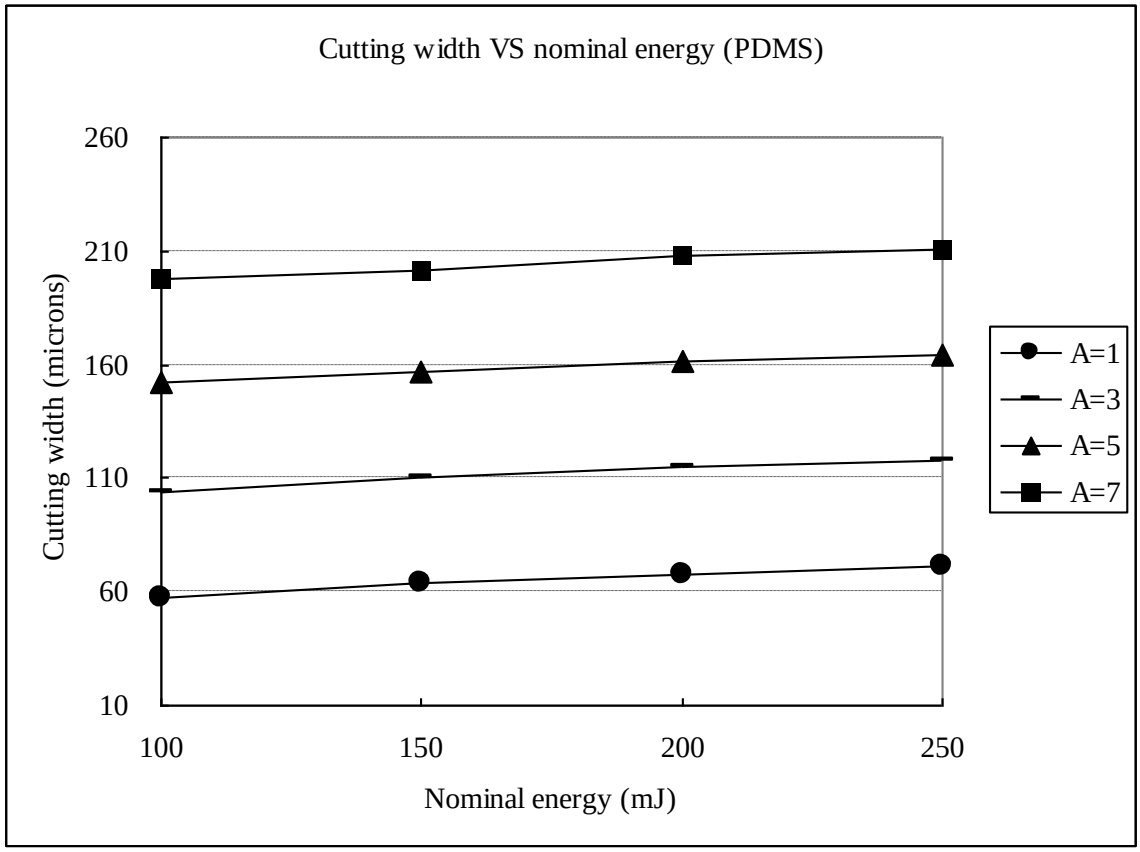

Fig.3.35 Cutting width VS nominal laser energy (PDMS)

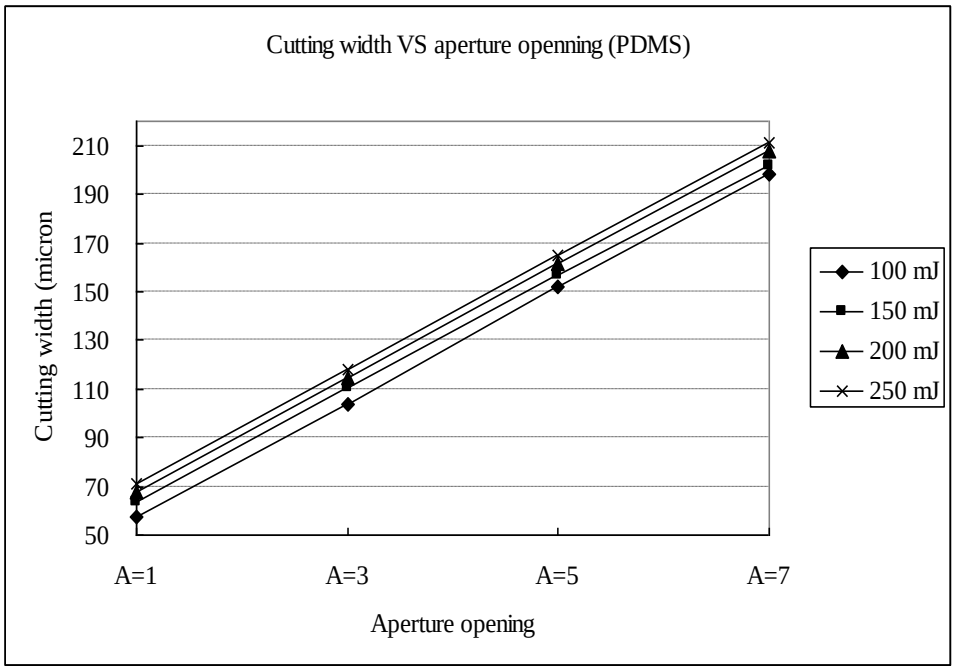

Fig.3.36 Cutting width VS aperture opening (PDMS)

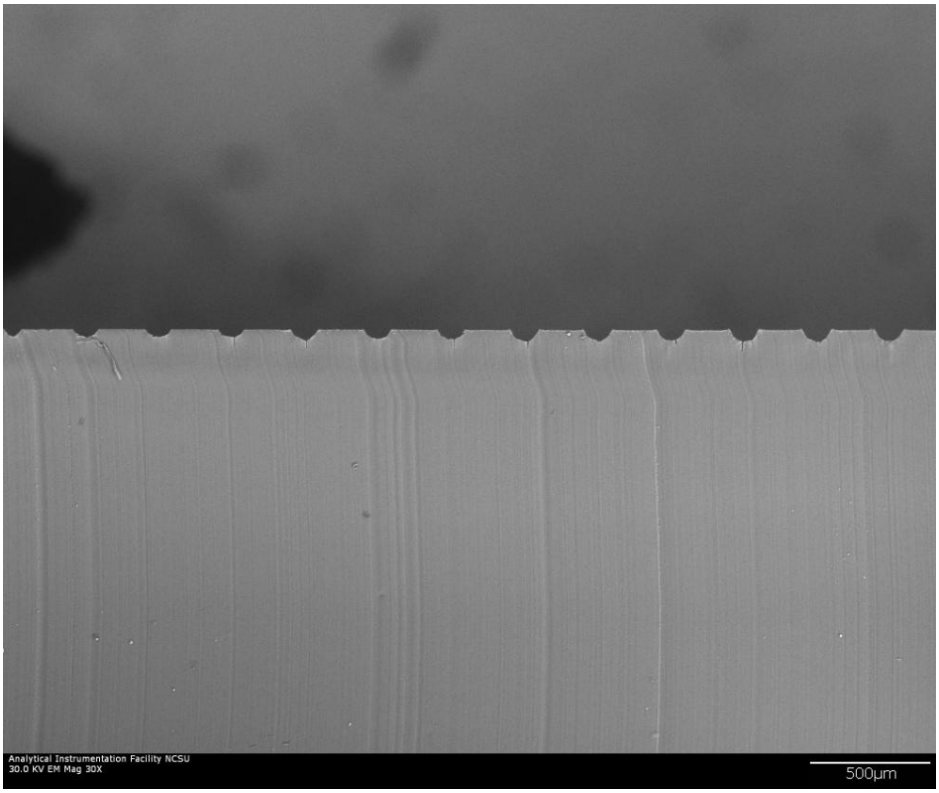

Fig.3.37 Microchannels on PDMS surface: A=3; from left to right energy ranging from 100, 150, 200 to 250 mJ; three microchannels made by each energy value

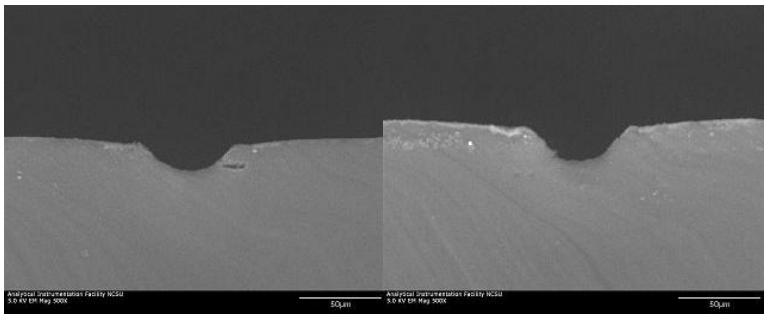

(a) 100 mJ (b) 150 mJ

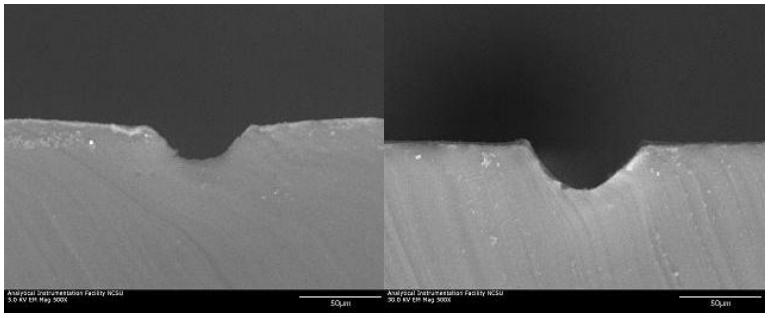

(c) 200 mJ (d) 250 mJ

Fig.3.38 SEM images for microchannels on PDMS (A=1): (a) E=100mJ; (b)E=150mJ; (c) E=200mJ; (d) E=250mJ.

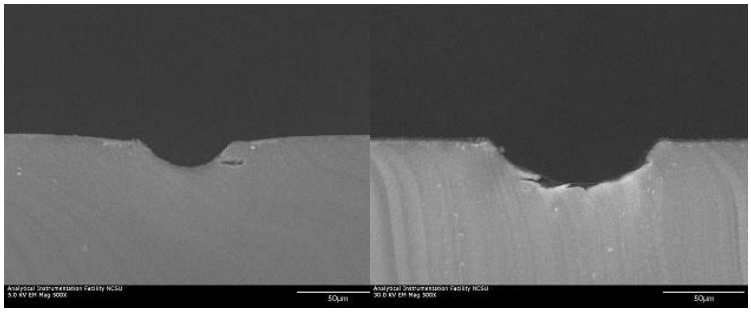

(a) A=1 (b) A=3

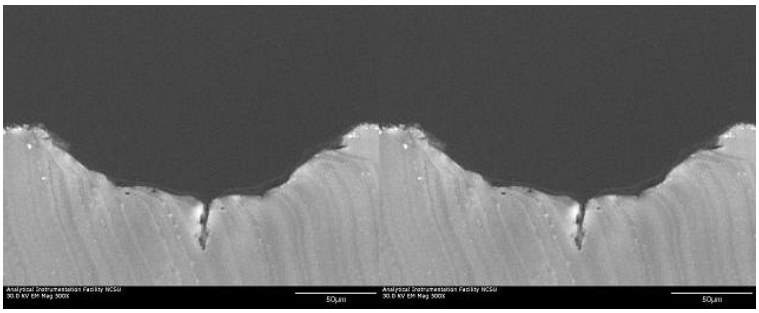

(c) A=5 (d) A=7

Fig.3.39 SEM images for microchannels on PDMS (E=100mJ): (a) A=1; (b) A=3; (c) A=5; (d) A=7.

From the results of three different materials, we found polyethylene and PMMA show better surface quality compared with PDMS. When aperture opening is large (A=3) or energy is high, the surface quality of PDMS drops dramatically. PMMA shows clearer cut on cutting width than polyethylene.

3.5 Summary

We designed three experiments to study the machining performance under different laser parameters for three biocompatible polymers. Based on the comparison, polyethylene and PMMA show better surface quality than PDMS. Laser-ablation depth is linearly dependent on the number of laser pulses per area in our experiments, which is a merit for manufacturing purpose. The quantitative relationship between cutting depth/width and laser energy/laser beam size was built based on statistical results from plenty of experiments. This mapping relationship provides a good basis for proper selection of laser parameters to achieve desirable machining parameters.

CHAPTER 4

MACHINED SURFACE ERROR ANALYSIS IN LASER MICROMACHINING

In Chapter 3, we developed the machining parameters for three biocompatible polymers by our lab-built laser micromachining system. Now we can select the laser parameters based on the desired pattern. From the perspective of manufacturing, surface quality is one of the key issues to make a good product. In this chapter, we will discuss the machined surface errors in laser micromachining. We will start from the laser energy profile and cutting performance on materials. Then the sources of machined surface errors will be discussed. The overlapping effects in laser micromachining, which is one of the machining error sources of laser micromachining different with other manufacturing processes, will be presented. A model will be proposed to calculate the machined surface errors in laser micromachining with the experiment and simulation results presented. A summary will be given in the end.

4.1 Introduction

4.1.1 Mechanism and application of laser micromachining

As manufacturing in micro scale becomes a trend in various industries including telecommunication, biomanufacturing, MEMS and biomedical applications, laser micromachining draws more and more attention from academia and industry. Laser micromachining is based on the removal of material with short but intense laser pulse due to the absorption of laser energy into the materials. When a laser beam is being shot onto the material surface, if the fluence of the laser beam is high enough to reach or surpass the threshold value (F_{th}) which is required for material to decompose, the material decomposition

will occur. Due to this contactless characteristics laser micromachining is a great tool in some applications where contamination must be avoided. Many materials can be used in laser micromachining ranging from metals, ceramics to polymers. This makes laser micromachining a good candidate in many occasions.

4.1.2 Numerical modeling on laser ablation process

The limited machining efficiency, uncertain energy loss, complex and expensive laser delivery systems, and irregularity of the cutting shape by laser pulses are the drawbacks for some applications. Due to the uncertain energy loss, complex optical system and material-dependent machining performance, it's very hard to do quantitative analysis on laser micromachining behaviors. Some research has been done to explore the mechanism of laser micromachining and built the numerical model to analyze the ablation behavior. In [Patterson 1999], a numerical model had been built to predict cutting behavior of laser micromachining including cutting depth and wall angles of trench structure ablated. This two-stage model involves calculation of the radiation distribution incident on the surface of the partially formed structure and modeling the ablation and removal of material from the surface. This model considered the surface propagation by continuous laser pulses, which is normal in laser micromachining. The experimental results and predicted results had been compared. They agreed with each other very well except lowest and highest energy. In [Gai 1992], authors studied the mechanism of interaction between laser radiation and materials. It exploited quantum mechanical process of ultraviolet photon absorption and molecular dynamics techniques to obtain a model for ablation of polymer surface. Their model showed repulsive antibonding electronic potential energy surfaces is crucial to understand the ultraviolet ablation process at 193 nm wavelength compared with other effects like intense local heating of material by longer wavelength lasers.

4.1.3 Applications of CAD/CAM in laser micromachining

Integrating the CAD/CAM into laser micromachining system shows great potentials and

becomes a trend in laser micromachining. CAD/CAM can help laser micromachining discard the trial-error method to obtain desirable structure. Instead, a more efficient and accurate approach can be provided by CAD/CAM tool. In almost all the current laser micromachining system, basic CAD/CAM is carried. Along with high resolution controller, the CAD/CAM module in laser micromachining system, which generally accepts G-code as input, can provide accurate positioning and motion in a predefined pattern. Some advanced CAD/CAM tools and numerical models for CAD/CAM purpose are also developed for special uses. In [Choi, 2004], mask was utilized to control the laser energy shooting on material surface. Through the various sizes of holes on mask, different cutting depth can be achieved. A numerical model had been built to represent the relationship between size of holes on mask and cutting depth. So given a depth in 3 dimension, a hole diameter would be calculated on 2 dimensional mask based on numerical model. In [Mutapcic 2006], a CAD/CAM system for excimer laser micromachining was introduced. The function of CAD/CAM system was very similar to convention CAD/CAM system including importing standard CAD files, triangulation of object surfaces, slicing the CAD models and generating NC code for tool path and mask layout design. By exploiting the system, authors studied the laser influence, pulse repetition frequency and the number of shots per area to optimize the wall angle and ablation depth. This paper also investigated the stitching error in laser micromachining. To minimize the stitching error, the overlap size was calculated and various shapes of masks were tested.

4.1.4 Related work in machined surface error analysis for laser micromachining

In traditional CAD/CAM research, surface error analysis is one the major parts of the research work. Surface roughness is directly determined by surface errors. Surface error analysis can help the process planning decision. A systematic methodology was proposed in [Lee 1996&1997] for surface error analysis in 5-axis machining. This method provided a general solution for surface error analysis considering different cutter shapes, part surface

geometry, and orientation of cutters. The machined surface error analysis in laser micromachining has not been fully addressed yet. The overlapping effects and stitched error were discussed in [Mutapcic 2003&2006]. In [Mutapcic 2003] machined surface errors caused by overlapping between two adjacent pulses for UV laser ablation on polycarbonate surfaces were studied. The overlay peak errors which are the materials left on part surfaces and overlay trough errors which are caused by penetration into part surfaces by laser pulses were investigated. The overlapping, wall angle, and number of shots per area are the main parameters to determine the peak and overlay errors. However, they didn't give a general numerical model to predict the machined surface errors for most natural laser energy profile. They also didn't consider the smaller number laser pulses per area. Their model needs lots of experiments to find the optimal parameters resulting in the minimal machined surface errors. In [Mutapcic 2006], they applied this method in a CAD/CAM tool.

4.1.5 Organization of this chapter

In this chapter, machined surface errors in laser micromachining will be studied. A model to calculate and predict the machined surface errors will be proposed. The remaining sections of this chapter will be organized as follows. In section 2, the shape and energy profile of laser beam and their roles in machined surface errors analysis will be introduced. In section 3, machined surface errors in machining will be explained and the sources of machined surface errors will be analyzed. As one of the sources causing machined surface errors, geometric error will be analyzed and calculated in section 4. Another source, overlapping effect in laser micromachining, will be studied in section 5. A model to calculate the machined surface errors considering the overlapping effect will be proposed in this part. Then the experiment results will be shown. The comparison of experiment result and simulation based on the proposed model can be seen in section 6. Finally a conclusion will be given at the end.

4.2 Shape and Energy Profile of Laser Beam.

Machined surface errors have been extensively studied for conventional machining including CNC machining. Geometry of cutters, orientation of cutters and geometric features on machining part surfaces are main factors to analyze machined surface errors in CNC machining. There is no real cutter in laser micromachining since materials are removed by energy of laser pulses. Technically, the light is the virtual cutter. The shape and the energy profile of laser beam are the counterpart of cutters' geometry in CNC machining， which directly determine the shape of etched cavity on material surfaces. Thus, to understand the shape and energy profile of a laser beam is important for investigation of the machined surface errors and surface roughness in laser micromachining.

4.2.1 Normally distributed laser beam energy profile

As mentioned in previous section, there are many types of lasers with different gases available in the market including high power infrared Nd: YAG and CO_2 lasers which are mainly used in industry and excimer lasers which emit in the UV range 157-355 nm depending on gases. Some lasers including CO_2, Copper vapor, Ti: Sapphire and Nd: YAG emit normally distributed or nearly normally distributed energy profile of laser beam with circular cross section. Fig.4.1 (a) and (b) present the cylindrical shape of laser beam and the energy profile in one direction on a cross section plane of the laser beam. The energy profile looks like a bell-shape curve. Laser fluence on this energy profile can be approximately defined as:

$$F(x) = F_{\max} e^{-\frac{x^2}{2\sigma^2}} \qquad (4.1)$$

where $F(x)$ is the fluence on one point of the laser profile curve;

F_{max} is the maximal fluence in this laser beam which is the center of cross section plane;

x is the x value along one direction on the cross section of laser beam in Fig.4.1(a);

σ is the range that laser beam spread over. In this case $\sigma = \frac{x_{\max} - x_{\min}}{6} = D/6 = R/3$, where D is the dimension of the laser beam. Outside D, laser energy is small enough to be neglected.

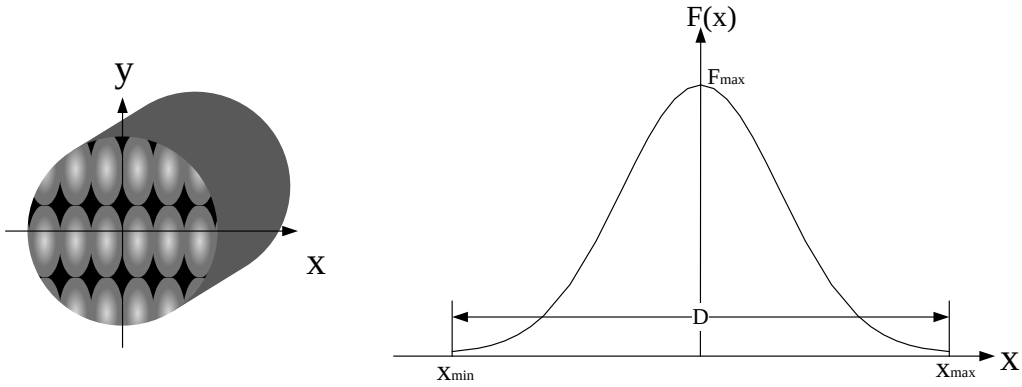

(a) Laser beam (b) Normally distributed energy profile

Fig.4.1 Cylindrical laser beam and normally distributed energy profile

For lasers with this cylindrical shaped output beam and normally distributed energy profile, the laser beam can be focused to a very small spot. It's flexible to control and make complex geometric patterns. However, due to the small size of spot, it is very time-consuming when you are trying to machine large areas where bulky materials will be removed. Fig.4.2 shows some circular cavities on silicon wafer ablated by the laser discussed above.

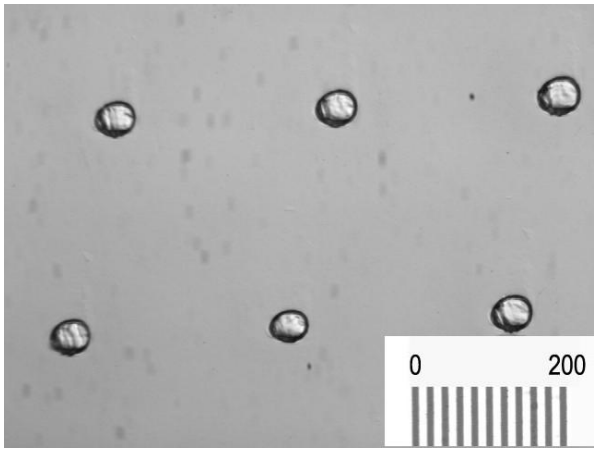

Fig.4.2 Circular spot on silicon wafer

4.2.2 Multimode laser beam energy profile

For TEA CO_2 and excimer laser, the shape of the beam is cuboid and the energy profiles on a cross section plane of laser beam are different in length and width directions. In one direction the energy profile is normal distribution or nearly normal distribution just like CO_2, Copper vapor, Ti: Sapphire and Nd: YAG lasers. In the other direction, the energy profile can be approximately described as equation (4.2) with top-flat function in the center and normally distributed function on both ends.

$$F = \begin{cases} F_{\max} & x^- \le x \le x^+ \\ F_{\max} e^{-\frac{(x-x^-)^2}{2\sigma^2}} & x_{\min} \le x \le x^- \\ F_{\max} e^{-\frac{(x-x^+)^2}{2\sigma^2}} & x^+ \le x \le x_{\max} \end{cases} \qquad (4.2)$$

where $\sigma = \frac{x_{\max} - x^+}{3} = \frac{x_{\min} - x^-}{3}$. The shape of one cross section of the laser beam and the energy profile in both directions are shown in Fig.4.3 (a), (b) and (c) respectively. With this type of energy profile and beam shape, the laser beam cannot be focused on one small circular spot but a rectangular-like shape with half oval on each end which is shown in Fig.4.4. Due to the shape of spot, it is not as easy as circular spot shape to make complex geometry. However, it's suitable to remove material in large areas due to its relative larger focused beam size. For some channels or reservoir patterns this laser beam and energy profile even naturally fit.

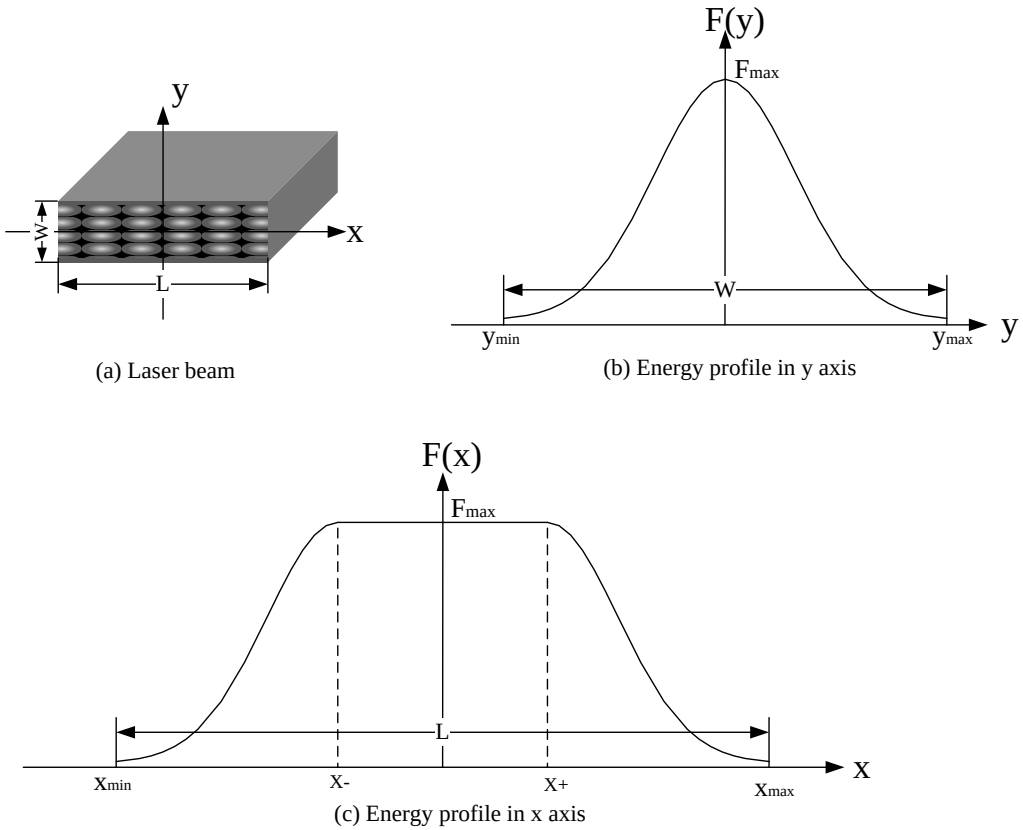

Fig.4.3 Laser beam with multimodal distribution energy profile

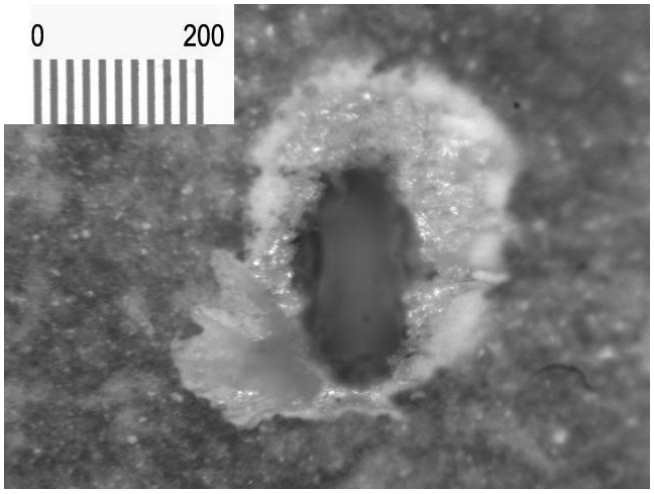

Fig.4.4 Cavity etched by excimer laser with multimode energy profile on lab-made PLA

Since the laser beam with multimodal energy profile is not favorable for patterns with

complex geometry and normally distributed energy profile is time-consuming for bulky material removal, some homogonous optical devices are developed to make the energy distribute more evenly and take advantages of both types of energy profiles. Laser beam homogenizer is one of those devices. It can change energy profile of a laser beam into a more even distribution almost without energy loss via reduce the standard deviation of laser energy over the beam area. Homogenizers split up the beam and then superimpose them in the mask plane by using optical devices. The homogenized energy profile is very similar to top-flat function in equation (4.2) but more evenly distributed with larger flat area. If aperture is utilized only to filter out the top-flat part of laser beam, the side wall could be vertical. Thus, via homogenizer device, we can acquire well-formed circular focused spot with larger dimension but much more evenly distributed energy profile.

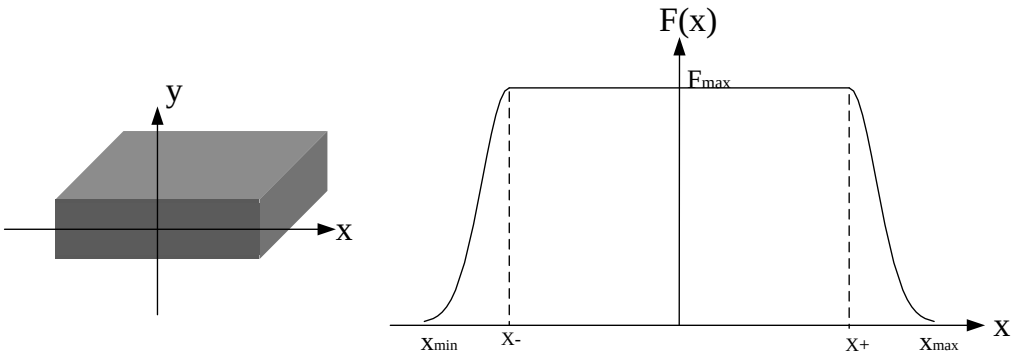

(a) Laser beam (b) Energy profile in both directions

Fig.4.5 Homogenized laser beam and energy profile

4.2.3 Cutting shape by laser beam on material surfaces

Several types of output laser beams have been discussed. Each of them results in a unique etched cavity on material surfaces. Since ablation happens only when the laser fluence reaches the threshold value F_{th}, the ablation occurs when $x \in [-x_{th}, x_{th}]$ in Fig.4.6 which shows the one cross section of cavity along any direction for circular laser beam with normally distributed energy profile and only width direction for multimode laser beam. Apparently the opening of the etched cavity is smaller than the area of cross section of laser beam.

According to Bear-Lambert law, if we assume the reflection by the material surface is negligible, etched depth given a material and laser fluence can be calculated as

$$d = \frac{1}{\alpha} \ln \frac{F}{F_{th}} \tag{4.3}$$

where α is the absorption coefficient of a particular material. The ablation will automatically stop at the depth where the local fluence has dropped below F_{th}.

For normally distributed energy profile (on any direction of circular laser beam or only width direction of multimode laser beam), we can calculate the depth etched by laser pulses based on equation. 4.1 and equation. 4.3 as follow.

$$d(x) = \frac{1}{\alpha} \ln \frac{F_{\max} e^{-\frac{x^2}{2\sigma^2}}}{F_{th}} = \frac{1}{\alpha} (\ln \frac{F_{\max}}{F_{th}} - \frac{x^2}{2\sigma^2}) \quad x \in [-x_{th}, x_{th}] \tag{4.4}$$

The cross section of etched cavity along one axis of laser beam and its corresponding laser energy profile are shown in Fig.4. 6.

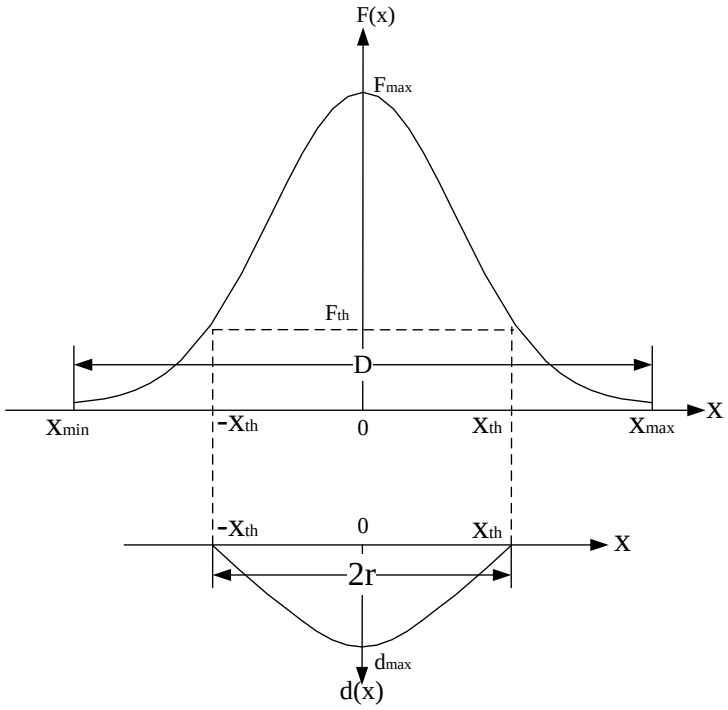

Fig.4.6 Cutting depth by laser beam with normally distributed energy profile

According to Fig.4.6 and Equ.4.4, the etched depth by laser pulses with normally distributed energy profile can be represented as a quadratic function and the cross section of the etched cavity along one axis of laser beam can be described as a quadratic curve.

4.3 Sources of Machined Surface Errors in Laser Micromachining

4.3.1 Overlapping effects between two adjacent laser pulses

To improve the surface roughness ablated by laser pulses, we need to understand machined surface errors by laser micromachining. For conventional machining processes, the machined surface errors are caused by the interaction between part surfaces and cutters. The cusp left over on part surface can be determined by the physical shape and orientation of cutters, tool path planning and local geometric features on part surface.

Although there is no real cutter in laser micromachining compared with conventional machining processes, geometric errors still exist due to the shape of cavities etched by laser pulses and the tool path planning. Another source of machined surface errors of laser micromachining is the overlapping effects by adjacent laser pulses. In laser micromachining, to achieve maximal laser fluence, laser beam has to be focused on a small spot to ablate more materials. Beyond the focal plane, laser beam spreads diffusively like shown in Fig.4.7 (a). If we only consider the region where the laser ablation happens, the propagation path of laser beam is very small. Thus we can assume there is no energy loss along laser propagation path in this confined region. On each cross section of laser beam along the propagation path, the total laser energy is constant and energy is normally distributed. If on focal plane, the energy profile is $F(x) = F_{\max} e^{-\frac{x^2}{2\sigma^2}}$ and one other cross section the energy profile is $F(x)' = F_{\max}' e^{-\frac{x^2}{2\sigma'^2}}$, the following relationship is always kept under our assumption.

$$\int_{-\infty}^{\infty} F_{\max} e^{-\frac{x^2}{2\sigma^2}} = \int_{-\infty}^{\infty} F_{\max}' e^{-\frac{x^2}{2\sigma'^2}} \qquad (4.5)$$

Apparently F_{max}' is less than F_{max}. The energy profiles on focal plane and a cross section are

presented in Fig.4.7 (b) and (c) respectively.

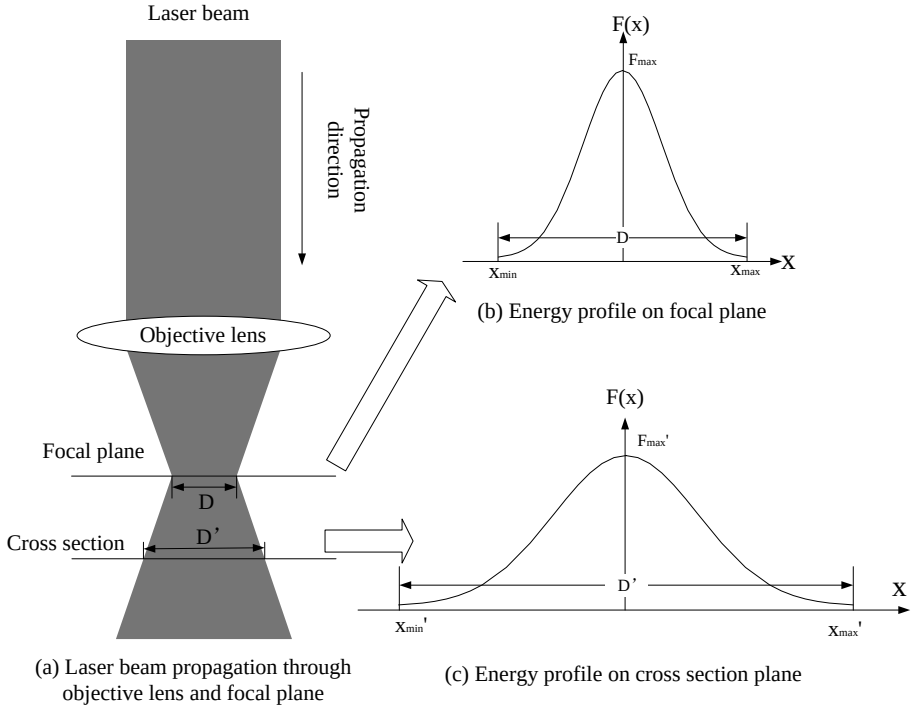

Fig.4.7 Laser energy profile on the focal plane and beyond the focal plane

Due to the characteristics of laser propagation through the objective lens and focal plane, when adjacent laser pulses overlap with each other, some portion of the laser beam will be shooting on the surface that was already ablated by previous laser pulse. Fig.4.8 (b) presents the overlapping by two adjacent laser pulses.

4.3.2 Machined surface errors caused by overlapping effects

As shown in Fig.4.8 (b), if the fluence of the portion of laser beam shooting on the machined surface is over threshold value F_{th}, further ablation will happen on the cavity surface which was already ablated by adjacent laser pulse. Without considering the overlapping effects, the cusp left over on material surface by two adjacent laser pulses is like Fig.4.8 (a). Fig.4. 8(c) shows how the overlapping between adjacent laser pulses has effects over the geometric errors. As shown in Fig.4.8 (c), the cusp height caused by pure geometric

error Δh changes to Δh' due to the overlapping effects by adjacent laser pulses. Coupling overlapping effects with geometric error, the cusp height by adjacent laser pulses can be calculated.

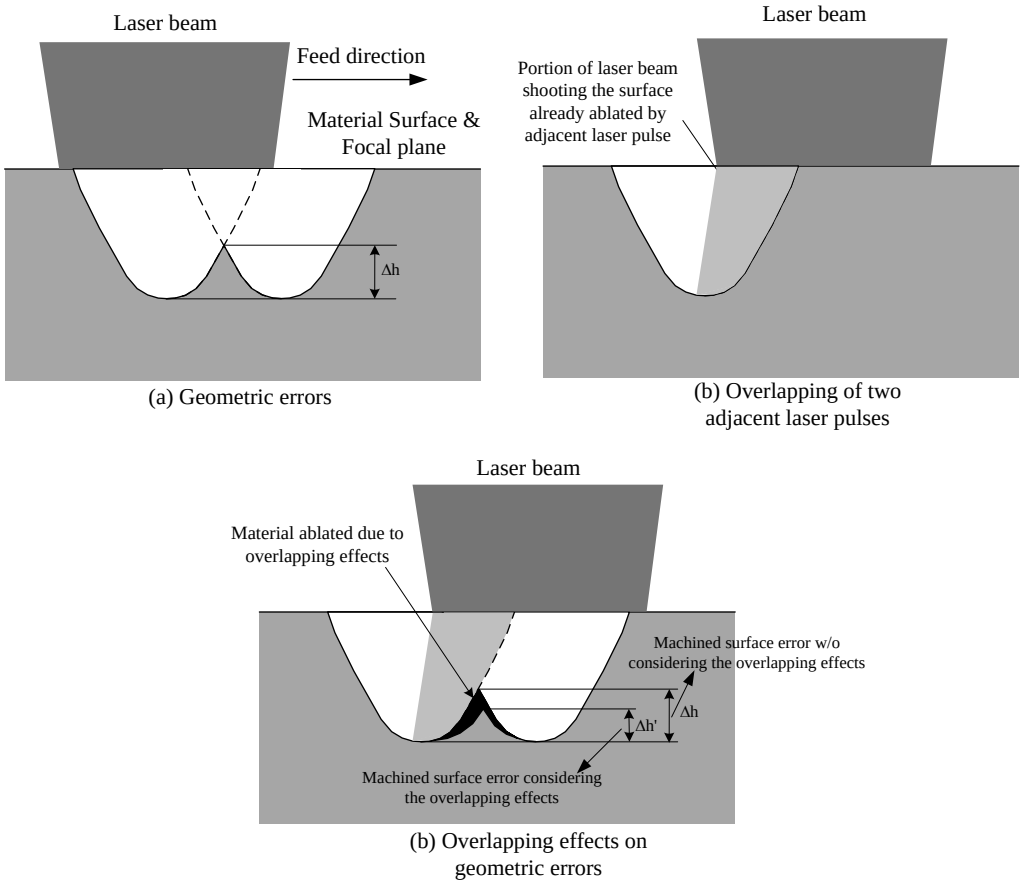

Fig.4.8 Overlapping between adjacent laser pulses and its effects on surface error

In the following two sections, the geometric errors and overlapping effects in laser micromachining will be discussed respectively. The combination of these two factors explains the surface errors in laser micromachining.

4.4 Analysis of Geometric Errors in Laser Micromachining

4.4.1 Geometric errors in laser micromachining

Similar to conventional machining, the geometric errors are caused by two adjacent

cutter locations. In laser micromachining the laser pulse is the counterpart of cutter in conventional machining. The cusp height left on the material surface by adjacent laser pulses determines the quality of surface and is critical for selecting laser micromachining parameters like feed rate, interval between adjacent cutting paths and distance between adjacent cutting surfaces in process planning. Given specific surface quality requirements, the cusp height should be maintained within an allowable tolerance. So the geometric errors need to be calculated and predicted for laser micromachining process planning to achieve satisfied surface geometry.

According to the source of geometric errors, we can define three types geometric error in laser micromachining.

Definition 1: *Type I error*

Due to the discontinuity of laser pulses, on the same cutting path materials are left between two adjacent laser pulses shooting on the material surface. We define this kind of machined surface errors as Type I error. In this case, the distance between two adjacent laser pulses depends on the frequency of laser pulses and the feed rate.

Definition 2: *Type II error*

Type II error is caused by the interval between adjacent cutting paths on the same cutting surface.

Definition 3: *Type III error*

Type III error is the most complex one in laser micromachining. It is caused by the adjacent cutting paths on adjacent cutting surfaces and local surface geometry.

These three types of machined surface errors are show in Fig.4.9 (a), (b) and (c) respectively.

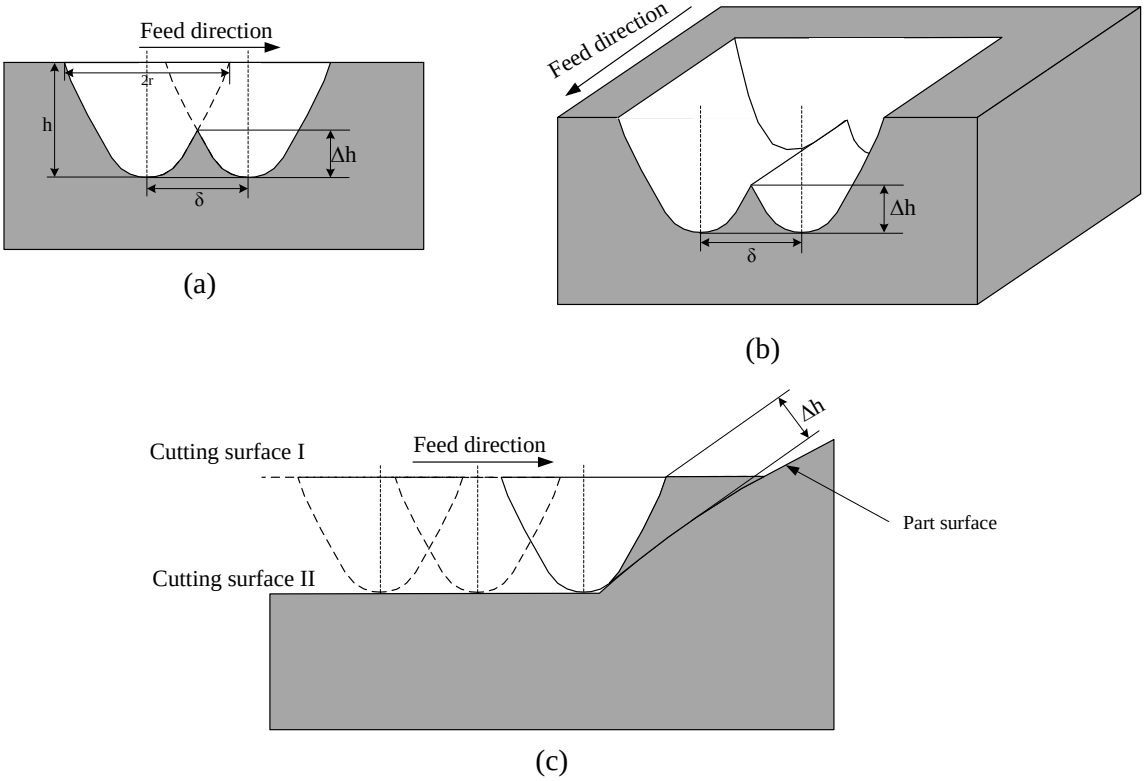

Fig.4.9 Definitions of geometric errors for laser micromachining: (a) Type I error, caused by discontinuity of laser pulses, (b) Type II error, caused by interval of two adjacent paths on the same cutting surface, and (c) Type III error, caused by two adjacent cutting paths on different cutting surfaces.

In the following sections, we will analyze the three types of geometric errors and discuss the calculation of cusp height left over part surfaces.

4.4.2 Calculation of Type I & II geometric errors

Type I and II geometric errors are calculated in the similar way. The difference lies in how the distance between adjacent laser pulses is determined. As mentioned above, the type I geometric error is caused by the discontinuity of laser pulses. Laser scriber shoots the laser pulses on material surfaces with a specific frequency. Meanwhile the platform controlled by computer moves the part along *X*, *Y* and *Z* axes synchronously. So distance between adjacent laser pulses in the type I error is determined by equipment-dependent parameters including

frequency of laser pulses (*f/sec*) and feed rate of platform (*Fr mm/sec*). While in type II error, the distance between adjacent pulses is given by process planning. To calculated type I and type II errors, some material-dependent parameters has to be known including opening of the cavity etched by a single laser pulse (r_{spot} *mm*) and etch depth (*h mm*).

To calculate the type I error, given the frequency of laser pulses *f* and feed rate *Fr*, the distance between adjacent pulses is $\delta = \frac{F_r}{f}$. According to equation (4.3), the maximal etched depth $h = \frac{1}{\alpha}\ln\frac{F_{\max}}{F_{th}}$ when *x*=0. Thus the cusp height caused by type I geometric error is

$$\Delta h = h - d(\frac{\delta}{2}) = \frac{1}{\alpha}\ln\frac{F_{\max}}{F_{th}} - \frac{1}{\alpha}(\ln\frac{F_{\max}}{F_{th}} - \frac{\delta^2}{8\sigma^2})$$

(4.6)

Since $\delta = \frac{F_r}{f}$, the type I error is

$$\Delta h = \frac{F_r^2}{8\alpha f^2\sigma^2} \qquad (4.7)$$

When to calculate the type II error, since the distance between adjacent pulses is known, the cusp height is give by the following equation.

$$\Delta h = \frac{\delta^2}{8\alpha\sigma^2} \qquad (4.8)$$

4.4.3 Analysis of Type III geometric errors

4) Source of Type III geometric errors

Compared with type I and II error, analysis and calculation of type III geometric error is more complex. It is determined by not only laser pulse locations but also local geometry of part surfaces. The location of a cavity etched by a laser pulse is defined as L_i (x_{li}, y_{li}, z_{li}) in world coordinate system along with its axis A_i. One cavity location L_1 (x_{l1}, y_{l1}, z_{l1}) etched by laser pulse, which is closest to designed part surface but without damaging part surface,

along with its axis A_1 is shown in Fig.4.10. Due to the three dimensional machining which our lab-built equipment is capable of doing currently, the laser beam is being shooting vertical to *XY* plane of world coordinate system. So the axes of cavity etched by laser pulses on material surfaces are always parallel to the *Z*-axis of world coordinate system and cutting surfaces are parallel to *XY* plane. In this figure, Δd is the distance between two cutting surfaces along *z* direction. Cusp height Δh, the height of undercut material left on the part surface, is the type III geometric error.

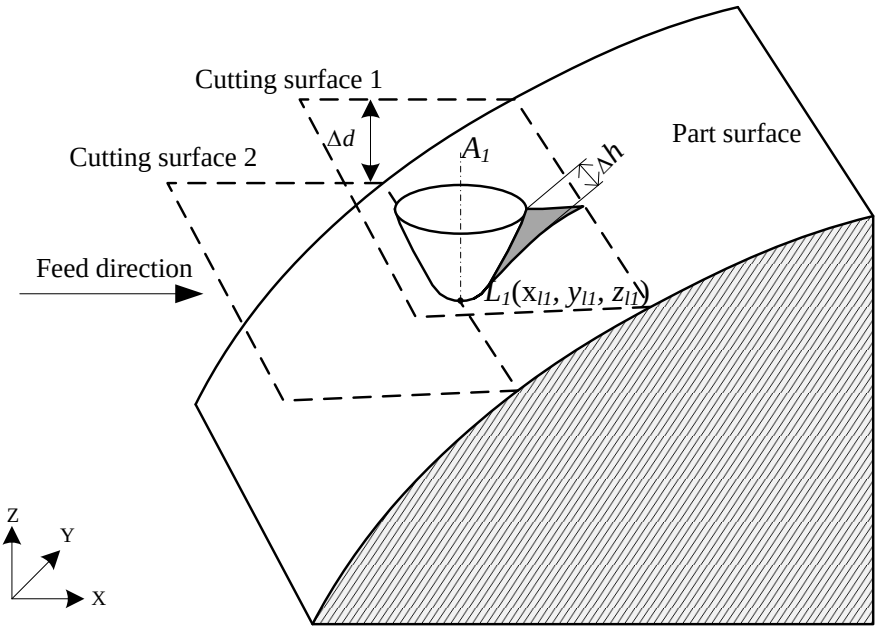

Fig.4.10 Cavity location etched by laser pulse L_1 (x_{l1}, y_{l1}, z_{l1}); Δd is the distance between two cutting surfaces along *z* direction; Δh is the cusp height left on part surface.

5) **Analysis and calculation of Type III geometric errors**

To illustrate how type III geometric errors are calculated, we project the cavity (L_1) etched by laser pulse and cusp left over part surface onto a plane P_0 containing the axis (A_1) of the cavity (L_1) and the feed direction. On this plane, a new local coordinate denoted as X_p and Z_p-axis is defined with the projection of L_1 lying in the origin, axis A_1 of L_1 as the *z* axis and feed direction as the *x*-axis of the coordinate system. The projected cavity, cusp and local coordinate system are present in Fig.4.11. In this diagram, L_{p1} is the projection of L_1; Δh_p is the projection of cusp height Δh; A_1 and Δd keep same as in world coordinate system; C_{p1} (x_{c1}, h) and C_{p2} $(x_{c2}, 0)$ are the intersection points $C_1(x_1, y_1, z_1)$ and $C_2(x_2, y_2, z_3)$ of two adjacent

cutting surfaces and part surface along one cutting path in world coordinate system projected on the plane P_0 where $x_{c1} = \sqrt{(x_{l1} - x_1)^2 + (y_{l1} - y_1)^2}$ and $x_{c2} = \sqrt{(x_{l1} - x_2)^2 + (y_{l1} - y_2)^2}$.

To calculate the Δh_p, we firstly calculate the distance ($\Delta h_p^{\perp}$) from point *M (h, R)* to line $\overline{C_{p1}C_{p2}}$. Then local surface geometric feature from C_{p1} to C_{p2} is considered to calculate $\Delta\varepsilon$. $\Delta h_p = \Delta h_p^{\perp} - \Delta\varepsilon$ is the approximation of Δh.

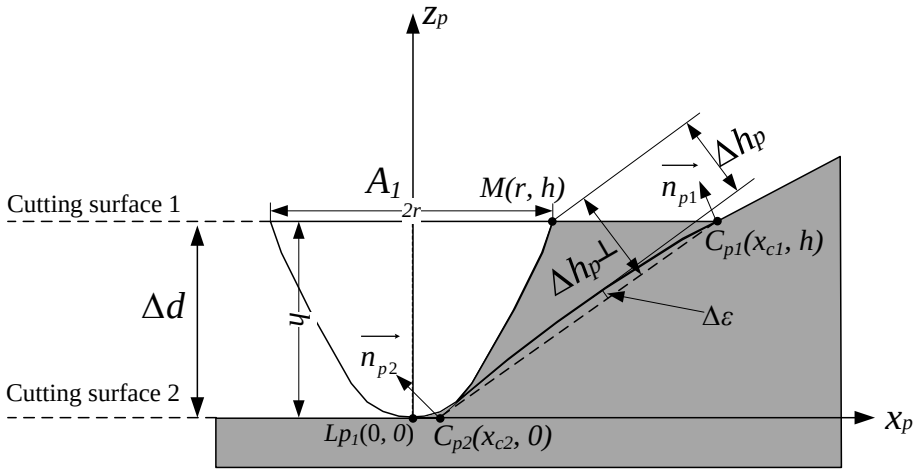

Fig.4.11 Cavity etched by laser pulses and cusp left on part surfaces projected on plane P_0

Line $\overline{C_{p1}C_{p2}}$ can be presented as the following equation:

$$z_p = \frac{h}{x_{c1} - x_{c2}} x_p - \frac{h x_{c2}}{x_{c1} - x_{c2}} \tag{4.9}$$

Thus the distance from point *M* to line $\overline{C_{p1}C_{p2}}$ is

$$\Delta h_p^{\perp} = \frac{(x_{c1} - r)h}{\sqrt{h^2 + (x_{c1} - x_{c2})^2}} \tag{4.10}$$

To consider the local geometric features, we need to look into the surface normal at C_1 and C_2 and its projection on plane P_0. The normal at point C_1 and C_2 in world coordinate system is known as $\vec{n}_1(x_{n1}, y_{n1}, z_{n1})$ and $\vec{n}_2(x_{n2}, y_{n2}, z_{n2})$ respectively. $\vec{n}_z(0,0,1)$ is used to represent a unit vector along *z*-axis of world coordinate system. The normal of plane P_0 can be calculated as $\vec{n}_{p0} = \vec{n}_z \times \vec{C_1C_2}$. Thus the projection of $\vec{n}_1$ and $\vec{n}_2$ on plane P_0 can be

calculated as follows:

$$\overrightarrow{n_{p1}} = \overrightarrow{n_{p0}} \times (\overrightarrow{n_1} \times \overrightarrow{n_{p0}}) \text{ and}$$

$$\overrightarrow{n_{p2}} = \overrightarrow{n_{p0}} \times (\overrightarrow{n_2} \times \overrightarrow{n_{p0}}) .$$

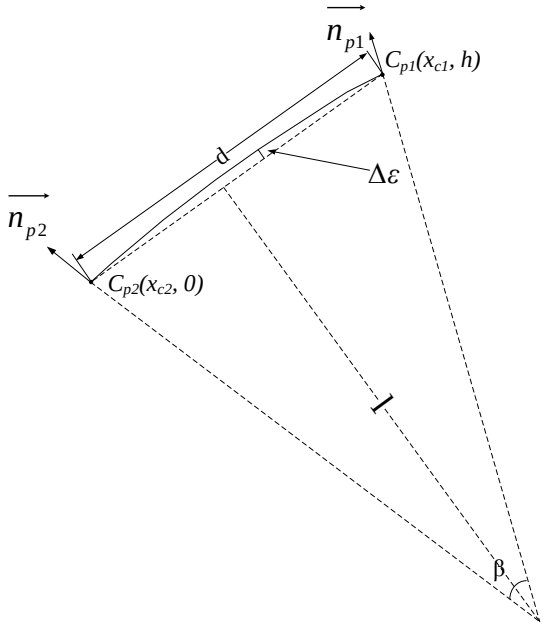

Fig.4.12 Calculation of cusp height considering local geometric *feature*

As shown in Fig.4.12, $\beta = \cos^{-1} \dfrac{\overrightarrow{n_{p1}} \bullet \overrightarrow{n_{p2}}}{\left|\overrightarrow{n_{p1}}\right|\left|\overrightarrow{n_{p2}}\right|} = \cos^{-1} \overrightarrow{n_{p1}} \bullet \overrightarrow{n_{p2}}$. The average curvature of arc $C_{p1}C_{p2}$ can be approximated as $r = \dfrac{d}{2\sin\dfrac{\beta}{2}}$, where $d = \sqrt{(x_{c1} - x_{c2})^2 + h^2}$. l can be approximated as $l = \dfrac{d}{2\tan\dfrac{\beta}{2}}$. Thus,

$$\Delta\varepsilon = r - l = \frac{\sqrt{(x_{c1} - x_{c2})^2 + h^2}}{2\sin\dfrac{\beta}{2}} - \frac{\sqrt{(x_{c1} - x_{c2})^2 + h^2}}{2\tan\dfrac{\beta}{2}} . \qquad (4.11)$$

The cusp height caused by type III geometric error is given by

$$\Delta h_p = \Delta h_p^{\perp} - \Delta\varepsilon = \frac{(x_{c1} - R)h}{\sqrt{h^2 + (x_{c1} - x_{c2})^2}} - \left(\frac{\sqrt{(x_{c1} - x_{c2})^2 + h^2}}{2\sin\frac{\beta}{2}} - \frac{\sqrt{(x_{c1} - x_{c2})^2 + h^2}}{2\tan\frac{\beta}{2}}\right) \qquad (4.12)$$

4.5 Machined Surface Errors Caused by Overlapping Effects in Laser Micromachining

Overlapping effects happen when adjacent laser pulses overlap with each other. The extent of overlapping can be presented as ratio p_o of overlapping portion divided by opening of cavity etched by one laser pulse. When $0 < p_0 < 1$, overlapping has effects on the machined surface errors for laser micromachining. Fig.4.13 (a), (b) and (c) show p_o=0.75, 0.5 and 0.25 respectively.

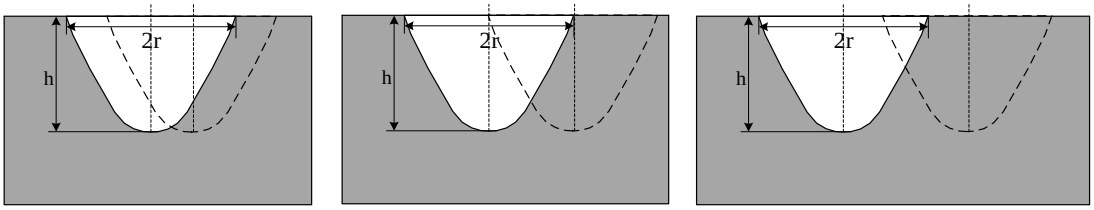

(a) p_o =0.75 *(b) p_o =0.5* *(b) p_o =0.25*

Fig.4.13 Different overlapping ratios (p_o=0.75, 0.5 and 0.25)

4.5.1 Laser beam energy profile along the laser's propagation path

As we discussed before, on focal plane the maximal fluence is achieved. The energy profile of laser beam on focal plane is $F(x) = F_{\max} e^{-\frac{x^2}{2\sigma^2}}$, where $\sigma = R/3$ as shown in Fig.4.14. Beyond the focal plane laser beam propagates diffusively. On each cross section of laser beam beyond the focal plane the energy profile is $F(x) = F_{\max}' e^{-\frac{x^2}{2\sigma'^2}}$, where $\sigma' = R'/3$. R and R' represent the laser beam size on focal plane and cross section plane respectively. γ is the side wall angle of the laser beam along propagation path. d is the distance between the focal plane and cross section. So $R' = R + d\tan\alpha$ and

$\sigma' = (R + d\tan\gamma)/3$. The total energy of laser beam on focal plane and cross section plane are $E = \int_{-\infty}^{\infty} F_{\max} e^{-\frac{x^2}{2\sigma^2}}$ and $E' = \int_{-\infty}^{\infty} F_{\max}' e^{-\frac{x^2}{2\sigma'^2}}$ respectively. If assuming the energy loss is small enough to be neglected in such a short distance, the following relationship will be kept.

$$\int_{-\infty}^{\infty} F_{\max} e^{-\frac{x^2}{2\sigma^2}} = \int_{-\infty}^{\infty} F_{\max}' e^{-\frac{x^2}{2\sigma'^2}}$$

$$\int_{-\infty}^{\infty} F_{\max} e^{-\frac{x^2}{2(\frac{R}{3})^2}} = \int_{-\infty}^{\infty} F_{\max}' e^{-\frac{x^2}{2(\frac{R'}{3})^2}}$$

$$\int_{-\infty}^{\infty} F_{\max} e^{-\frac{9x^2}{2R^2}} = \int_{-\infty}^{\infty} F_{\max}' e^{-\frac{9x^2}{2(R+d\tan\gamma)^2}} \qquad (4.13)$$

Calculating the integral of both sides of equation, we can get

$$\frac{\sqrt{2\pi}R}{3} F_{\max} = \frac{\sqrt{2\pi}(R + d\tan\gamma)}{3} F_{\max}'$$

$$F_{\max}' = \frac{R}{R + d\tan\gamma} F_{\max} \qquad (4.14)$$

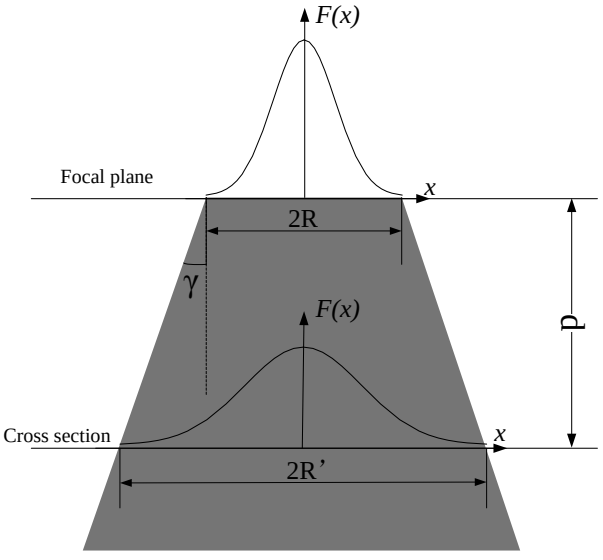

Fig.4.14 Laser energy profile along propagation path

Thus, the energy profile on the cross section of laser beam beyond the focal plane can be written as

$$F(x) = \frac{R}{R + d\tan\gamma} F_{\max} e^{-\frac{9x^2}{2(R+d\tan\gamma)^2}}. \qquad (4.15)$$

Ablation only happens when laser fluence reaches the threshold value (F_{th}) of the material. On the focal plane in Fig.4.15, when $x=x_{th}$, laser fluence reaches threshold value $F(x)= F_{th}$. x_{th} is equal to the radius r of the cavity ablated by laser pulse on focal plane as shown in Fig.4.15. Thus, the threshold value (F_{th}) can be calculated as:

$$F_{th} = F_{\max} e^{-\frac{9r^2}{2R^2}} \qquad (4.16)$$

Same with the focal plane, on the cross section plane of the laser beam beyond the focal plane, when laser fluence reaches F_{th}, ablation will happen. We have

$$F_{\max} e^{-\frac{9r^2}{2R^2}} = \frac{R}{R + d\tan\gamma} F_{\max} e^{-\frac{9x_{th}'^2}{2(R+d\tan\gamma)^2}} \qquad (4.17)$$

Thus the counterpart of x_{th} on the cross section plane beyond the focal plane is

$$x_{th}' = \frac{R + d\tan\gamma}{3} \sqrt{2\ln\frac{R}{R + d\tan\gamma} + \frac{9r^2}{R^2}} \qquad (4.18)$$

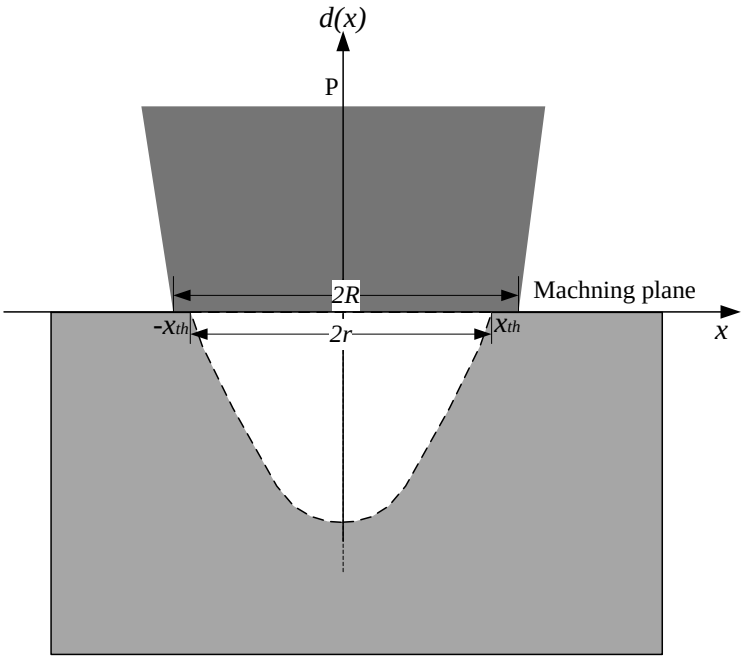

Fig.4.15 Cavity ablated by one single path

4.5.2 Modeling of cutting shape by single laser path

1) Cutting shape by multiple laser pulses per area

Before we discuss the overlapping effects by two adjacent paths, we need to have a good understanding on the ablation behavior by single path. As mentioned earlier, the cutting profile by a single pulse with normally distributed energy can be explained by

$$d(x)=\frac{1}{\alpha}\ln\frac{F_{\max}e^{-\frac{x^2}{2\sigma^2}}}{F_{th}}=\frac{1}{\alpha}(\ln\frac{F_{\max}}{F_{th}}-\frac{x^2}{2\sigma^2}) \quad x\in[-x_{th},x_{th}]. \tag{4.19}$$

This equation can be used when only one single laser pulse shooting on the materials surface. However, in reality due to the limited machining efficiency of laser multiple number of laser pulse per area are needed. As the laser pulses shooting on material, the machined surface will propagate into material. Along with propagation of the machined surface, the energy profile will also change on the partially machined surfaces following the equation (4.15). Therefore, the laser cutting behavior is a combination of multiple laser pulses on partial machined surface in the same area as shown in Fig.4.16

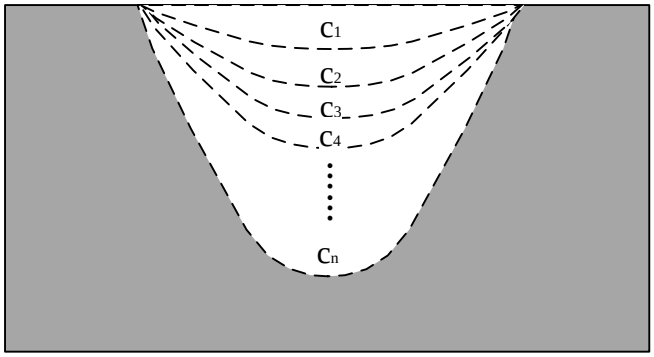

Fig.4.16 Effect of laser ablation by multiple laser pulses per area

In Fig.4.16, C_1 is the surface ablated by the first laser pulse p_1. $C_2, C_3, C_4 \ldots\ldots C_{n-1}$ are the partially machined surfaces after 2^{nd}, 3^{rd}, 4^{th},……*(n-1)th* laser pulse shoot on the material surface. The C_n is final cavity ablation by totally n laser pulses. To understand the behavior of multiple laser pulses, we need to know the local energy fluence of laser pulse shooting on the previous machined surface. As shown in Fig.4.17, C is the partially machined surface. A laser pulse L shoots on C. $p(x_p, d(x_p))$ is a point on the partially machined surface C. S is a horizontal surface containing point p. According to equation (4.15), the energy profile on the surface S is

$$F(x) = \frac{R}{R + d(x_p)\tan\gamma} F_{\max} e^{-\frac{9x^2}{2(R+d(x_P)\tan\gamma)^2}}. \qquad (4.20)$$

So the local laser fluence on point p is

$$F(x_p) = \frac{R}{R + d(x_p)\tan\gamma} F_{\max} e^{-\frac{9x_p^2}{2(R+d(x_P)\tan\gamma)^2}}. \qquad (4.21)$$

If the following condition satisfies

$$x_p \in [-\frac{R + d(x_p)\tan\gamma}{3}\sqrt{2\ln\frac{R}{R + d(x_p)\tan\gamma} + \frac{9r^2}{R^2}}, \frac{R + d(x_p)\tan\gamma}{3}\sqrt{2\ln\frac{R}{R + d(x_p)\tan\gamma} + \frac{9r^2}{R^2}}],$$ the local cutting depth on p by laser pulse L is

$$d(x_p)' = \frac{1}{\alpha}\ln\frac{\frac{R}{R + d(x_p)\tan\gamma} F_{\max} e^{-\frac{9x_p^2}{2(R+d(x_P)\tan\gamma)^2}}}{F_{th}} = \frac{1}{\alpha}(\ln\frac{\frac{R}{R + d(x_p)\tan\gamma} F_{\max}}{F_{th}} - \frac{9x_p^2}{2(R + d(x_P)\tan\gamma)^2}).$$ Thus, in Fig.4.16, the partially machined surface C_1 can be given by

$$d(x)^1 = \frac{1}{\alpha}(\ln\frac{F_{\max}}{F_{th}} - \frac{x^2}{2\sigma^2}) \ . \tag{4.22}$$

Then the partially machined surface C_2 can be represented as

$$d(x)^2 = d(x)^1 + \frac{1}{\alpha}(\ln\frac{\frac{R}{R+d(x)^1\tan\gamma}F_{\max}}{F_{th}} - \frac{9x^2}{2(R+d(x)^1\tan\gamma)^2}) \ . \tag{4.23}$$

The partially machined surface C_3 is

$$d(x)^3 = d(x)^2 + \frac{1}{\alpha}(\ln\frac{\frac{R}{R+d(x)^2\tan\gamma}F_{\max}}{F_{th}} - \frac{9x^2}{2(R+d(x)^2\tan\gamma)^2}) \tag{4.24}$$

Thus the *ith* partially machined surface is

$$d(x)^i = d(x)^{i-1} + \frac{1}{\alpha}(\ln\frac{\frac{R}{R+d(x)^{i-1}\tan\gamma}F_{\max}}{F_{th}} - \frac{9x^2}{2(R+d(x)^{i-1}\tan\gamma)^2}) \tag{4.25}$$

For *n* total laser pluses per area, the final etched cavity is given by

$$d(x)^n = d(x)^{n-1} + \frac{1}{\alpha}(\ln\frac{\frac{R}{R+d(x)^{n-1}\tan\gamma}F_{\max}}{F_{th}} - \frac{9x^2}{2(R+d(x)^{n-1}\tan\gamma)^2}) \tag{4.26}$$

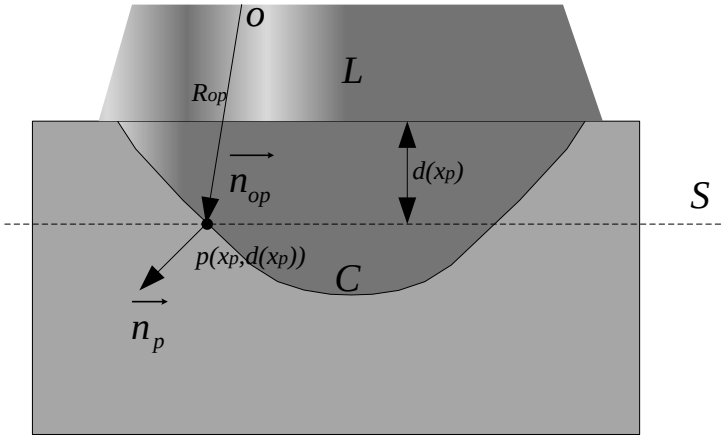

Fig.4.17 Calculation of local cutting energy profile and local cutting depth by multiple laser pulse on partially machines surface

2) Considering incident angle between laser beam and machined material surface in modeling of cutting shape by single laser path

We already discussed the effects by multiple laser pulses per are on cutting performance.

Equation (4.4) has been modified to accommodate the multiple laser pulses. In equation (4.4), another assumption is the laser pulses vertically shoot onto the material surface. For single pulse, the assumption is valid if γ is very small. When multiple laser pulses shoots onto the partially machined surfaces like Fig.4.16, apparently we cannot make this assumption any more. According to [Kahiert 1992 & Patterson 1999], the energy fluence is the total flux due to the incident radiation integrated over the laser pulse. This determines the dependence of the etch rate on the angle of incidence. Still considering Fig.4.17, if R_{op} is the laser ray shooting at point *p*, $\overrightarrow{n_{op}}$, a normalized vector, is used to represent R_{op} from *o* to *p* and $\overrightarrow{n_p}$ is the surface normal at *p* into material. We define *k*, where $k = \overrightarrow{n_{op}} \bullet \overrightarrow{n_p}$. Then the local energy profile on surface *S* is modified as

$$F(x) = \frac{kR}{R + d(x_p)\tan\gamma} F_{\max} e^{-\frac{9x^2}{2(R+d(x_P)\tan\gamma)^2}}. \qquad (4.27)$$

The local cutting depth on point *p* is

$$d(x_p)' = \frac{1}{\alpha}\left(\ln\frac{\frac{kR}{R + d(x_p)\tan\gamma} F_{\max}}{F_{th}} - \frac{9x_p^{\,2}}{2(R + d(x_P)\tan\gamma)^2}\right). \qquad (4.28)$$

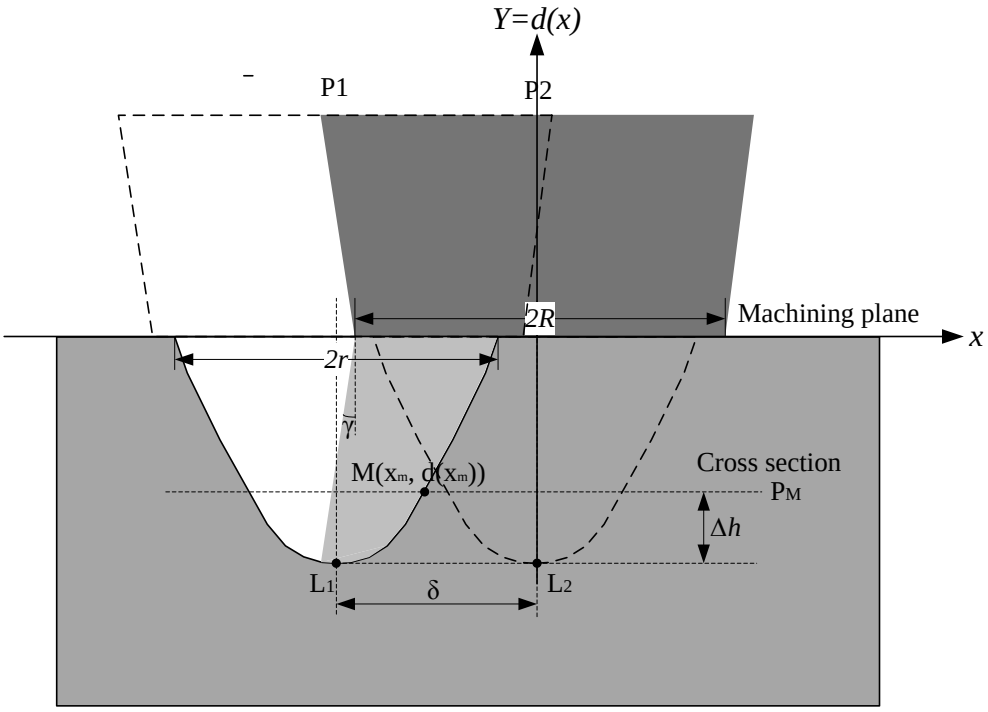

Fig.4.18 Calculation of overlapping effects on surface error

4.5.3 Analysis and calculation of machined surface errors caused by overlapping effects between two adjacent laser pulses

After we understand the behavior by single laser path, now we consider the overlapping effect by two adjacent laser pulses. As shown in Fig.4.18, L_1 is the cavity already ablated by laser pulse P_1. L_2 is the cavity that will be ablated by the adjacent laser pulse P_2. R is the dimension of laser beam on machining plane. r is the dimension of cavity ablated by a single laser pulse. A local coordinate system is defined with the axis of L_2 as the y-axis and x-axis lying on the machining plane. δ is the distance between L_1 and L_2. Thus, based on Equ.4.1, the energy profile on focal plane for P_1 is $F_1(x) = F_{\max} e^{-\frac{9(x+\delta)^2}{2R^2}}$, and based on Equ.4.4 the cutting depth function for L_1 can be represented as:

$$d_1(x) = \frac{1}{\alpha}(\ln\frac{F_{\max}}{F_{th}} - \frac{9(x+\delta)^2}{2R^2}) \quad x \in [-\delta - r, -\delta + r]. \qquad (4.29)$$

The function of the height from the bottom of the cavity to one point on the cavity surface is:

$$\Delta h(x) = \frac{9(x+\delta)^2}{2\alpha R^2} \quad x \in [-\delta - r, -\delta + r]. \tag{4.30}$$

M(x_m, $d_1(x_m)$) is a point on the surface of L_1 where $x_m \in [\delta + r, \delta - r]$. The distance between the cross section plane of laser beam, which contains point *M*, and the focal plane is

$$d_1(x_m) = \frac{1}{\alpha}(\ln\frac{F_{\max}}{F_{th}} - \frac{9(x_m+\delta)^2}{2R^2}). \tag{4.31}$$

The height from point *M* to bottom of L_1 is

$$\Delta h(x) = \frac{9(x_m+\delta)^2}{2\alpha R^2} \ . \tag{4.32}$$

Now we consider the adjacent laser pulse P_2 and its overlapping effects on cavity L_1. The laser profile of P_2 on focal plane is $F_2(x) = F_{\max} e^{-\frac{9x^2}{2R^2}}$, and, on the cross section plane of the laser beam containing point *M*, according to Equ.4.15 the laser energy profile is

$$F_{2m}(x) = \frac{R}{R + d_1(x_m)\tan\gamma} F_{\max} e^{-\frac{9x^2}{2(R+d_1(x_m)\tan\gamma)^2}}. \tag{4.33}$$

On this cross section plane when $x_m \in [-x_{th}', x_{th}']$, the laser fluence is over the threshold value to make laser ablation happen. From Equ.(4.18), we can know

$$x_{th}' = \frac{R + d_1(x_m)\tan\gamma}{3}\sqrt{2\ln\frac{R}{R + d_1(x_m)\tan\gamma} + \frac{9r^2}{R^2}}. \tag{4.34}$$

If $x_m \in [-x_{th}', x_{th}']$ which means

$x_m \in [-\frac{R + d_1(x_m)\tan\gamma}{3}\sqrt{2\ln\frac{R}{R + d_1(x_m)\tan\gamma} + \frac{9r^2}{R^2}}, \frac{R + d_1(x_m)\tan\gamma}{3}\sqrt{2\ln\frac{R}{R + d_1(x_m)\tan\gamma} + \frac{9r^2}{R^2}}]$ (*condition I),*

ablation will happen again at point *M* by laser pulse P_2. Base on equation 4.4, the depth etched by P_2 at point *M* is

$$d_2(x_m) = \frac{1}{\alpha}\left\{\ln\frac{\frac{R}{R + d_1(x_m)\tan\gamma}F_{\max}}{F_{th}} - \frac{9{x_m}^2}{2[R + d_1(x_m)\tan\gamma]^2}\right\}. \tag{4.35}$$

Thus for any point with $x \in [\delta + r, \delta - r]$ on the surface of cavity L_1, considering the

overlapping effects of adjacent laser pulses, height from the bottom of L_1 to the point is

$$\Delta h(x) = \begin{cases} \dfrac{9(x-\delta)^2}{2\alpha R^2} - \dfrac{1}{\alpha}\left\{\ln\dfrac{F_{\max}}{F_{th}} + \ln\dfrac{R}{R+d_1(x)\tan\gamma} - \dfrac{9x^2}{2[R+d_1(x)\tan\gamma]^2}\right\}, & condition\ I\ satisfied \\ \dfrac{9(x-\delta)^2}{2\alpha R^2}, & otherwise \end{cases} . \quad (4.36)$$

After considering the effects of multiple laser pulses per area and the incidental angle of laser beam on material surface, the $\Delta h(x)$ can be calculated for multiple laser pulses per area.

4.5.4 Computer simulation to calculate the machined surface errors

The maximal value of $\Delta h(x)$, $\max(\Delta h(x))$, is the machining by laser micromachining, which considers both the geometric error and the overlapping effects by adjacent laser pulses. The surface roughness is determined by $\max(\Delta h(x))$. Based on different application, different surface roughness will be chosen. Usually we hope to minimize surface roughness as much as possible. Thus $\min(\max(\Delta h(x)))$ is one of the main concerns. No matter in which cases, how to calculate the machined surface errors and how to predict surface roughness given specific laser parameter and functionality requirements are vital in process planning for laser micromachining. A simulation program (*Error Analysis Simulator*) has been developed to calculate the machined surface errors. The procedure for finding the machined surface errors considering the overlapping effects can be described as below:

(1) Input measured parameters of cavity ablated by single laser pulses path including cutting depth *w* and cutting width *d* and the distance between two adjacent laser paths;

(2) Calculate the cutting depth $d_1(x)$ for the points on the cavity L_1 ablated by first laser path P_1;

(3) For every point *M* on the surface of L_1, calculate the energy profile $F_{2m}(x)$ of adjacent laser pulse P_2 on the plane P_m which contains point *M* and is $d_1(x_m)$ below the machining surface;

(4) Calculate the zone $[-x_{th}', x_{th}']$ where the ablation by P2 on the plane Pm happens;

(5) For point *M* which has $x_m \in [-x_{th}', x_{th}']$, calculated the cutting depth $d_2(x_m)$ by P_2 on the plane P_m. So $\Delta h(x) = d - \mathrm{d}_1(\mathrm{x}_\mathrm{m}) - \mathrm{d}_2(\mathrm{x}_\mathrm{m})$.

The flow chart of the algorithm can be seen in Fig.4.19.

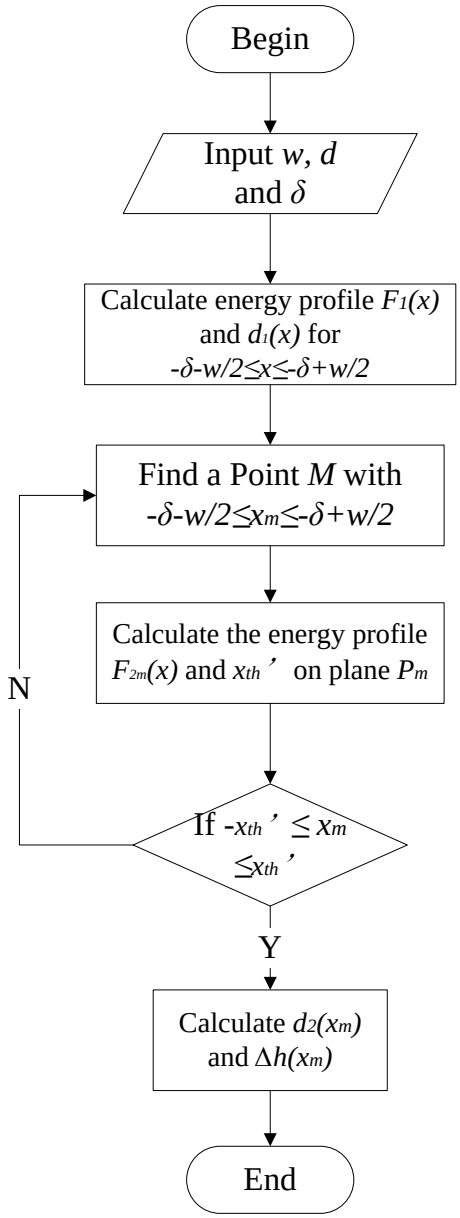

Fig.4.19 Algorithm of calculating the machined surface errors caused by overlapping effects

4.6 Experiments and Preliminary Results

4.6.1 Lab-built excimer laser micromachining system

To study the overlapping effects in laser micromachining and validate our model to calculate machined surface errors, we have done some experiments through our lab-built laser micromachining system. The system can be illustrated in Fig.4.20.

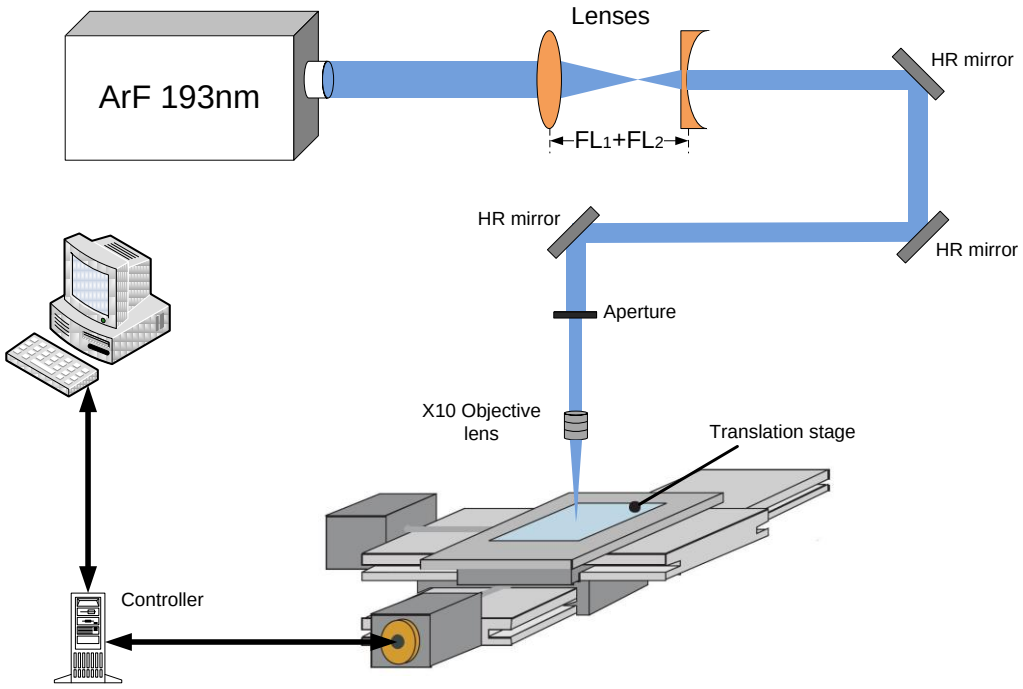

Fig.4.20 Lab-built laser micromachining system

A commercial laser scriber (COMPexPro 201, Coherent, Inc.) is employed in this system. This ArF laser emits laser pulses with wavelength at 193 nm and maximum average power of 4 W. The energy of output laser beam can be adjusted up to 400 mJ and the maximum repetition rate is 10/sec. A lab-built laser delivery system including a set of lens, three high UV reflection mirrors, and objective lens carries the laser beam from the laser scriber to material surface. A CCD camera is installed above the objective lens to monitor the machining process. A 3-aixs translation stage (A3200, Aerotech Inc) is used to provide 3-axis synchronized translation motion for machining parts. High UV reflection mirrors are used to

change the direction laser beam. To reduce the beam size without losing energy, a set of lens consisting of a positive and a negative lens separated by the sum of their focal lengths (FL_2+FL_1) can be put between laser source and machining platform. The output beam diameter reduces proportionally to FL_2/FL_1 and the beam fluence changes with a factor of $(FL_2/FL_1)^2$ correspondingly. An aperture is used to further reduce the laser beam size. However, it also reduces the laser radiance by block part of laser beam. Objective lens focuses laser beam onto material surface to achieve possible highest fluence. The demagnification of objective lens and the size of incoming laser beam determine the laser spot size onto material surface.

The experiments were carried on the surface of high density polyethylene. A series of microchannels were machining on material surfaces. The dimension of the channels was measured via SEM images. The results from experiments and simulations have been compared.

4.6.2 Experiments on the cutting shape by single laser path

The first experiment is to compare the shape of channels from experiments and our simulation model. Several microchannels were made when the number of laser pulses per area is 10, 20, and 40. For each channel, 20 points have been uniformly sampled on its surface. Cutting depth on these 20 points was measured on SEM images and calculated by our simulation program at the same location. The results from both experiments and simulation are listed in Table 4.1, 4.2, and 4.3 for p=10, 20, and 40 respectively along with the difference between experiment and simulation results. In those tables, *d* means the simulation results while *d'* represents the experiment measurement. The SEM images of the cross section of micro channels and the graphs generated via our simulation program are shown in Fig.4.21, 4.22, and 4.23 as well. 20 sample points and their cutting depth are plotted on the diagrams in Fig.4.21 (c), 4.22(c), and 4.23(c). Lines represent the plot of simulation results while dotted lines represent the plot of experiment measurements. From the results and comparison, we can clearly see simulation results and experiments match each other very well. It shows our model can accurately predict cutting performance by single path.

Table 4.1 Experiment measurement and simulation results of cutting shape of single laser path (p = 10)

x(μm)	**-28.39**	**-25.55**	**-22.70**	**-19.87**	**-17.03**	**-14.19**	**-11.35**	**-8.51**	**-5.67**	**-2.83**
d(μm)	0.00	1.76	4.09	6.38	8.48	10.34	11.95	13.26	14.25	14.87
d'(μm)	0.00	1.27	3.53	5.72	8.25	9.98	11.79	13.06	14.15	14.69
Error	0.00	0.39	0.16	0.12	0.03	0.04	0.01	0.02	0.01	0.01
x(μm)	**2.83**	**5.68**	**8.51**	**11.35**	**14.19**	**17.03**	**19.87**	**22.70**	**25.55**	**28.39**
d(μm)	14.87	14.25	13.26	11.95	10.34	8.48	6.38	4.09	1.76	0.00
d'(μm)	14.87	14.33	13.24	11.79	9.83	7.89	6.17	3.47	1.09	0.00
Error	0.00	0.01	0.00	0.01	0.05	0.07	0.03	0.18	0.61	0.00

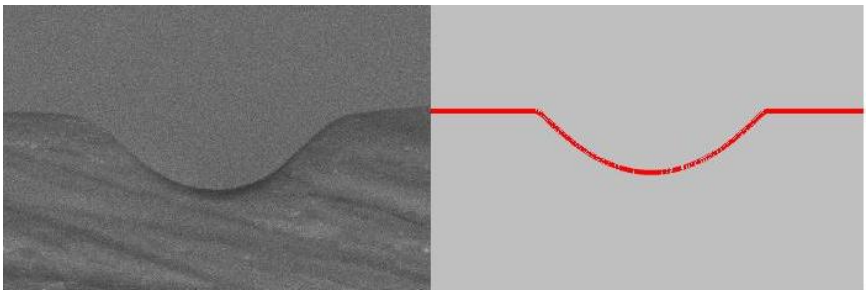

(a) SEM image (b) Simulation result

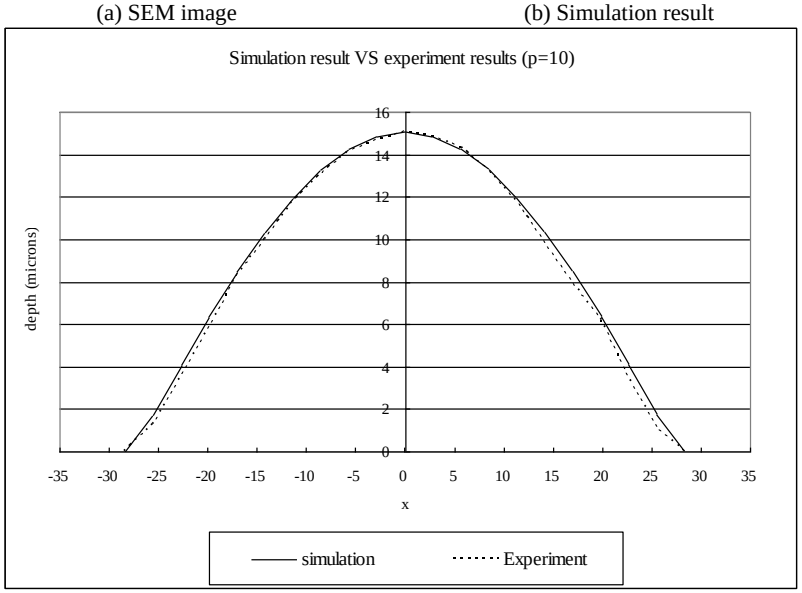

(c)Plot of both experiment and simulation results

Fig.4.21 Comparison of experiment and simulation results (p=10):
(a) SEM experiment image; (b) simulation result; (c) plot of experiment measurement and simulation result

Table 4.2 Experiment measurement and simulation results of cutting shape of single laser path (p = 20)

x(μm)	**-30.84**	**-27.04**	**-24.04**	**-21.04**	**-18.04**	**-15.04**	**-12.04**	**-9.04**	**-6.04**	**-3.04**
d(μm)	0	2.57	5.89	10.35	14.78	19.10	22.90	25.66	27.71	29.03
d'(μm)	0.00	2.18	4.53	9.17	14.75	18.68	23.03	26.12	28.11	29.20
Error	0.00%	17.89%	30.02%	12.87%	0.20%	2.25%	0.56%	1.76%	1.42%	0.58%
x(μm)	**3.04**	**6.04**	**9.04**	**12.04**	**15.04**	**18.04**	**21.04**	**24.04**	**27.04**	**30.87**
d(μm)	29.03	27.71	25.66	22.90	19.65	14.78	11.35	6.47	2.57	0.00
d'(μm)	29.20	28.29	26.30	23.58	19.77	14.15	10.52	4.90	1.81	0.00
Error	0.58%	2.05%	2.43%	2.88%	0.61%	4.45%	7.89%	32.04%	41.99%	0.00%

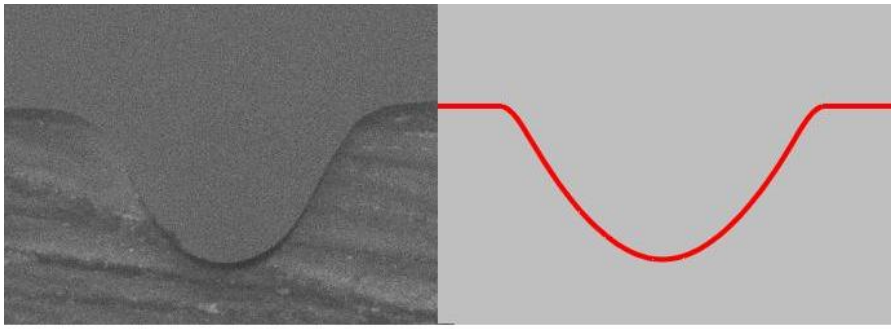

(a) SEM image (b) Simulation result

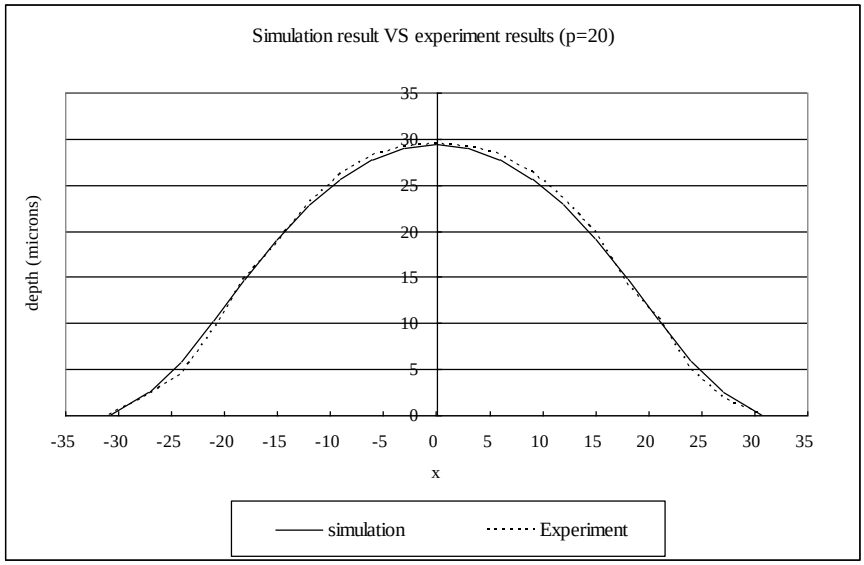

(c)Plot of both experiment and simulation results

Fig.4.22 Comparison of experiment and simulation results (p=20): (a) SEM experiment image; (b) simulation result; (c) plot of experiment measurement and simulation result

Table 4.3 Experiment measurement and simulation results of cutting shape of single laser path (p = 40)

x(μm)	**-29.83**	**-26.83**	**-23.83**	**-20.83**	**-17.83**	**-14.83**	**-11.83**	**-8.83**	**-5.83**	**-2.83**
d(μm)	2.56	8.33	14.67	22.52	30.56	37.77	44.44	48.62	51.16	53.67
d'(μm)	2.18	5.26	11.06	18.86	29.20	37.18	45.70	50.06	52.96	53.89
Error	17.43%	58.37%	32.64%	19.41%	4.66%	1.59%	2.76%	2.88%	3.40%	0.41%
x(μm)	**2.83**	**5.83**	**8.83**	**11.83**	**14.83**	**17.83**	**20.83**	**23.83**	**26.83**	**29.93**
d(μm)	53.67	51.16	48.62	44.44	37.77	30.56	22.52	14.67	8.33	2.56
d'(μm)	53.69	52.42	49.51	44.25	36.27	26.67	18.85	11.78	6.08	1.82
Error	0.04%	2.40%	1.80%	0.43%	4.14%	14.59%	19.47%	24.53%	37.01%	0.00%

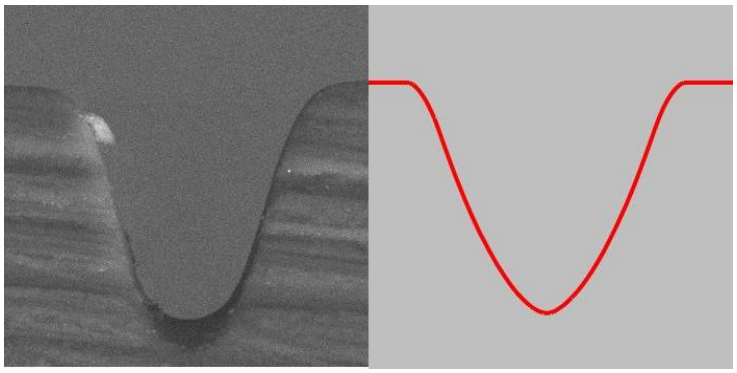

(a) SEM image (b) Simulation result

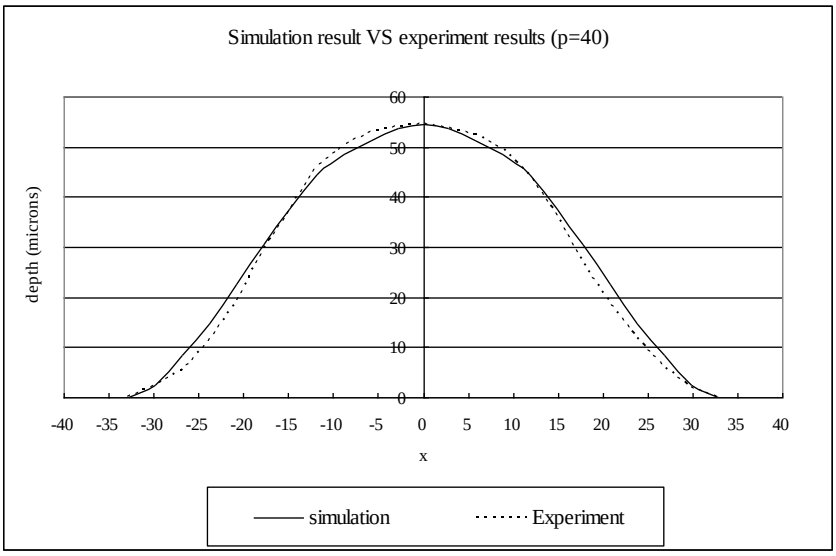

(c)Plot of both experiment and simulation results

Fig.4.23 Comparison of experiment and simulation results (p=40): (a) SEM experiment image; (b) simulation result; (c) plot of experiment measurement and simulation results

4.6.3 Experiments on the machined surface errors

The second experiment is to validate our model to calculate the machined surface errors. In this experiment, two channels are machined side by side. The distance between two channels ranges from 25, 30, 35 to 40 μm. The SEM images and the graphs from simulation are shown in Fig.4.24. The machined surface error in each case from experiment and simulation are listed as $max(\Delta h)$ in Table 4.4 along with the x value where the machined surface errors occur.

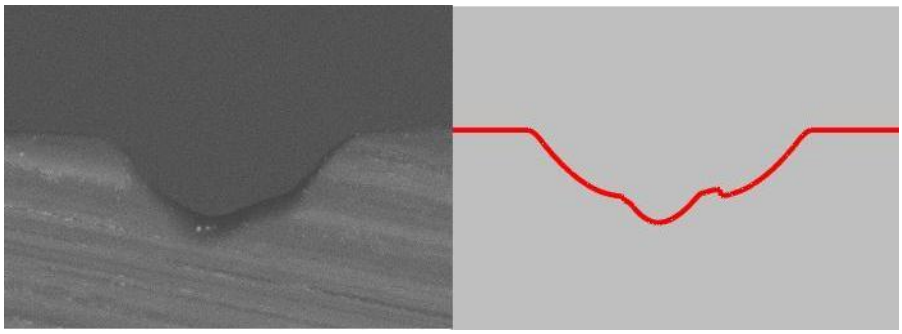

(a) d=25 μm

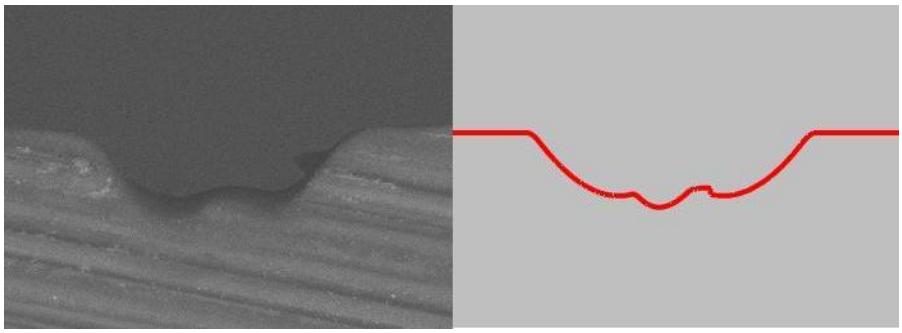

(b) d=30 μm

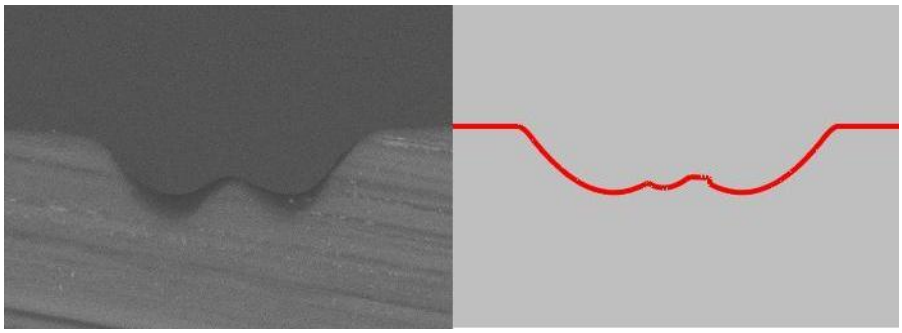

(c) d=35 μm

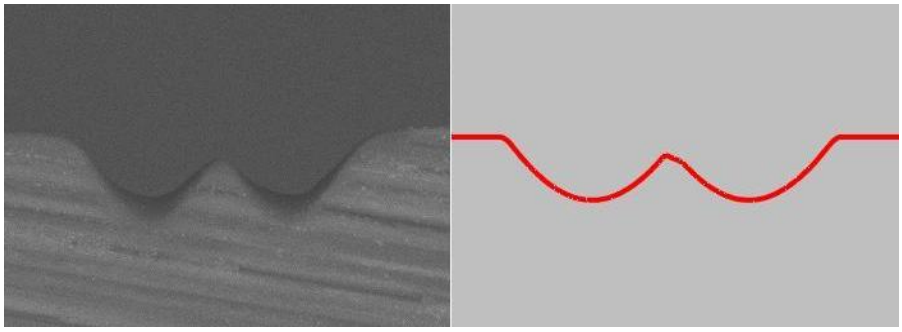

(d) d=40 μm

Fig.4.24 Machined surface error measured in experiment and predicted by our model with different distance (*d*) between two adjacent paths: (a)d=25 μm; (b)d=30 μm; (c)d=35 μm; and (d)d=40 μm;

Table 4.4 Comparison of machined surface error from experiments and simulations

Distance (μm)		25	30	35	40
Simulation	x	9.5	10.5	21.5	21
	max(Δh)	-7.68	-3.7	4.15	9.23
Experiment	x	9.03	10.31	20.64	21.22
	max(Δh)	-7.32	-2.41	3.93	8.89

The experiment result and simulation show good match between each other. It demonstrates our model can calculate and predict machined surface error given limited input parameter including cutting width, depth and number laser pulses per area.

4.7 Summary

Laser micromachining has been exploited in many areas due to its contactless characteristics, extensive material selections and micro scale machining capability. Integrating CAD/CAM into laser micromachining shows great potentials for applications that need complex geometric features. However, machined surface errors in micromachining have not been studied systematically.

In this chapter, the machined surface errors in laser micromachining have been analyzed. Unlike traditional machining, geometric error solely cannot explain the machined surface errors in laser micromachining by itself. The overlapping effects, which are caused by two adjacent laser pulses, were studied. A model to calculate and predict machining considering both geometric error and overlapping effect has been proposed based on the mechanism of laser ablation and energy profile of laser beam. Via this model, machined surface errors can be calculated given the input including cutting width, depth and distance between two adjacent laser pulses. Also, give a specific tolerance an optimal parameter can be generated for the purpose of process planning. Experiment results and simulation results have been compared. It showed good match between our model and experiment measurement.

CHAPTER 5

AN INTEGRATED BIOMANUFACTURING SYSTEM FOR DESIGN AND MANUFACTURING OF BIOMEDICAL DEVICES

Laser micromachining is a good candidate for manufacturing of biomedical devices in micro scale. We have presented the techniques for laser micromachining and machined surface error analysis in laser micromachining. In biomanufacturing, fabricated structures with desirable geometric features cannot solely perform biomedical functions. Biological species like cells, proteins and bacteria need to get involved to make biomedical devices functional. In this chapter, we will propose an integrated biomanufacturing system to utilize both laser micromachining and biological species for design and manufacturing of biomedical devices.

5.1 The Roles of Living Cells in Biomanufacturing

In conventional manufacturing processes, mechanical parts with desirable geometric features or assembly can perform full functionality, in some cases, with assistance of some forms of energy, while biomanufacturing utilizes living cells to perform biomedical functionality. Fabricated structures have to be integrated with living cells to realize the full functions of biomedical devices.

For example, proteins can facilitate growth and adherence of some cells. Engineered cellular networks with protein adsorbed on the surface can be used as biointerfaces to guide the growth and adherence of cells and provide nutrition for cells. Another example is magnetotactic bacteria (MTB) which are a class of bacteria exhibiting the peculiar ability to orient themselves along the magnetic field lines of earth's magnetic field. MTB produce and

contain magnetosomes, which are nanometer-sized, magnetic, mineral crystals enclosed in a membrane. The magnetosomes produced during the growth of MTB has very interesting applications. MTB have been used in the study on the diagnostic devices and microsensors [McMurray 2007 & Denomme 2007].

With these living cells and microstructures fabricated by laser micromachining, we can achieve tremendous biomedical functionality with biomedical devices. So a biomanufacturing system based on laser micromachining integrated with living species is feasible, meaningful and promising.

5.2 An Integrated Biomanufacturing System for Micro Medical Devices Based on Laser Micromachining

As discussed in 5.1, manufacturing techniques and biological species are two vital components in biomanufacturing. An integrated biomanufacturing system will involve both of them.

Based on the machining parameter development and machined surface error analysis we have done, microstructures can be fabricated by laser micromachining following designed patterns. Different surface finishing can be achieved based on our machined surface error analysis to provide insight into the effects of surface quality on biological activities.

Proteins, bacteria and other living cells can be deposit into fabricated microstructures using micropipette or other advanced techniques such as material printers. Then the living cells will perform some specific biomedical functions as biointerfaces, cellular networks, delivery devices, biosensors or biocarriers. This is the motivation we propose an integrated biomanufacturing system based on laser micromachining and biomedical techniques.

As shown in Fig.5.1, this system consists of 4 modules: parameter design and fabrication module, surface analysis module, biological deposit module, and biological species growth module.

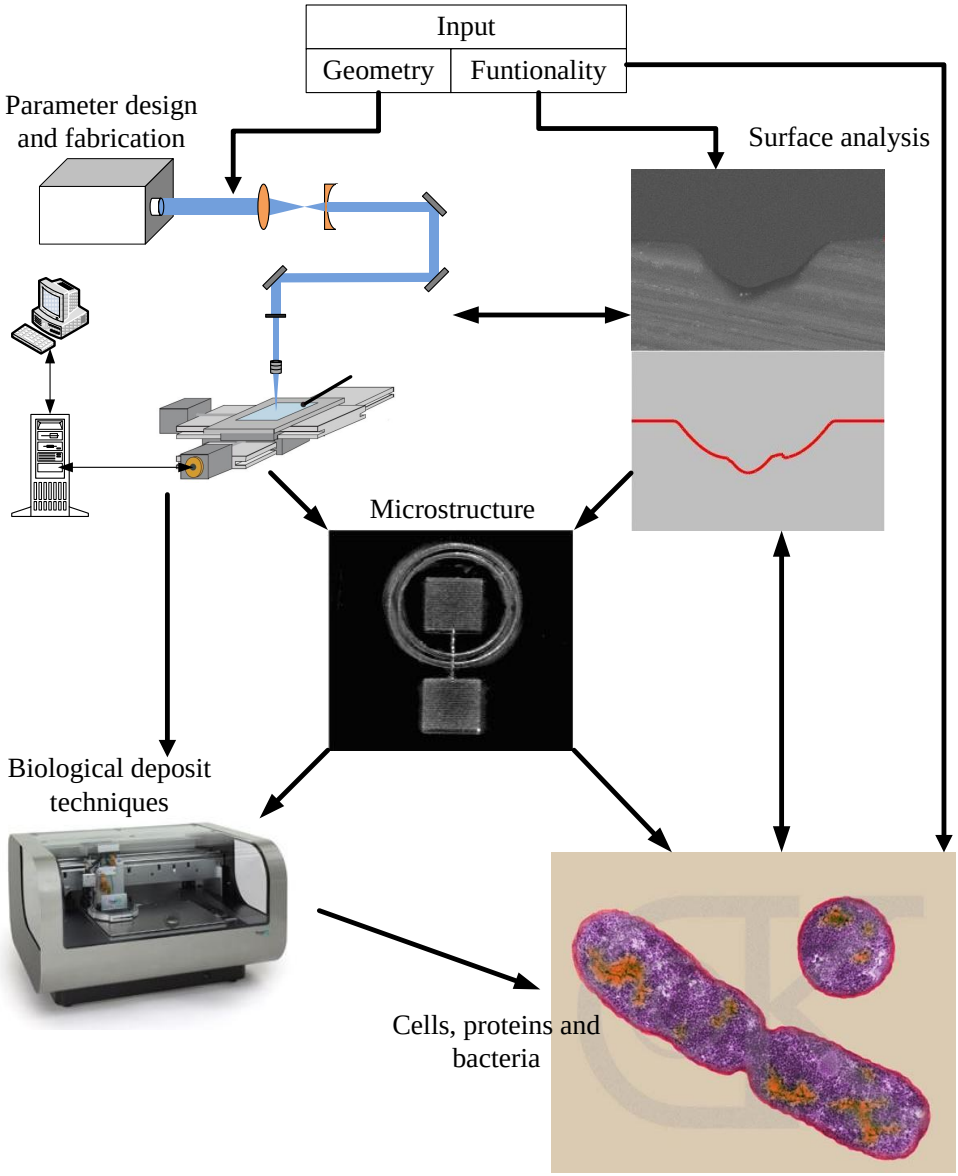

Fig.5.1 Overview of biomanufacturing system for micro medical devices based on laser micromachining

In this system, the input includes two aspects: geometry, which defines the patterns of microstructures, and functionality, which defines the function of the biomedical devices. Parameter design and fabrication module produce the microstructure based on the input geometry. Our machining parameter development can be used as the basis to select the laser parameters to achieve desired machining parameters. According to input geometry and functionality, surface analysis determines the surface roughness and corresponding

machining parameters. Parameter design module and surface analysis module work closely to select suitable laser parameters and produce desired microstructures. Taking microstructures as the input, biological deposit techniques are involved to deposit the living cells along with their medium into microstructures. Then the growth of biological species will be observed, manipulated and controlled to realize the functionality of the medical devices.

5.3 Functionality of the Integrated Biomanufacturing System

5.3.1 Machining parameter design and fabrication

This module is to select the laser parameters including laser energy, number of laser pulses per area, laser beam size and machining surfaces based on the input geometry of microstructure. Our work in chapter 3 shows a method to develop machining parameters for laser micromachining. Then microstructures can be fabricated by our excimer laser micromachining system.

5.3.2 Surface analysis

This module is to determine the surface roughness based on the geometry and functionality inputs. Then it works closely with parameter design and fabrication module to produce microstructures. This module can assist the process planning for laser micromachining.

5.3.3 Biological deposit module

In this part, living cells with their cultivation medium will be deposited into microstructures using micropipette or some other advanced techniques. Dimatix material printer can be utilized to inject biological species into the fabricated microstructures. The mechanism of the injection can be seen in Fig.5.2. The cells and their living medium are dropped via nozzle into the microstructure made through laser micromachining. The nozzle can be moved manually or in a predefined pattern.

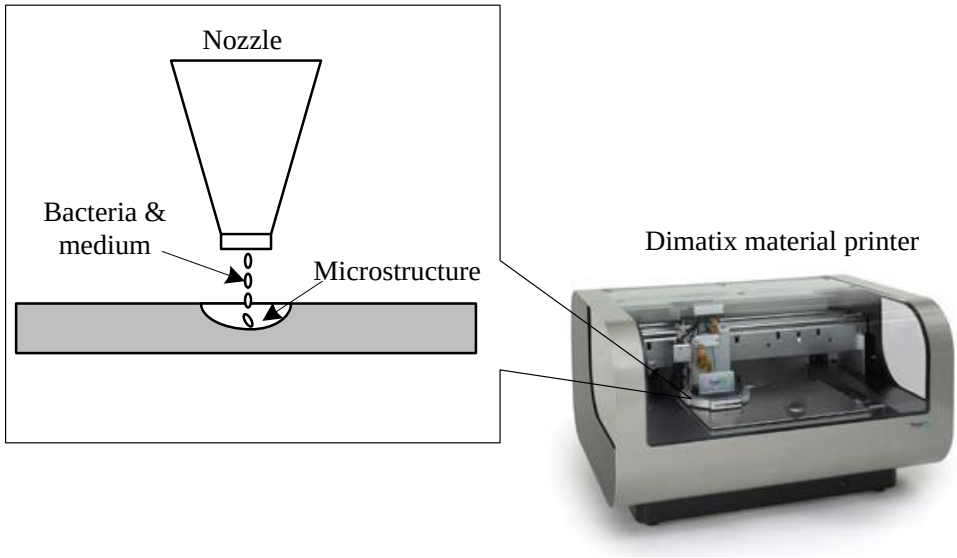

Fig.5.2 Bacteria and medium injected into microstructure by Dimatix material printer

5.3.4 Bacteria growth in microstructures

In this module the living cells will grow in microstructures. Biological activities of these living cells can be observed, manipulated and controlled to realize specific biomedical functions such as biointerfaces, biosensors, biocarriers or cellular networks.

5.4 Summary

In this chapter, we proposed an integrated biomanufacturing system based on laser micromachining and living biological species. The overall description of the system and the functionality of each module in this system were discussed. The machining parameter design and machined surface error analysis have been presented in Chapter 3 and Chapter 4. The design and fabrication of biomedical devices and biological study on machined material surfaces will be discussed in the following chapters. In Chapter 6, a medical device fabricated by laser micromachining to guide protein adsorption and adherence will be discussed. It can be used as biointerfaces and delivery devices. Electrical properties are always used to be as indicators of biological activities. Design and manufacturing of medical

devices to characterize the electrical parameter of biological species will be introduced in Chapter 7. The electrical properties of magnetotactic bacteria will be studied using this device.

CHAPTER 6

STUDY OF BOVINE SERUM ALBUMIN ADSORPTION ON LASER MICROMACHINED SURFACES FOR MANUFACTURING OF BIOMEDICAL DEVICES

As stated in the previous sections, the laser micromachined polymeric materials are good candidates for biomedical applications especially in manufacturing of biomedical devices. However, the biocompatibility of materials for specific applications has yet been discussed. In the section, the study of adsorption of albumin will be carried out on laser micromachined surfaces of polyethylene and PDMS materials. The interaction between the laser micro-machined surfaces of these two matrerials and bovine serum albumin (BSA) in 0.9% NaCl solution (2mg/mL) containing sodium azide will be studied by X-ray (EDS) on Scanning Electron Microscope (SEM). The adsorption of Fluorescent isothiocyanate (FITC) Conjugate bovine serum albumin will be also investigated with the fluorescent images captures by UV biological microscope. With the capability of fabricating microstructures by laser micromachining and the ability of adsorption of albumin on the laser mciromachined surface, biomedical devices can be fabricated to guide the adherence of protein to be used as biointerfaces and protein delivery tools.

6.1 Introduction

Polymeric materials play an important role in research and development of biomedical devices. For example, biosensor is one attractive application for polymeric materials in biomedical areas. Using polymers as the base materials of biosensor has recently received lots of attentions [Lucci 2003]. There are quite some studies regarding to the manufacturing of biosensor using polymers [Griffith 1996; Gerard 2002]. For example, polymers were used

in amperometric biosensor in [Emr 2005]. While biocompatibility, particularly blood compatibility, is the most important property required for these materials [Tsuruta 1993]. Investigation and improvement of biocompatibility of polymers is of great importance in the manufacturing of biomedical devices.

Polyethylene is one of the most widely used polymeric materials, consisting of long chains of the monomer ethylene. The ethylene molecule (C_2H_4) has two CH_2 groups connected by a double bond. One ethylene molecule can be represented as Fig.6.1(a) and polyethylene consisting of repeating ethylene units is shown in Fig.6.1(b). Thus, polyethylene only contains the chemical elements carbon and hydrogen. Polyethylene and its derivatives have abroad applications in biomedical areas. Suitable biologically active agents including microbial peptide agents, detergents, non-steroidal anti-inflammatory drugs, cations, amine-containing organosilicones, diphosphonates, fatty acids, fatty acid salts, heparin and glucocorticosteroids may attached on polyethylene, which may be used as a medical unit of an implantable devices like pacemaker [Yang 2002]. Due to its excellent biocompatibility, high impact strength, remarkable wear resistance and low friction coefficient, Ultra-high molecular weight polyethylene (UHMWPE) is widely used in orthopedics, especially in the fabrication of articular components for arthroplasties, in particular, the acetabular cup or liner in a total hip joint replacement (THJR) and the tibial insert in a total knee joint replacement (TKJR) [Park 2004]. Therefore, study of biocompatibility of polyethylene is worthwhile and meaningful.

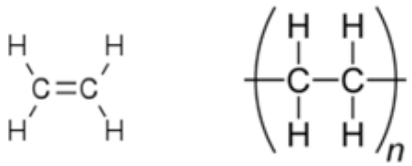

(a) (b)

Fig.6.1 (a) Single ethylene molecule; (b) polyethylene consisting of repeating ethylene units.

Polydimethylsiloxane (PDMS) belongs to a group of silicones which are polymeric organosilicon compounds. It is a popular material for contact lenses and medical devices. The chemical formula for PDMS is $(H_3C)_3SiO[Si(CH_3)_2O]_nSi(CH_3)_3$ and density is 0.965 g/cm−3. PDMS is one of the most common materials used for flow delivery in microfluidics chips for Bio-MEMS.

Proteins may play an important role in the interaction of the biomedical device and surrounding environment. Thus, lots of fundamental research work studied the adsorption behaviors of proteins onto different polymeric supports. Generally the adsorption of protein is a rapid and irreversible process. Hydrophobic and electrostatic interactions are dominated factors in adsorption process [Duracher 2004]. Serum albumin is the most abundant plasma protein in humans and other mammals. It is essential to maintain the osmotic pressure for proper distribution of body fluid between intravascular compartments and body tissues. Bovine serum albumin (BSA) is used in this study. BSA is commonly used in biomedical research especially in immunodiagnostic procedures, clinical chemistry reagents, cell culture media, protein chemistry research and molecular biology laboratories. The adsorption of BSA on Ti surface was observed for its effect on osteoblast attachment in [Yang 2002]. The maximum adsorption was achieved after 180 minutes of incubation. In [Wei 2009], the influence of surface wettability on albumin adsorption was studied on polymers. The adsorption of BSA as a function of pH, ionic strength and temperature was investigated on latex particles in [Duracher 2007].

In this chapter, the adsorption of BSA on laser micromachined surfaces of polyethylene and PDMS will be studied to explore the possibility of using laser micromachining, polyethylene and PDMS in manufacturing of biomedical devices. The interaction of BSA and laser micromachined surfaces will be analyzed X-ray (EDS) on Scanning Electron Microscope (SEM), which yield the chemical information on the surfaces of material, and confirmed by fluorescent BSA observed under UV microscope. In the remaining parts of this chapter, the sample preparation and experiment procedure will be introduced along with different methods to measure the adsorption of BSA on material surfaces. The results from EDS study and fluorescent analysis will be recorded and discussed. Then two types of

biomedical devices utilizing the capability of laser micromachining to fabricate microstructures and ability of adsorption of protein on laser micromachiend surfaces will be presented.

6.2 Materials and Experiments

6.2.1 Sample preparations

The polyethylene sheets and PDMS are purchase from Goodfollow Inc. Polyethylene sheets are in dimension of 150x150 x10mm with density of 0.95 g/cm^3. PDMS sheets are in 300x300x3mm. The whole sheets were cut to small pieces. On each piece of polyethylene and PDMS sheet, an array of 3x3 mm reservoirs was fabricated in our lab-built excimer laser micromachining system. The laser energy was set to 100 mJ, the aperture size was set to 4, and the number pulses per area is 6 for polyethylene and 10 for PDMS. According our machining parameters study, the depth of these reservoirs is 30μm approximately. After laser micromachining, substrates were cleaned with methanol and de-ion water. When samples are incubated in BSA solution, the interaction of protein and laser micromachined surface will occur in reservoirs (as shown in Fig.6.2) which are the interesting areas we will be analyzing.

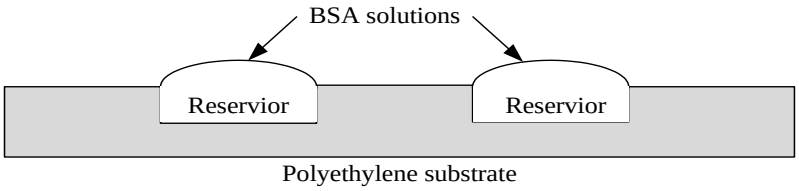

Fig.6.2 BSA solution on the laser micromachined polyethylene and PDMS surfaces

6.2.2 Albumin adsorption experiments

50 mL Standard bovine serum albumin solution with concentration of 2mg/mL was purchased from Fisher Scientific, which contains bovine albumin fraction V in NaCl solution containing sodium azide. Fluorescent isothiocyanate (FITC) Conjugate bovine serum albumin powders were obtained from SIMAG-ALDRICH. Fluorescent BSA solution was

prepared by dissolving fluorescent BSA powder in PBS with the same concentration of standard BSA solution purchased (2mg/mL).

Laser micromachined polyethylene and PDMS substrates were incubated in standard BSA solution and fluorescent BSA/PBS solutions respectively. Incubation ranged from 1, 3, 6, 12 to 24 hours. The incubator was set to 37^{o}C and 5% concentration of CO_2.

6.2.3 Fluorescent study and EDS analysis on Scanning Electron Microscope

Many methods and equipments have been used to measure the adsorption of albumin by substrate materials. Generally there are two strategies for measurement purposes: indirect methods and direct methods. Indirect methods usually measure the concentration of the albumin solution before and after experiment and calculate the difference. In [Yang 2003], Protein concentrations were analyzed using the micro BCA protein assay. Same method was also adopted in [Ishihara 1999]. Direct methods will analyze the surface after the adsorption of protein occurs. QCM-D was used in [Wei 2009] to measure the mass adsorption of protein at the surface by monitoring the resonance behavior of piezoelectric oscillation. X-ray photoelectron spectroscopy (XPS) analysis and ATR-FTIR measurements are widely used methods to measure the adsorption of protein on materials surfaces [Zhou 2005; Lucci 2003; Griffith 1996, 1997]. In this work X-ray analysis (EDS) on scanning electron microscope was used to measure albumin adsorption. Energy dispersive X-ray spectroscopy (EDS) is an analytical technique used for the elemental analysis or chemical characterization of samples. Bovine serum albumin will introduce nitrogen element on the materials surfaces. Since substrate materials polyethylene and PDMS contain no nitrogen, the introduced nitrogen can be used as an indicator of adsorption of protein. Before each analysis, a simulation procedure was run to determine the penetration of X-ray into analyzed material with the given information of chemical formula and density of substrate materials.

For fluorescent BSA solution, the fluorescent images were observed under TC5000 Series Inverted Biological Microscope from Meiji Techno equipped with INFINITY CCD digital camera 2 from Lumenera Corporation. Images were analyzed by INFINITY ANALYZE 6.0. The pristine BSA solution on the material surfaces was observed. Then after incubation, the

laser micromachined surfaces interacted with albumin were also studied.

6.3 Results

6.3.1 Fluorescent analysis of interactions of BSA and laser micromachined polyethylene surfaces

Fig.6. 3 (a) and (b) show the pristine BSA on the laser micromachined surfaces. The green color represents the fluorescent BSA on the material surfaces. Dark areas are the substrate material surfaces.

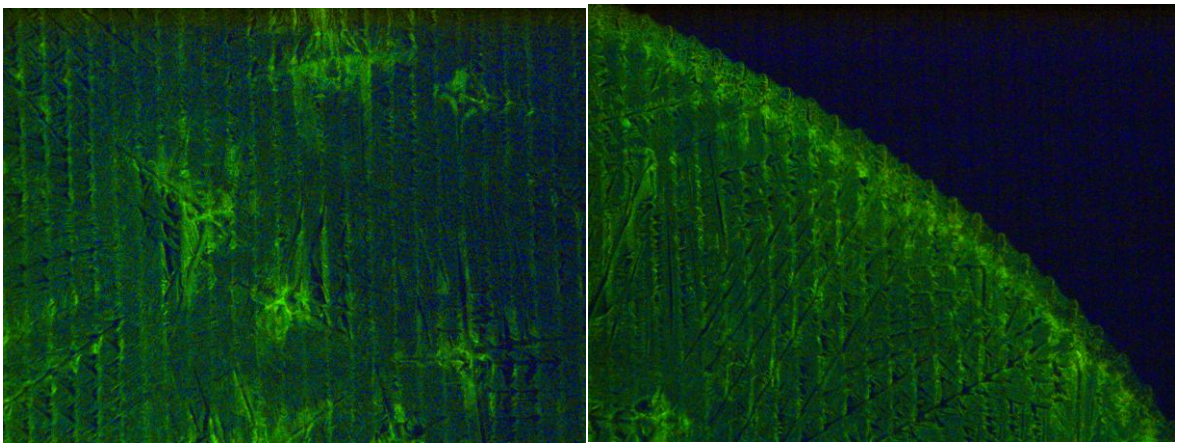

(a) (b)

Fig.6.3 Pristine fluorescent BSA on laser micromachined polyethylene surfaces

Fig.6.4 and Fig.6.5 show the protein adsorption on the laser micromachined polyethylene surfaces after one hour and six hours incubation. Images are captured on randomly picked four spots on the laser micromachined surfaces by INFINITY digital camera 2. From these fluorescent images, the adsorption of albumin on laser micromachined polyethylene can be confirmed and the adsorption is time-dependent since the amount of albumin and the area that adsorbed protein are larger in Fig.6.5 than in Fig.6.4. Also from Fig.6.4 we can see that protein adsorbed were dispersed as dots on the surfaces, while in Fig.6. 5 as the incubation time period increased protein cells began to aggregate and clog. Although we can use some image analysis software to estimate the protein adsorbed on laser micromachined surface,

more accurate analysis will rely on EDS study on those surfaces due to the limited areas where image were captured and lack of accuracy in image processing only counting the illumination.

A free image processing software JMicroVision was used to analyze the machined surface area that adsorbed protein. Proper threshold values were set for each image. Then the percentage of fluorescent color was calculated for each image. Average percentage values and standard deviations are shown in Table 6.1.

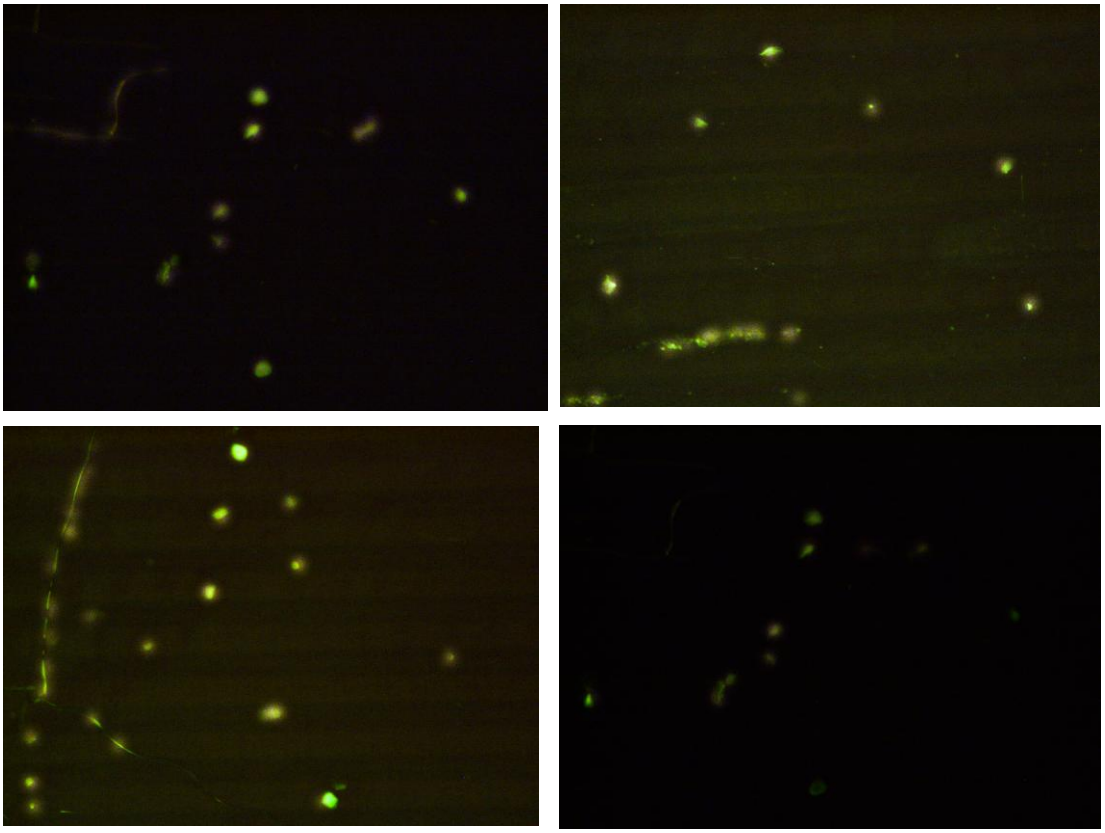

Fig.6.4 Albumin adsorption on laser micromachined polyethylene surfaces after one hour incubation

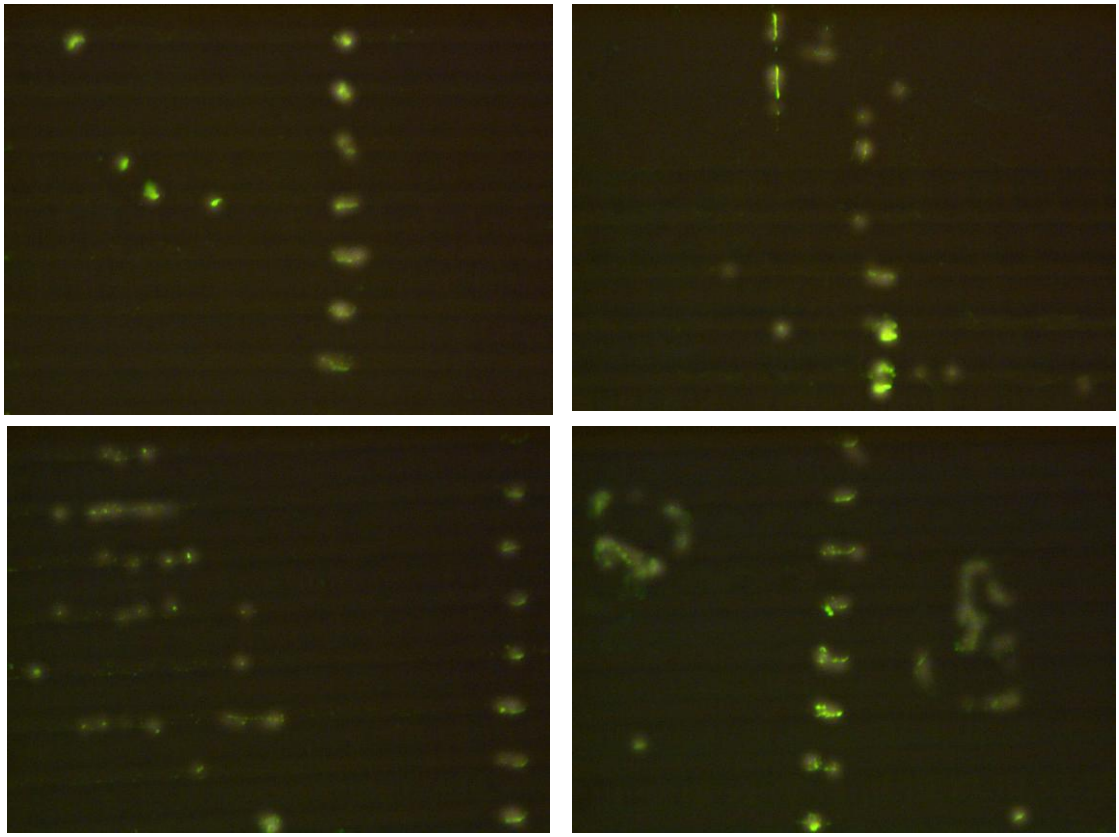

Fig.6.5 Albumin adsorption on laser micromachined polyethylene surfaces after six hours incubation

Table 6.1 Percentage of protein on laser micromachined surfaces for different incubation time

Incubation time(hours)	Percentage of areas adsorbed protein	
	Average	Standard deviation
1	0.27%	0.05%
6	1.26%	0.31%

6.3.2 Fluorescent analysis of interactions of BSA and laser micromachined PDMS surfaces

In Fig.6.6, the fluorescent images of albumin adsorption on laser micromachined PDMS surfaces were presented. 1, 3, 6, 12 and 24 hours incubation time were adopted. As shown in these images, with incubation increased time more protein was adsorbed by laser

micromachiend PDMS surfaces. Fig.6.7 shows the trend of protein adsorption on the laser micromachined surfaces as the incubation time increased.

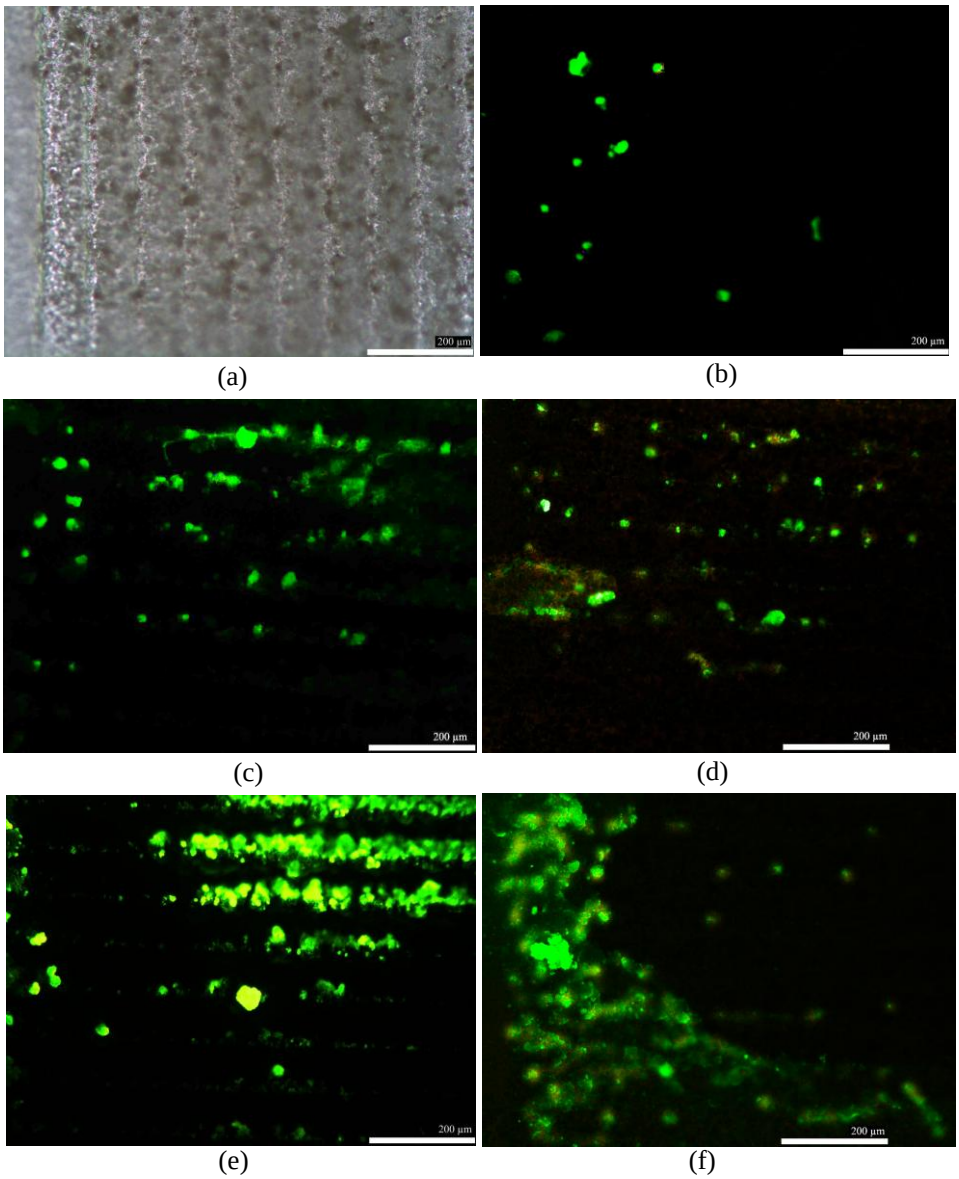

(a) (b)

(c) (d)

(e) (f)

Fig.6.6 Fluorescent image of albumin adsorption on laser micromachined PDMS surfaces with difference incubation time of 1(b), 3(c), 6(d), 12(e) and 24(f) hours

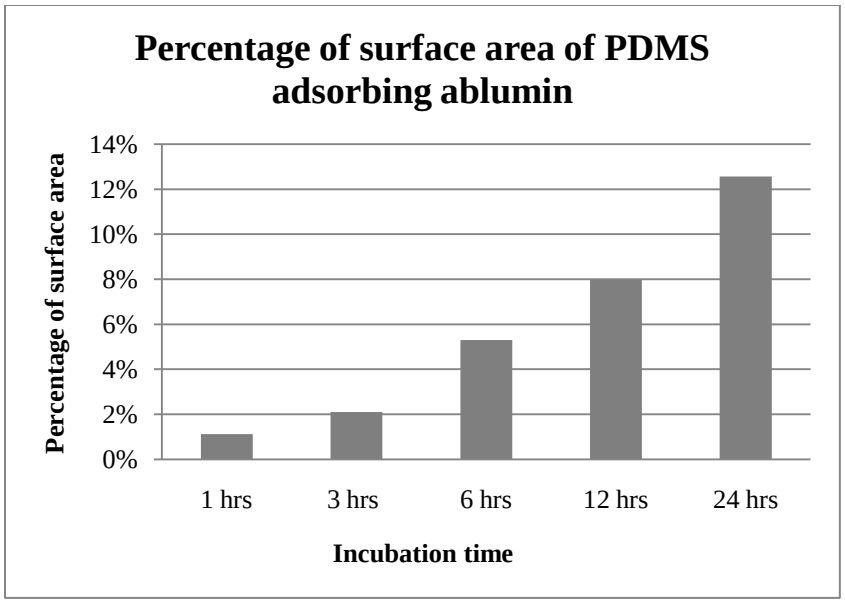

Fig.6.7 Adsorption of albumin on the laser micromachined PDMS surfaces with incubation time increased

6.3.3 EDS on SEM analysis of albumin adsorption on laser micromachined polyethylene surfaces

Before using EDS to analyze the surfaces of substrates, Electron Flight Simulations (EFS) were run to determine the penetration of X-ray into materials. The chemical formula of polyethylene is $(CH_2)_n$ and density is 0.96. 5.0 kV voltage was selected after several iterations of simulations with 0.85 μm penetration into material surfaces achieved. The simulation result is shown in Fig.6.8 for polyethylene.

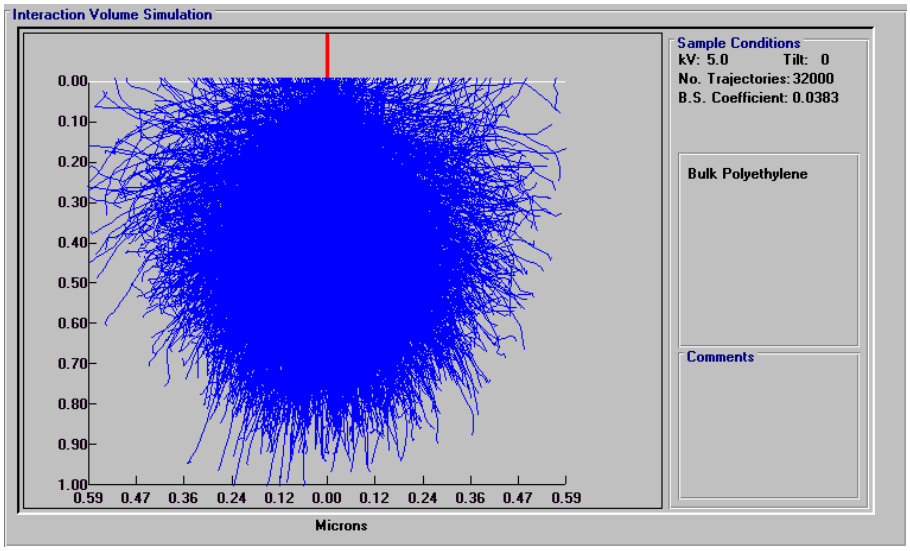

Fig.6.8 Electron Flight Simulation result on polyethylene surfaces

In Fig.6.9, the weight percentage of nitrogen on the laser micromachined polyethylene surfaces was shown with increasing incubation time. The percentage of nitrogen on the surfaces ranged from 1.32% to 1.65% when the incubation time is 1, 3, 6, 12 and 24 hours.

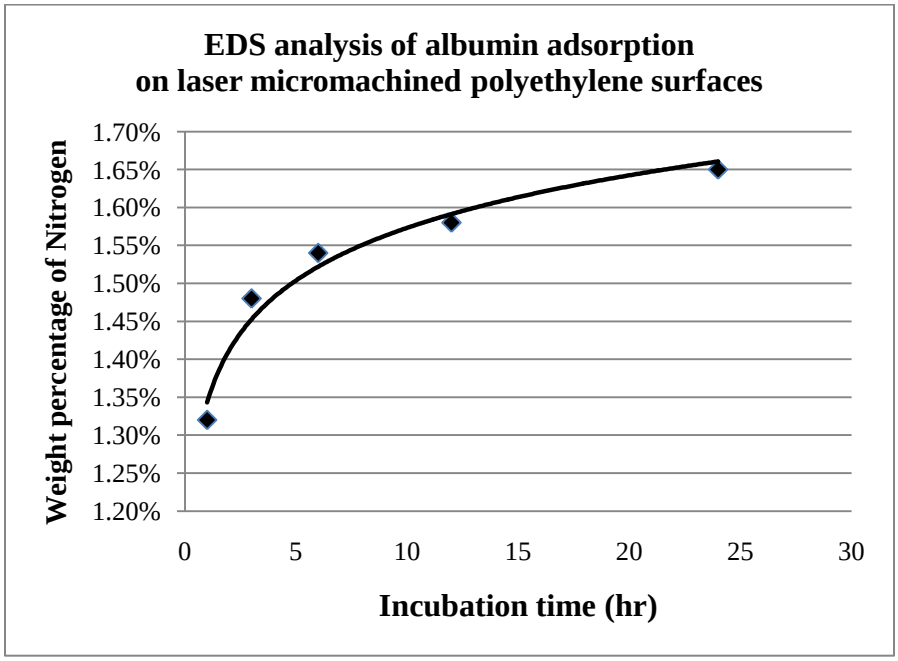

Fig.6.9 Percentage of Nitrogen on the laser micromachined polyethylene surfaces with increasing incubation time

6.3.4 EDS on SEM analysis of albumin adsorption on laser micromachined PDMS surfaces

Same EFS procedure was also performed on the laser micromachined PDMS surfaces. Fig.6.10 shows the weight percentage of nitrogen on the laser micromachined PDMS surfaces with different time of incubation.

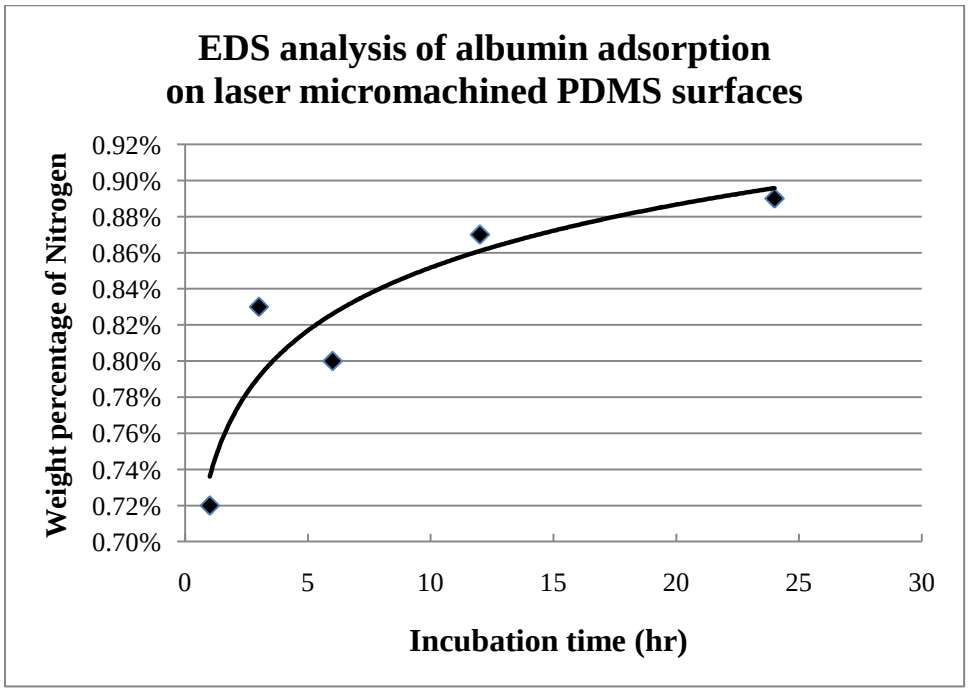

Fig.6.10 Percentage of Nitrogen on the laser micromachined PDMS surfaces with increasing incubation time

6.4 Conclusions and Discussion

As discussed in previous sections, the laser micromachined polyethylene and PDMS surfaces showed the ability of adsorption of albumin protein. The fluorescent images and EDS analysis demonstrated that the adsorption of protein on the laser micromachined surfaces is time-dependent. As the incubation time increases, the amount of protein adsorbed and the area on the surfaces that adsorbs protein will also increase.

With the capability of fabricating microstructures by CAD/CAM–geared laser micromachining and the ability of adsorption of protein on laser micromachined polymer surfaces, microstructures can be fabricated in our laser micromachining system to guide the flow, adherence and growth of protein on the material surfaces. Due to the ease of using different parameters in our CAD/CAM-geared laser micromachining system, microstructures with varying geometric features can be fabricated to provide insight of biological activities such as adherence and alignment of cells in different structures.

There are tremendous potential biomedical applications to integrate microstructures and biological species. Microchannels and circles can be used as reservoirs to allow flow of growth factors and facilitate cell growth. Some proteins can facilitate specific cell attachment and growth. With microstructures and proteins adsorbed on the laser micromachined surfaces, the microstructures can be employed as biointerfaces for attachment and growth of cells. Those cells can be controlled to grow and adhere in specific interested areas to be engineered as cell-ECM networks. Extracellular matrix (ECM) proteins are known to induce cellular adhesion, growth and proliferation. Application of ECM within these microchannels may allow controlled alignment of cells.

Due to the ease of achieving different machining parameters via selecting different laser parameters, microstructures with varying geometric features can be fabricated to provide insight into the difference of adherence and alignment of biological tissues in those microstructures. Laser micromachined microstructures can also serve as biomedical devices to deliver biological species from supply to specific spots.

In Fig.6.11 and Fig.6.12, square reservoirs connected with microchannels are shown. In Fig.6.11, the width of microchannel is about 70 microns. The microchannel shown in Fig.6.12 has width of 50 microns. 200 nanoliters fluorescent BSA solution was injected into the reservoir. Surface tension drove liquid solution into microchannels. Protein adherence and adsorption was guided in the microchannels.

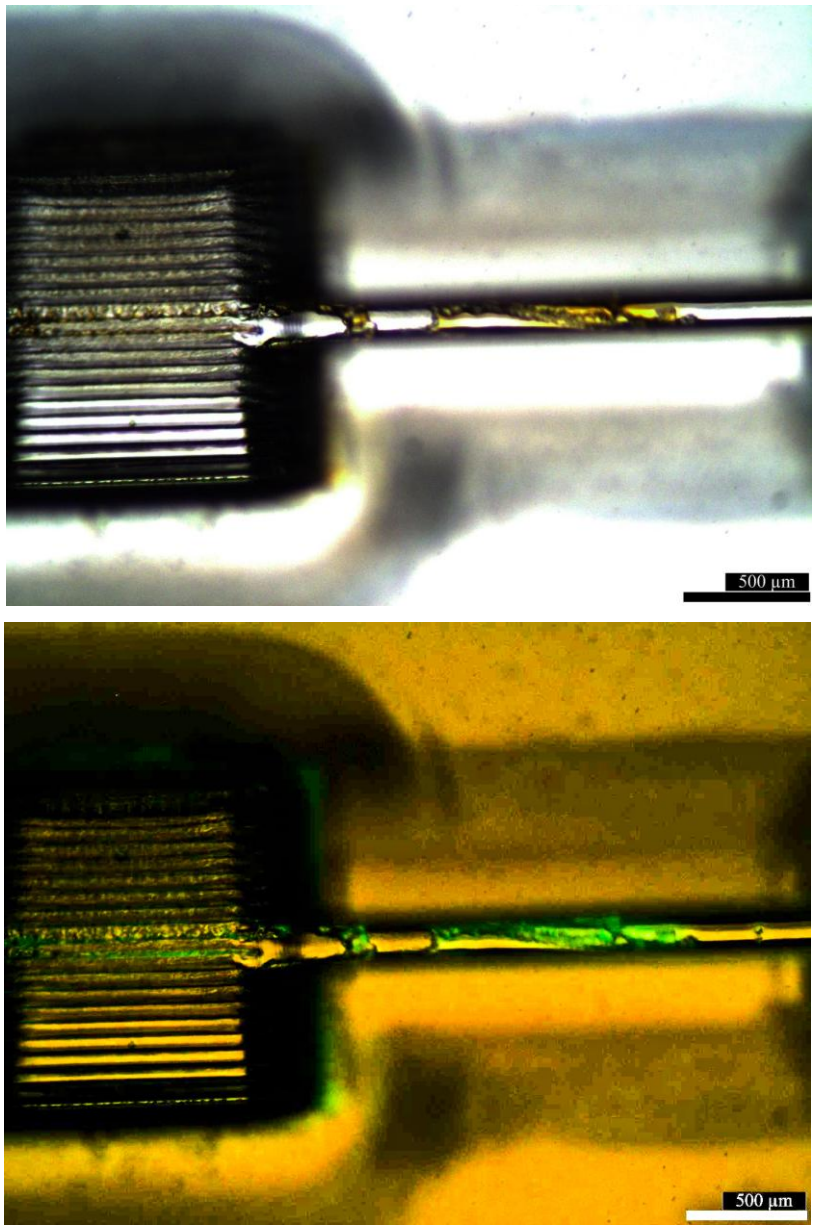

Fig.6.11 Adherence and adsorption of protein (supplied by the reservoir) guided by a microchannel with width of 70 microns

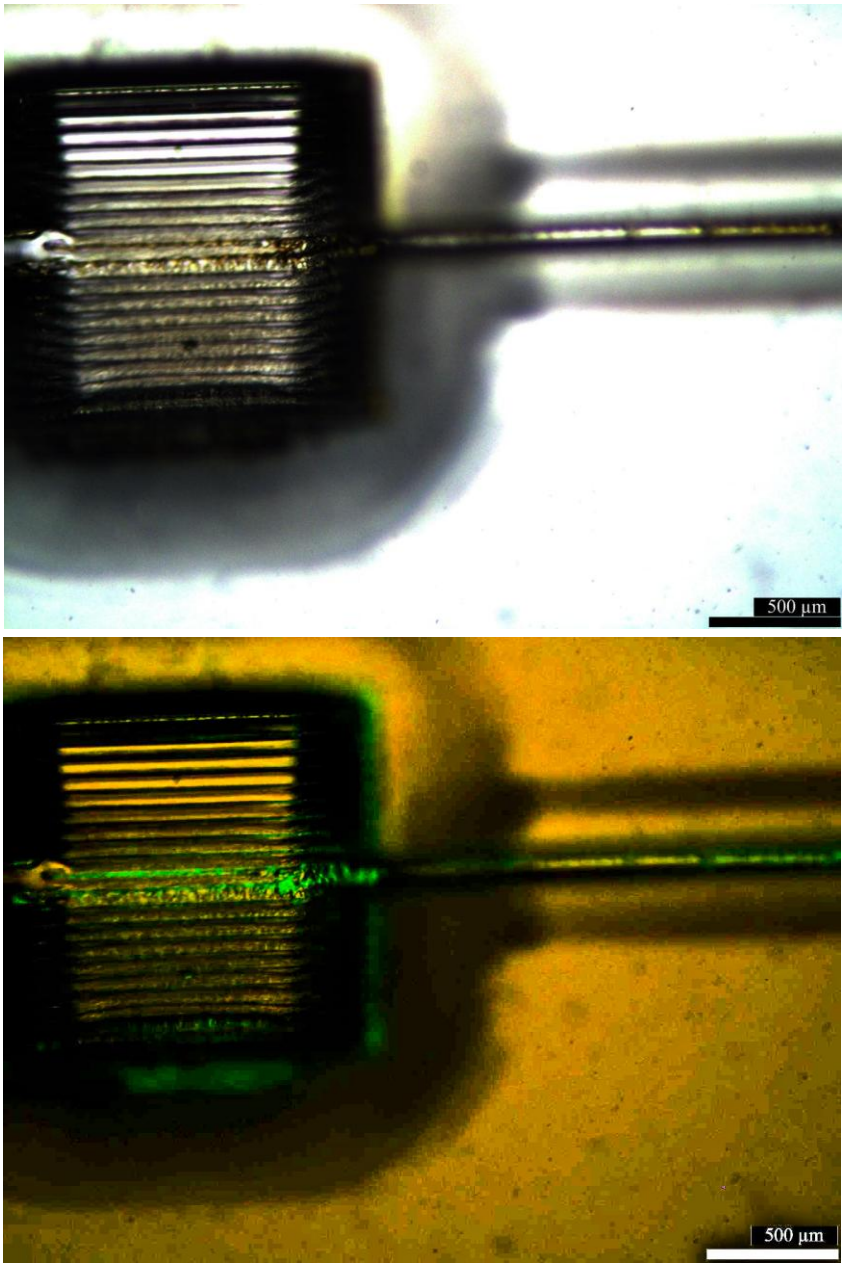

Fig.6.12 Adherence and adsorption of protein (supplied by the reservoir) guided by a microchannel with width of 50microns

Another example of biomedical devices is shown in Fig.6.13. A microchannel connects a reservoir with a circle well. The BSA solution was delivered from reservoir from reservoir to the well. This microstructure can be used as a delivery device to supply proteins from reservoir to a desired area.

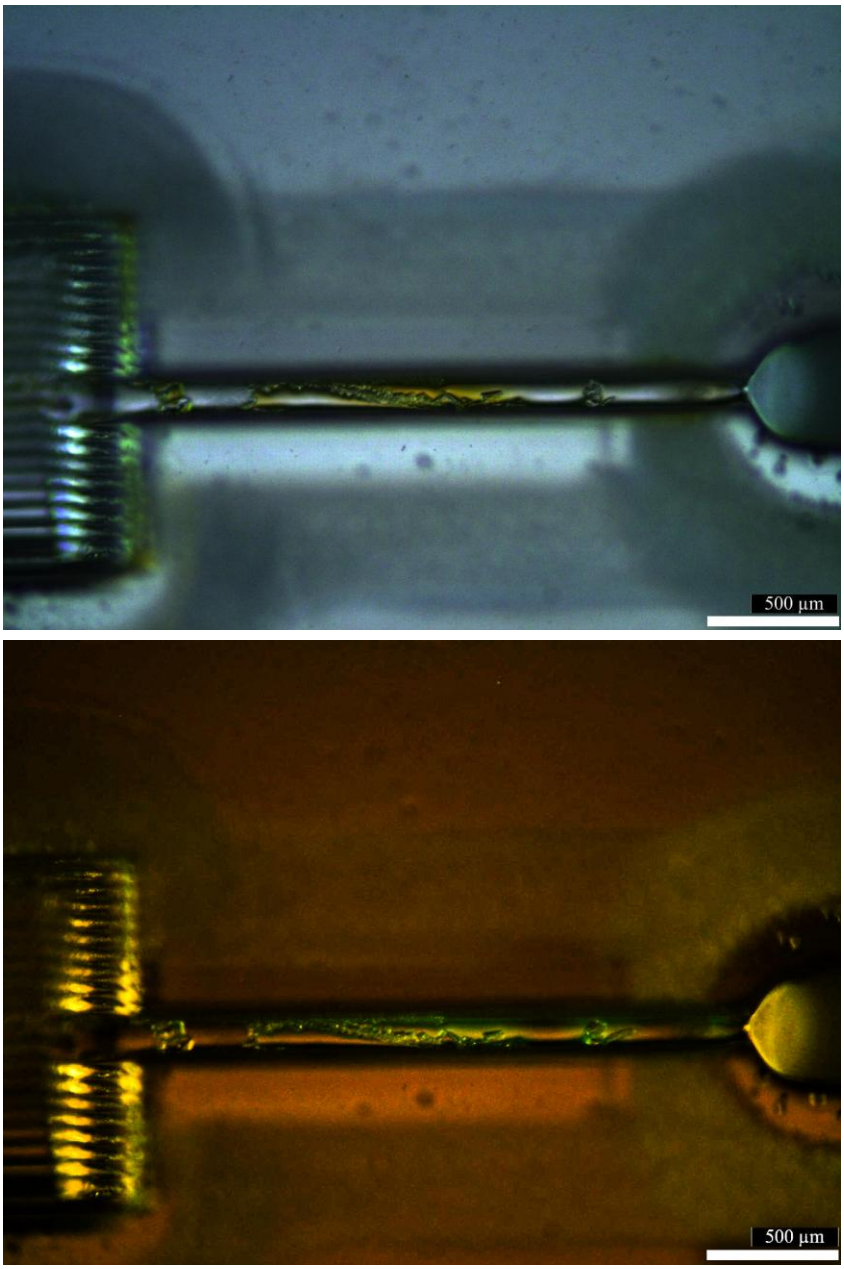

Fig.6.13 Protein delivered by a microchannel from a reservoir to a desired spot

CHAPTER 7

DESIGN AND MANUFACTURING OF BIOMEDICAL DEVICES TO CHARACTERIZE ELECTRICAL PROPERTIES OF BIOLOGICAL SPECIES

A biosensor or biochip is a kind of fabricated medical devices in micro scale to process, deliver and analyze biological species. Usually the electric property of biological species is interpreted by a medical device. Some applications including detection of protein binding to surface, small amount of pathogenic bacteria, antigen-antibody binding, and DNA hybridization have been explored by researchers with biosensors or biochips. Portable or so-called "point-of-care" biomedical devices become a trend. With laser micromachining, we can fabricate microstructures for portable biomedical devices in micro scale. In this chapter, we will discuss design and manufacturing of portable biomedical devices to measure the electrical properties of biological species by our laser micromachining system. Magnetotactic bacterium is a special microorganism that can produce magnetic particles. With the magnetic property, MTB has great potential to be used as biosensor or biochip. We will use the biomedical devices fabricated by laser micromachining to study the electric properties of MTB and explore the possibility of MTB to be used as biosensors or biochips.

7.1 Introduction

7.1.1 Potable biomedical devices

Biosensors are analytical instruments possessing a biomolecule as a reactive surface in close proximity to a transducer, which converts the binding of an analyte to the capturing biomolecule into a measurable signal [Radke 2004]. They can be used to detect existence of

specific molecules and diagnosis of diseases.

Diagnosis of diseases relies on the analysis and interpretation of chemical parameters. Currently most of diagnoses are performed in centralized laboratories with special equipment and experts. This process may delay diagnosis and treatment. Therefore, there is an emerging requirement to perform point-of-care testing outside laboratories with compact and portable devices [McMurray 2007]. To realize the point-of-care diagnosis, portable medical devices and diagnosis approach are needed.

A portable and handheld prototype medical device was developed to assess the DVT and related blood clotting conditions in [McMurray 2007]. Using this device, the blood concentration of D-dimer was measured through the detection of impedimetric parameter. Corresponding measurement and reporting system were also developed.

In [Radke 2004], a biosensor to detect and measure E. coli cells in food and water was developed based on MEMS system and immobilized antibodies. The sensor can detect the impedance change caused by bacteria immobilized electrodes. The resistivity of the bacteria cytoplasm and the capacitance of the lipid bilayer membrane cause the impedance change. The size and spacing of electrodes were optimized by FEM according to the size of bacteria.

In the work mentioned above, impedimetric detection works by measuring impedance changes produced by the binding of target molecules to receptors immobilized on the surface of microelectrodes. This method is very sensitive and very difficult to prepare surface of electrodes. For example, since the impedance change depends on the binding of targets to surface of electrodes, the optimization of geometry of electrodes is a very tricky problem. The immobilization of antibodies or enzymes is very complex and unreliable. It is very noise prone due to the species presence in biological samples.

In [Zee 2001], a micromachined polymer-based chemical gas sensor array to monitor and detect chemical gases was developed. Since it’s a sensor array, with each sensor geared with a different polymer composite, different gas or mixed gas can be detected by this sensor array. The existence and concentration of gases were indicated by the change rate of impedance.

7.1.2 Magnetotactic bacteria and magnetic particles

Magnetic particles are of great interests for researchers involving many applications. Those applications include magnetic carriers in immunoassays, drug delivery system, magnetic memory in electronic applications, manufacturing of magnetic tapes and printing inks, magnetic targeting of pharmaceuticals, cell separation, contrast-enhancement agents in magnetic resonance imaging, biosensors and bio-carriers [Matsunaga 2004; Schuler 1999]. For these applications, preparation of nano-sized magnetite particles with well-controlled size and shape is one of vital steps.

Magnetotactic bacteria (MTB) are a class of bacteria that exhibits the ability to orient themselves along the magnetic field lines of earth's magnetic field. These bacteria possess a magnetic moment due to the presence of membrane bounded crystals called magnetosomes within their structures [Schuler 1999]. Magnetosomes, synthesized by magnetotactic bacteria via biomineralization process, are uniformed and nano-sized magnetite particles enveloped by organic lipid membranes [Matsunaga 2004]. Fig.7.1 shows the images of magnetotactic bacteria and magnetosomes. With these features of magnetosomes, magnetosomes and magnetotactic bacteria have been applied in numerous applications by exploring their magnetic properties.

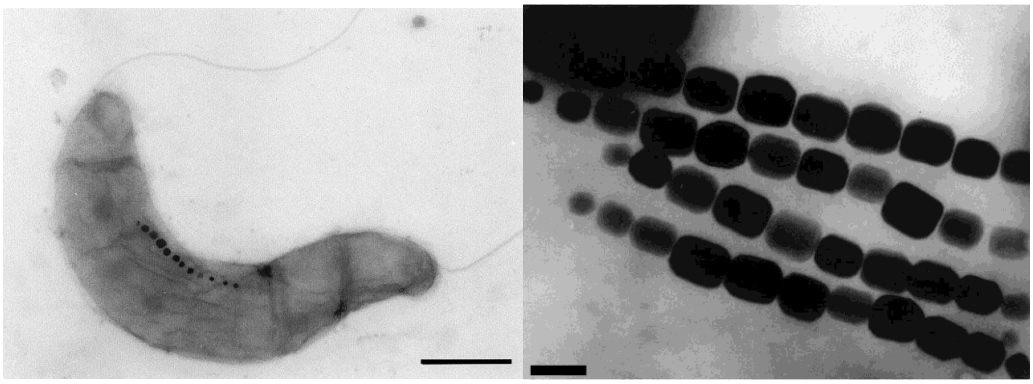

(a) Magnetotactic bacteria (b) magnetosomes

Fig.7.1 Images of magnetotactic bacteria and magnetosomes: (a) a magnetotactic bacteria cell; (b) magnetosomes in magnetotactic bacteria [Matsunaga 2004]

Magnetotactic bacteria was discovered in 1960s and formally introduced by Richard

Blakemore in 1975 [Schuler 1999; Blakemore1982]. Magnetotactic bacteria align themselves with the earth's magnetic field enabling them to navigate towards their ideal environment in sediments of ponds, streams or rivers in which they live [Bahaj 1994]. The biological phenomenon of microorganisms tending to move in response to the environment's magnetic characteristics is known as magnetotaxis, an instance of magnetoception. It is believed to aid these organisms in reaching regions of optimal oxygen concentration. This ability is based on intracellular magnetic structures, the magnetosomes, which comprise nanometer-sized, membrane-bound crystals of the magnetic iron minerals magnetite (Fe_3O_4) or greigite (Fe_3S_4) [Schuler 1999]. Magnetosome formation is achieved by a mineralization process with biological control over the accumulation of iron and the deposition of the mineral particles with specific size and orientation within a membrane vesicle at specific locations in the cell [Schuler 1999]. These crystals enable the bacteria to orientate themselves with respect to the earth's magnetic field and so swim towards their ideal environment within the sediments of ponds, streams or lakes in which they live. The effect of the earth's magnetic field means that in the northern hemisphere the majority of bacteria migrate towards the south pole of a bar magnet and vice a versa in the southern hemisphere [Bahaj 1994]. Magnetosomes are found in all magnetotactic bacteria and consist of magnetic iron mineral particles enclosed within membrane vesicles. In most cases the magnetosomes are organized in a chain or chains, which are fixed within the cell magnetite [Schuler 1999]. The crystals range in size from 30-60 nm [Bahaj 1994], while in [Schuler 1999] sizes of magnetosomes are reported as 35-120 nm

As mentioned above, magnetotactic bacteria produce magnetic nanocrystals enveloped by membranes. These magnetic nanoparticles are called magnetosomes. Magnetosomes can be harvest by separating bacteria from solutions following by burning membranes and drying. Magnetotactic bacteria and magnetosomes can be both used in various applications. In [Alphandery 2008], the differences between magnetotactic bacteria and magnetosomes were studied. Inside magnetotactic bacteria, magnetosomes are arranged in chains and provide a strong magnetic dipole. While extracted magnetosomes tend to be a denser packing of chains.

7.1.3 Magnetotactic cultivation

With the directed migration along the direction of external magnetic field, magnetotactic bacteria can be easily collected from natural samples. However, the cultivation of magnetotactic bacteria in laboratory is very difficult. Only a few types of MTB in nature have been successfully isolated in pure culture. Part of the difficulties lie in the life environment with complex pattern of vertical sediments and chemically stratified aquatic habitats [Schuler 1999]. This is very difficult to mimic in laboratory conditions. Successfully cultured MTB can be grown microaerobically on simple media containing short organic acids as a carbon source and ferric chelates as a source of iron [Schuler 1999]. Due to the lack of the oxygen-protective enzyme catalase in bacteria organism, bacteria cells have a strictly oxygen-dependent respiratory type of metabolism, but do not tolerate higher oxygen concentrations. Therefore, the control of low oxygen concentration in growth medium to achieve microaerobic conditions is very important. Currently M. magnetotacticum, M. gryphiswaldense and Magnetospirillum AMB-1 are three very popular MTB available in pure culture for research purpose. The maximum cell yields reported so far are 0.33 g/l (dryweight) for M. gryphiswaldense grown in a 100L fermenter and 0.34 g/l for Magnetospirillum AMB-1 grown at a four-liters scale [Schueler 1999]. Approximate 2.6 mg magnetosomes yielded per liter of cultured AMB-1 was reported in [Matsunaga 2004].

Isolation and purification of magnetosome particles from MTB species rely on magnetic separation and centrifugation techniques [Schueler 1999]. After separation of magnetotactic bacteria, the surrounding membrane stays intact. Crystal magnetosome particles can be isolated from these suspensions by solubilization of membrane of bacteria using a detergent. 2.6 mg or similar yield of magnetite can be isolated from 1L culture of Magnetospirillum AMB-1 and M. gryphiswaldense according to the reports in [Matsunaga 1997] and [Schueler 1997]. In a fed-batch culture system, a synthetic medium by continuously adding succinate and nitrate was used in [Matsunaga2004]. The productivity of magnetosome particles increased to 4.7 mg per liter of culture.

7.1.4 Applications of MTB: medical devices using MTB or magnetic particles

Commercial uses of bacterial mangetosome particles may include manufacturing of magnetic tape and printing inks, magnetic targeting of pharmaceuticals, cell separation and their application as contrast-enhancement agents in magnetic resonance imaging [Schuler 1999]. Since the bacteria can orient, migrate and accumulate in the stray fields originating from magnetic fields, the motion and change of magnetism or electrical impedance can be utilized to manipulate or carry particles and detect existence of some specific chemicals.

In [Bahaj 1995, 1998 & 2002], magnetotactic bacteria were used to remove heavy metals and radionuclides from wastewater. Both high-gradient magnetic separation and low-magnetic field were used to remove metals from water.

Orientation magnetic separation (OMS) represents a simple method that permits motile, field-susceptible magnetotactic bacteria (MTB) to be separated from water [Bahaj 2002]. This approach was used to decontaminate polluted water uptake of contaminants by the bacteria and their subsequent removal by applying magnetic fields in [Bahaj 2002]. In this system, an MTB culture flowing in a separation channel was subjected to a magnetic field perpendicular to the channel. By orienting and moving along the direction of magnetic field, bacteria would carry metals in polluted water and accumulate to the sides of channel. OMS can be used as a wastewater treatment process with the fact that MTB immobilize metal pollutants.

In [Bahaj 1994], a low magnetic field was applied on magnetotactic spirillum to study uptake and separation of heavy metals from solution at low ppm levels. Magnetotactic bacteria can be forced to swim in a required direction inside a chamber and then separated from solutions. Under low magnetic field, the bacteria were just orientated not attracted like when high gradient magnetic separation was applied. Nine heavy metals studied (Al, Cd, CO, Cu, Fe, Mg, Mn, Pb, Zn) at three different concentration were studied [Bahaj 1994].

This OMS process was used to recover of plutonium adionucleides from sediments in [Bahaj 1998].

Due to their magnetic property, MTB can be used in bio-sensor to detect the existence of some chemicals and carry particles to specific location following direction of external magnetic fields.

In [Denomme 2007], an MTB based bio-carrier was proposed to improve pathogenic bacteria detection time, specificity, and sensitivity. In this proposed system design, microbeads were modified with a coating of an antibody specific to target pathogenic bacteria. Then microbeads were attached to MTB. By applying external magnetic field, MTB with microbeads would be swimming through the solution containing target bacteria. Then the MTB were measured to determine the number of pathogenic bacteria. In this design, impedimetric parameters were measured to detect if target bacteria were attached to the microbeads. The detection system measured the changes in electrical impedance as MTB with microbead and pathogenic bacteria pass through a set of embedded microelectrodes. System design was optimized by FEM simulation including channel geometry and object sizes.

A detection system including microelectrodes and COMS technology based on integrated circuit to identify the present of micro-sized biological entities using magnetotactic bacteria being guided under the control of an external magnetic field of a few Gauss was studies preliminarily in [Fouladi 2007]. A microfluidic device and a microelectronic chip were fabricated onto a silicon substrate. Pairs of planar microelectrodes were patterned on the bottom of a microchannel and connected with the microelectronic chip. The electrical impedance change would be detected by integrated circuit when microbeads were pushed by MTB passed through a pair of microelectrodes. Then the impedance parameters were turned into digital decisions to reflect the presence of biological entities. The voltage across a pair of electrodes must always be greater than the bacterium's membrane breakdown voltage, which is approximately 0.2 to 1.5V [Fouladi 2007].

In [Martel 2006], the same research group studied the motion of MTB under external magnetic field and the potential applications to manipulate micro-particles. An average velocity 7.5 μm/s of 3 μm beads pushed by MTB with a peak velocity of 20 μm/s was observed along preplanned paths with a directional magnetic field of at least 0.5 G generated

from a small programmed electrical current. For a single Magnetospirillum gryphiswaldense and MC-1 MTB, average velocities greater than 16 and 12 μm/s with peak velocities of 22.5 and 60 μm/s could be achieved respectively. Therefore, MTB they could be used to manipulate efficiently suspended micro-objects in fluids for potential applications in microsystems such as lab-on-a-chip and Micro-Total-Analysis Systems [Martel 2006]. However, following this procedure, only 1% of the bacteria would attach to the microbeads and move along the line of an applied magnetic field. And the average velocity of this particular sample of MTB was lower than typical average speeds previously observed, which is 40–80 μm/s. This work showed that MTB can be precisely navigated in the microchannel with an external magnetic field for applications as bio-carriers.

7.1.5 MTB VS extracted magnetic particles

Magnetotactic bacteria belong to a unique group of microorganisms, which produce magnetic nanocrystals enveloped by biomembranes, called magnetosomes.

These magnetosomes are arranged in chains inside the bacteria and provide a strong magnetic dipole, which is used by the bacteria to swim along the direction of the earth's magnetic field. The whole magnetotactic bacteria maintain the chains of magnetosomes separated by large distances while the extracted magnetosomes favor a denser packing of the chains. However, the presence of biogenic material remaining after extraction prevents the chains of magnetosomes from reaching too high packing density [Alphandery 2008].

7.1.6 Detection and measurement of MTB and magnetic particle: magnetism and electrical impedance

To parameterize application of MTB or magnetic particles, we need some approaches to measure the magnitude of parameter changes caused by MTB, magnetic particles and specific targets. Normally the magnetism or electrical impedance caused by MTB or magnetic particles can be detected measured for practical applications.

Since the magnetism of MTB is very weak, it's not feasible to detect the magnetic field

by normal equipment. Various equipments including MFM (magnetic force microscope), SQUID microscope and VSM (Vibrating Sample Magnetometer) were used to detect and measure the magnetic field caused by MTB or nano magnetic particles. SQUID magnetic microscope was developed based on a high transition temperature dc SQUID [Chemla 1999]. It is extremely sensitive to magnetic field produced by nearby specimens. The magnetic field produced by MTB was detected and measured using SQUID microscope in [Chemla 1999]. The SQUID microscope must be maintained at 77K inside a vacuum enclosure. MTB were brought to within 15μm of a SQUID for measurement. Nonmotile bacteria in zero magnetic field, nonmotile bacteria in a magnetic field, motile bacteria in zero magnetic field and motile bacteria in a magnetic field were tested to demonstrate the ability of measurement of magnetotactic bacteria. In [Chemla 2000], the same equipment was used to study magnetic nanoparticles carrying antibody directed against the targets.

In [Alphandery 2009; Matsunaga 1987], VSM (vibrating sample magnetometer) was used to measure magnetism of magetotactic bacteria and magnetic particles. The samples were placed inside a capsule mounted in an electromechanical transducer. Vibrating sample magnetometers is normally operated over a temperature range of 2.0 to 1050 K.

SQUID microscope and VSM are very sensitive to weak magnetic field. They are ideal equipment to detect and quantify the magnetism caused by magnetotactic bacteria and nano magnetic particles. However the environment to use these facilities is very strict and sample preparation is very difficult. For SQUID microscope, the operation temperature must be maintained at 77K inside a vacuum enclosure or even lower. The samples have to put very close to it. The distances between samples and vacuum enclosure have great effects on the measurement of magnetism. Sample preparation for VSM is very hard. The sample must be confined in a specific space. Both of them are not competitive candidate of point-of-care detection and measurement.

Compared with magnetism measurement, electrical impedance measurement has its own advantages. Basic ideas are using electric circuit to measure impedance of specimen or interfacial impedance reflecting the changes in the electrolyte concentration gradient at the interface. Since the equipment of electrical impedance measurement is much inexpensive

compared with VSM or SQUID microscope and sample preparations are much easier, electrical impedance measurement may be a better fit for portable biosensor.

In this chapter, we will discuss design and manufacturing of medical device to measure the electrical impedance of biological species. Using this device, electrical impedance characteristics of magnetotactic bacteria will be measured and analyzed to explore its potential in application of medical devices as biosensors. In the remaining parts of this chapter, the design and fabrication of medical devices in our lab-built excimer laser micromachining. The cultivation of magnetotactic bacteria will be also introduced. Then a set of experiments will be performed on different biological solutions with fabricated biosensor. Finally, results will be presented.

7.2 Design and Fabrication of Medical Device to Characterize Electrical Properties of Biological Species

7.2.1 Design

The proposed biosensor is composed of two reservoirs connected by a microchannel. The dimension of reservoirs is 500μm x500 μm. The width of microchannel is 200 μm with length of 500 μm. In each of two reservoirs, an electrode was patterned with gold wire connected with four probes system to measure electrical impedance of biological species. The design of proposed biosensor is shown in Fig.7.2 and Fig.7.3with critical dimensions marked.

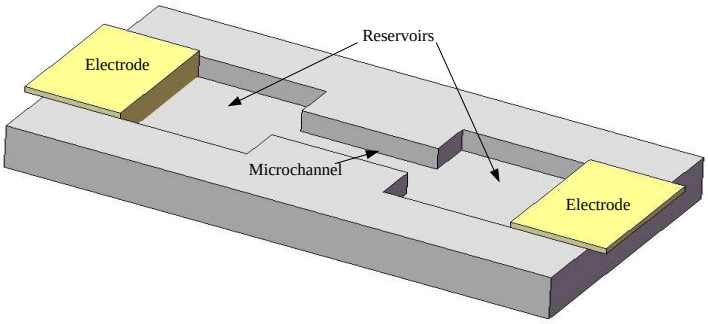

Fig.7.2 Design of biosensor consisting of reservoirs, microchannel, electrodes and polyethylene substrate

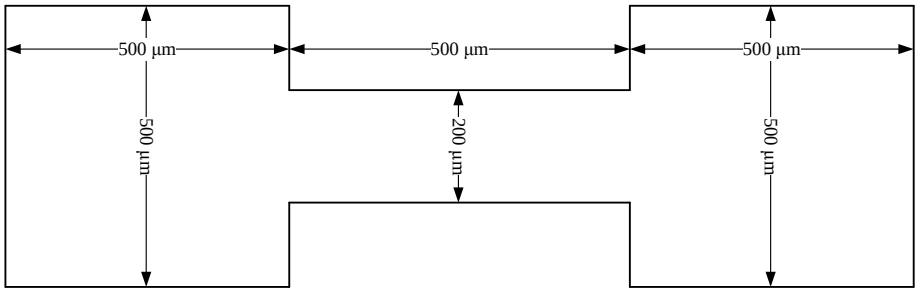

Fig.7.3 Design of biosensor with detail dimensions

7.2.2 Fabrication

The proposed biosensor was fabricated in our lab-built excimer laser micromachining system. The laser parameters were set based on the parameters study in chapter 3. The number of pulses per area was set to 200. Base on Fig.7.4, the depth of microchannel and reservoirs was 480 µm approximately. Based material of proposed biosensor is high density polyethylene. The fabricated biosensor with electrodes patterned is shown in Fig.7.2.

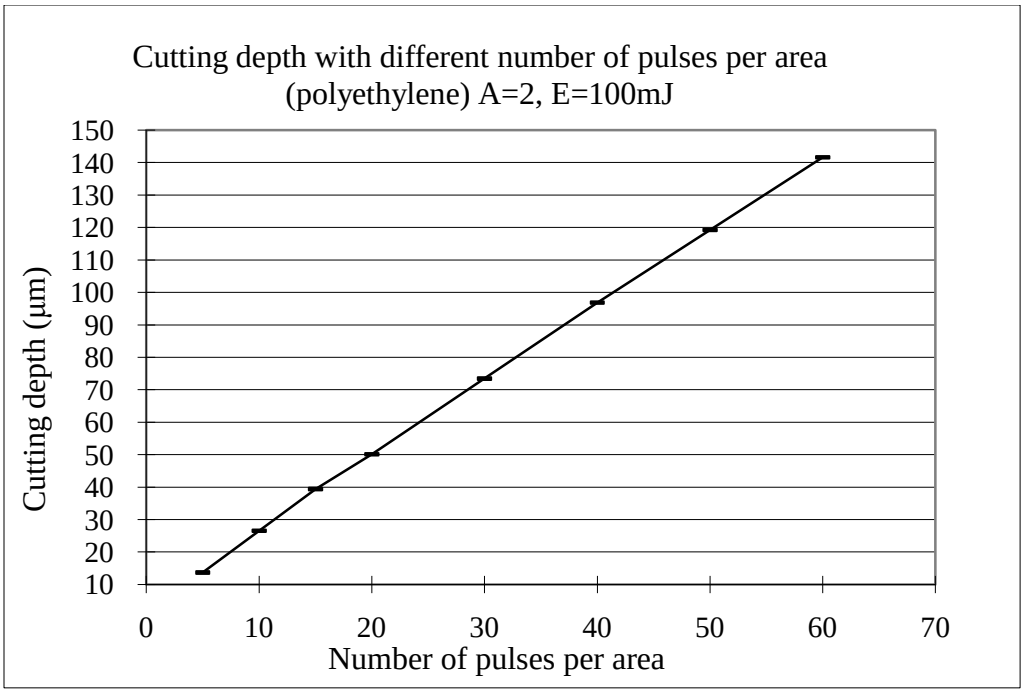

Fig.7.4 Cutting depth as a function of number of laser pulses per area

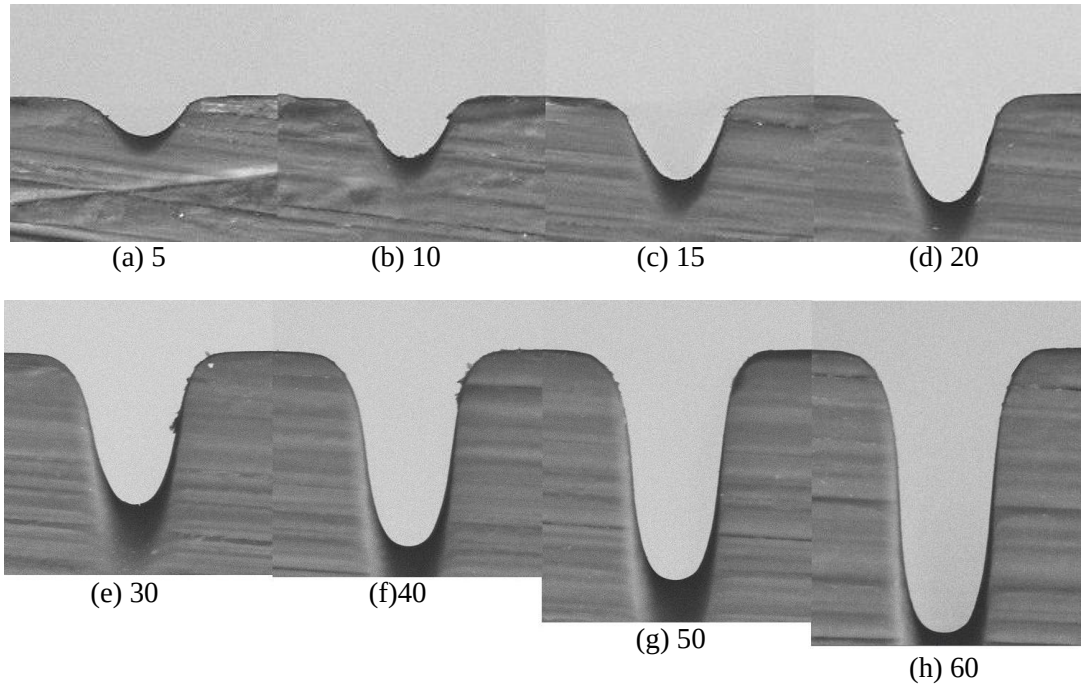

Fig.7.5 SEM images for microchannels cut by different number of pulses per area (polyethylene): (a) P=5; (b) P=10; (c) P=15; (d) P=20; (e) P=30; (f) P=40; (g) P=50; (h) P=60.

7.2.3 Cultivation of magnetotactic bacteria

The *magnetospirillum sp.* was purchased from ATCC with ATCC revised magnetic spirillum growth medium (MSGM). The MSGM was mixed with ingredients as shown in Table 7.1. The bacteria were cultivated, insolated and incubated according to standard protocol for 14 days.

Table 7.1 Ingredients of living medium for MTB

Name	Amount
Distilled water	1.0 L
Wolfe's Vitamin Solution	10.0 ml
Wolfe's Mineral Solution	5.0 ml
0.01 M Ferric Quinate	2.0 ml
0.1% Resazurin	0.45 ml
KH2PO4	0.68 g
NaNO3	0.12 g
Ascorbic acid	0.035 g
Tartaric acid	0.37 g
Succinic acid	0.37 g
Sodium acetate	0.05 g
Agar (for semi-solid medium)	1.3 g

7.3 Experiment Setup for Electrical Characterization

With fabricated biosensor and cultivated MTB, a series of experiment will be carried out to characterize the electrical parameters of MTB solutions to explore the potentials in application of MTB as biosensors. The two-point I-V sweep will be performed on different solutions including deionized water, pure ATCC medium, solution containing bacteria and solution containing bacteria with double concentration. 500 nl of each biological solutions will be injected into reservoirs and microchannel to measure the electrical characteristics. For each solution, current and voltage are used as independent variables respectively with output voltage and current recorded. The U-I curve representing the electrical characteristics will be compared for different ranges of input and different solutions.

When current is used as independent variable, the circuit ranging from 0 μA~10 μA, 0

μA~20 μA, 0 μA~50 μA and 0 μA~100 μA will be applied via our four-probe system. Since the voltage capacity of this system is 40 V, we cannot read any output of voltage with 0 μA~100 μA circuit for solutions with high impedance. We will also use the voltage as the independent variable and the current as the output, the voltage ranges from 0 V~5V. 0 V~10 V, and 0 V~20. The measurement model can be presented as the figure below.

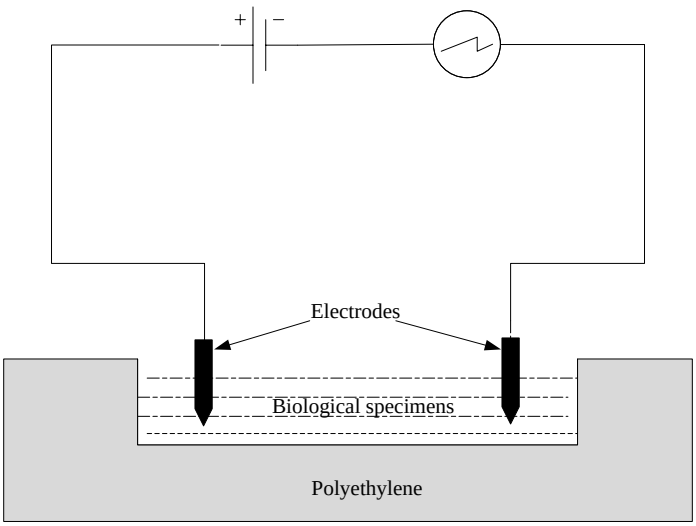

Fig.7.6 The prototype of circuit to characterize the electrical property of biological solutions

7.4 Results and discussions

Measuring the changes of electrical conductivity of biological specimens is a convenient method to qualitatively and quantitatively trace the biological activities of microorganisms. Bacterial metabolism changes the electrolyte concentration in the suspension medium, then significantly altering its electrical characteristics. The electrical impedance between two electrodes includes the impedance of solution, impedance of bacteria, impedance of electrodes, and capacitance at the interface of solution and electrodes. The impedance of solution includes solution resistance and the capacitance of dielectric solution. The impedance of bacteria includes the resistance of cytoplasm of bacteria, the resistance and capacitance of the call membrane. With electrical property measurement, the changes in conductivity of biological specimens containing MTB can serve as an indication parameter

when MTB solution is used in biosensor.

The first set of experiment is to apply current ranging from 0~10 μA, 0~20 μA, 0~ 50 μA and 0~100 μA on biological solutions via two electrodes. Output voltage is recorded with 100 measurement points sampled. Fig.7.7 shows the U-I curve of ATCC medium with different ranges of current as input. According to the diagram, when input current is small (less than 15 μA), the increasing of recorded output voltage is relatively large. When input current is larger than 15 μA, the slope of the curve is much smaller.

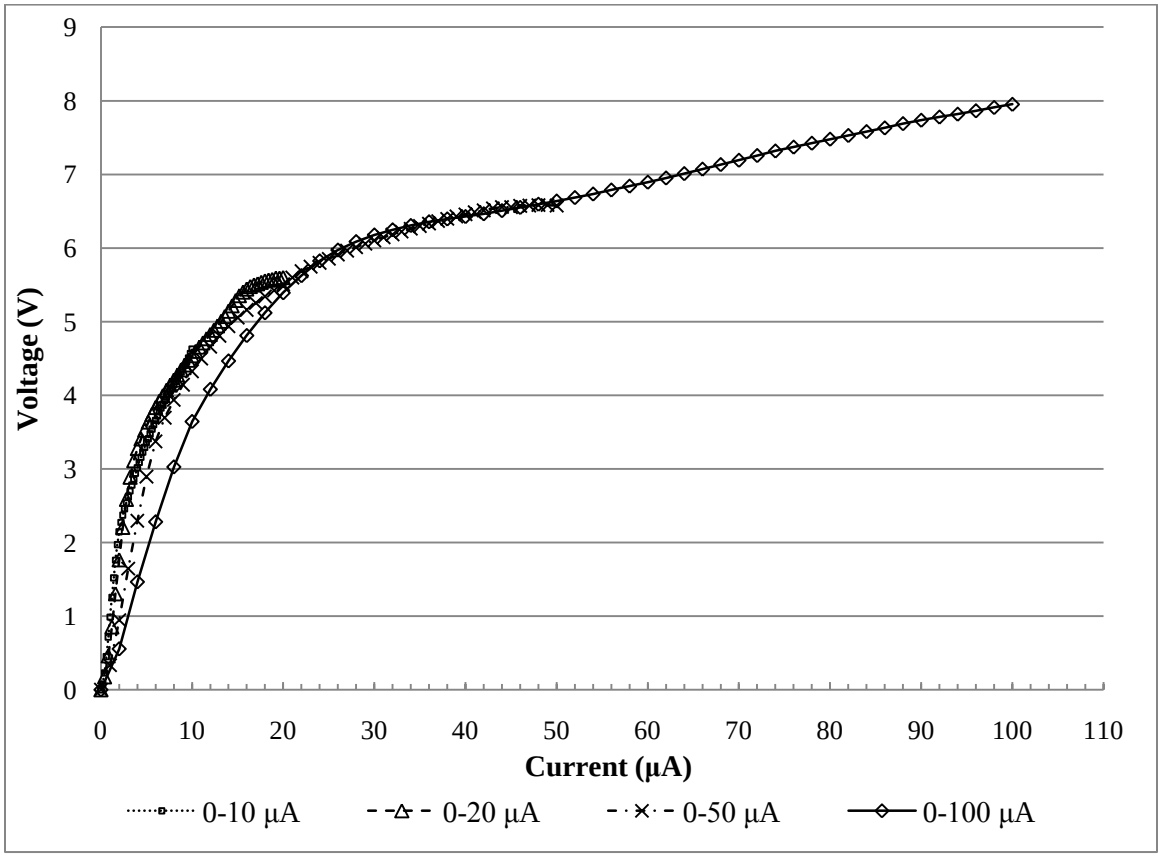

Fig.7.7 The U-I curve for ATCC medium with different input of current

Similar pattern can be also observed in Fig.7.8 and Fig.7.9 for regular MTB solution and double concentration MTB solution. The turning point of U-I curve for these two solutions happen at I=10 μA and I=5 μA approximately. The comparison for three solutions can be seen in Fig.7.10.

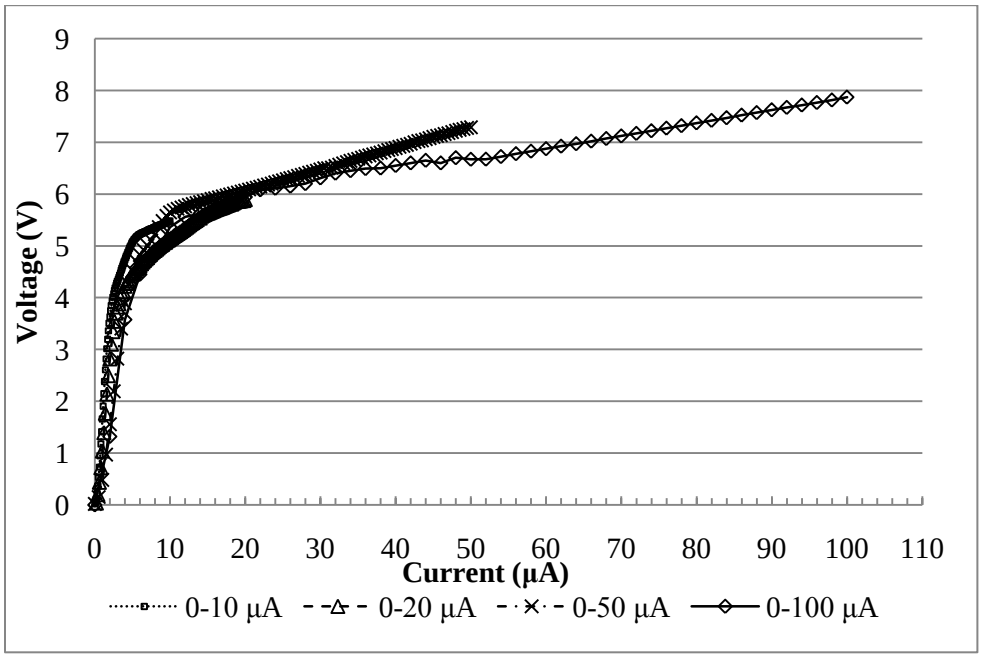

Fig.7.8 The U-I curve for bacterial solutions with different input of current

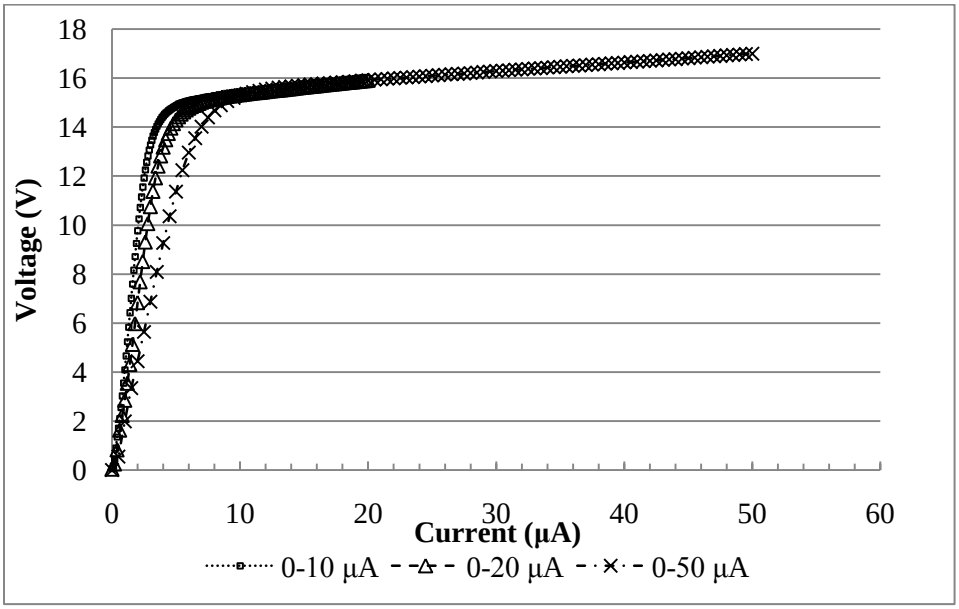

Fig.7.9 The U-I curve for double concentration bacterial solutions with different input of current

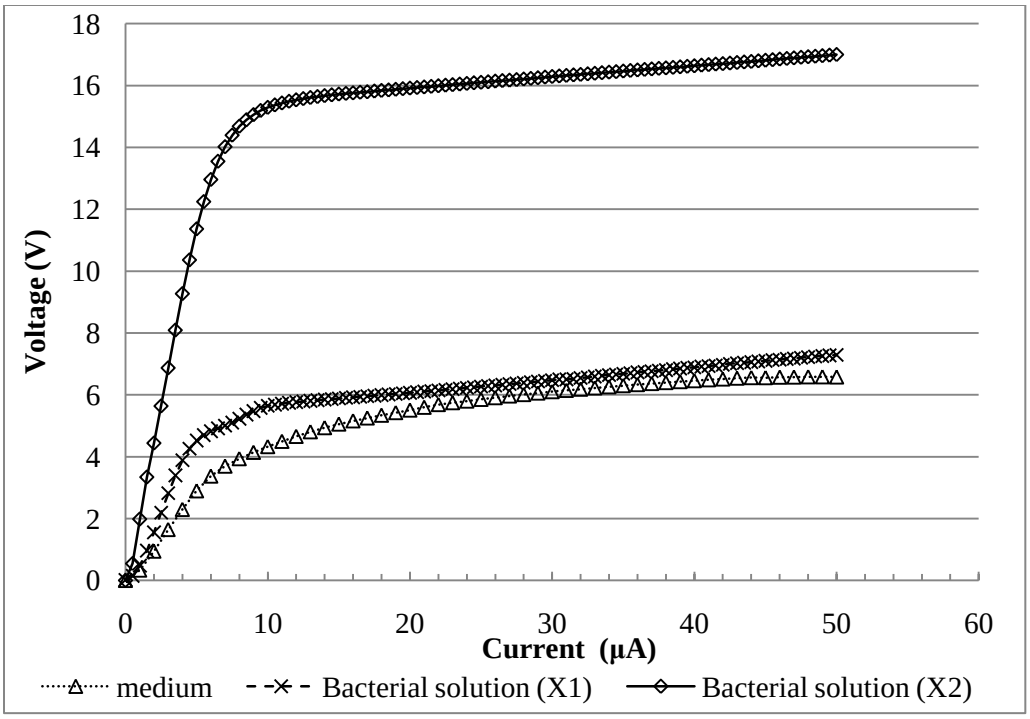

Fig.7.10 Comparison of electrical properties of different solutions with different input of current

This observation was corroborated in the experiments that voltage was used as input with output current recorded. For each specimen, 0~5V, 0~10V and 0~20V voltage were applied. Output currents on 100 sample points were measured. At the beginning when input voltage is <4V for ATCC medium, <8V for bacterial solution and <16V for bacterial solution with double concentration, the output currents are very small. When input voltage is higher than some threshold value, output current will increase rapidly. According to the comparison of three different specimens, pure ATCC medium, bacterial solution and double concentration bacterial solution show different threshold voltages.

For the pure ATCC medium, the measured impedance parameters only consist of impedance of solution, impedance of electrodes, impedance at the interface of electrodes and solutions, not including impedance caused by bacteria. Essentially the ATCC medium is electrolyte containing acids, bases and salts. The input voltage supplied the energy necessary to discharge the ions in the solution. When the electrical potential between two electrodes is high enough to achieve the electrolysis, the output current can be read and recorded. Thus, at

the beginning when input voltage is small, the output current is 0 or very small since the energy provided is not high enough to achieve electrolysis. When the input voltage is high enough, the output current increases as the input voltage increases. Because the input energy is only to compensate the energy of electrolysis, the threshold voltage is not very high as shown in Fig.7.11.

When the concentration of bacterial cells increases, the impedance of bacteria including the resistance of cytoplasm of bacteria, the resistance and capacitance of the call membrane becomes a more and more important factor. With electrical fields applied via electrodes, the structural rearrangement of cell membrane will occur. When the potential on the membrane exceeds the dielectric breakdown voltage of the membrane, pores will be formed on cells' membranes and the resistance of cell will be dropping significantly. This phenomenon correspond the jump of output current in Fig.7.11, Fig.7.12, Fig.7.13 and Fig.7.14. Therefore, in this situation the input electrical circuit will apply not only the energy for electrolysis, but also for the breakdown of cell membrane. When the concentration of bacterial cells is higher, the cell resistance becomes more dominating. As a result, the phenomenon of drop of cell's resistance becomes more significant. The turning point as indicated in the diagrams where the jump of output current occurs is sharper.

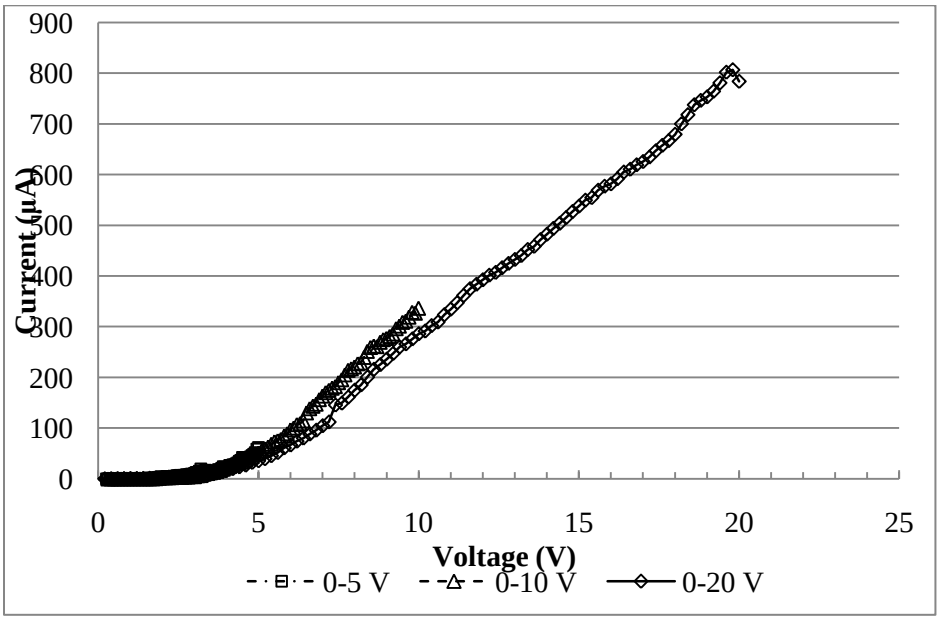

Fig.7.11 The U-I curve for ATCC medium with different input of voltage

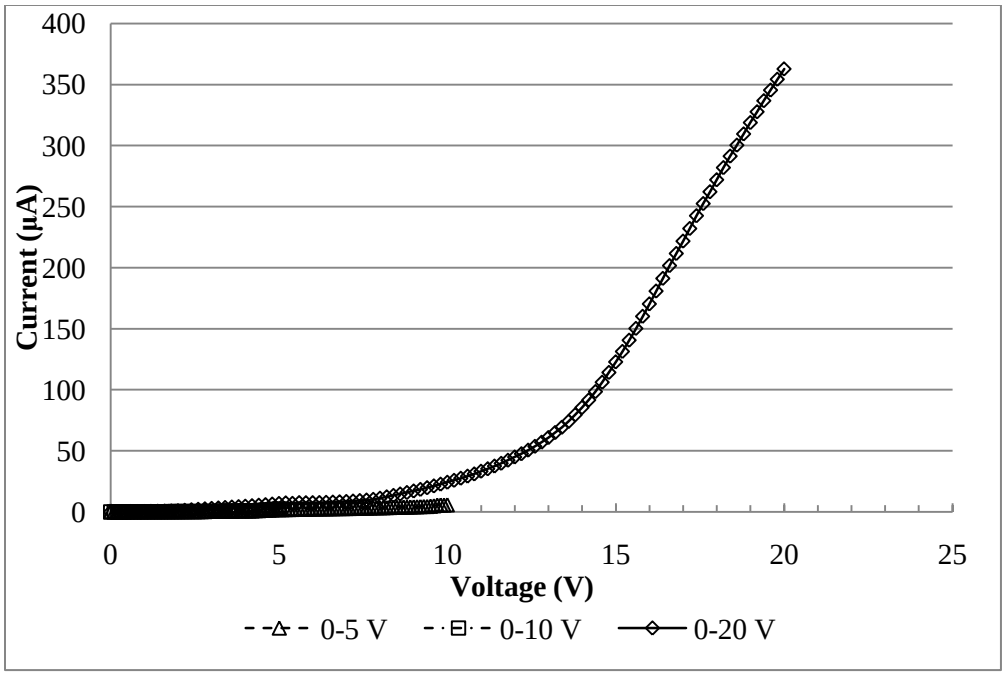

Fig.7.12 The U-I curve for bacterial solutions with different input of voltage

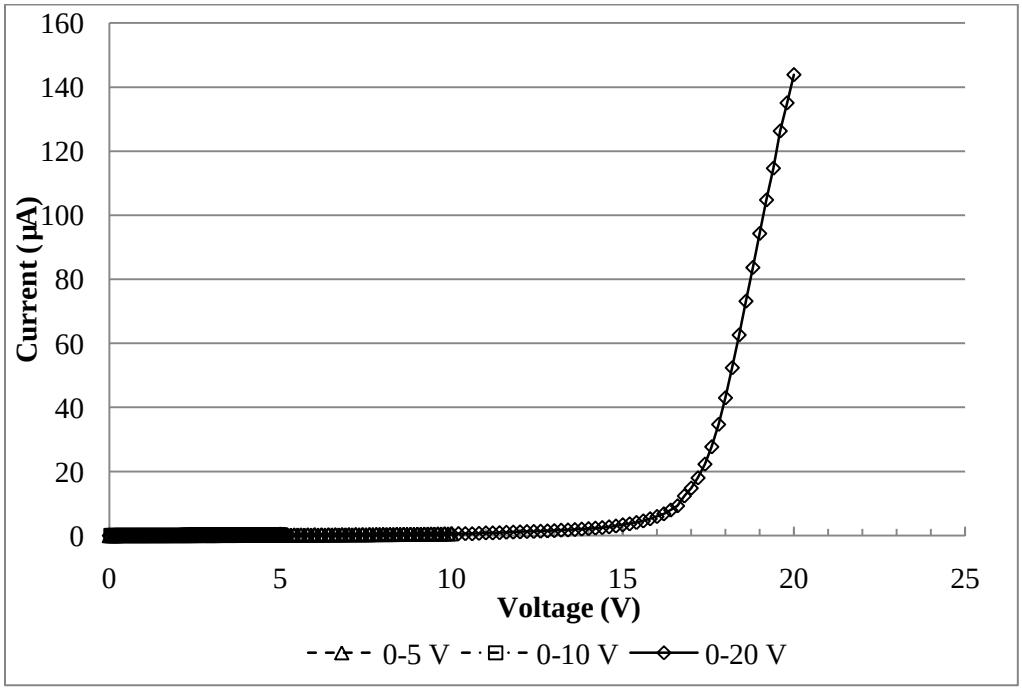

Fig.7.13 The U-I curve for double concentration bacterial solutions with different input of voltage

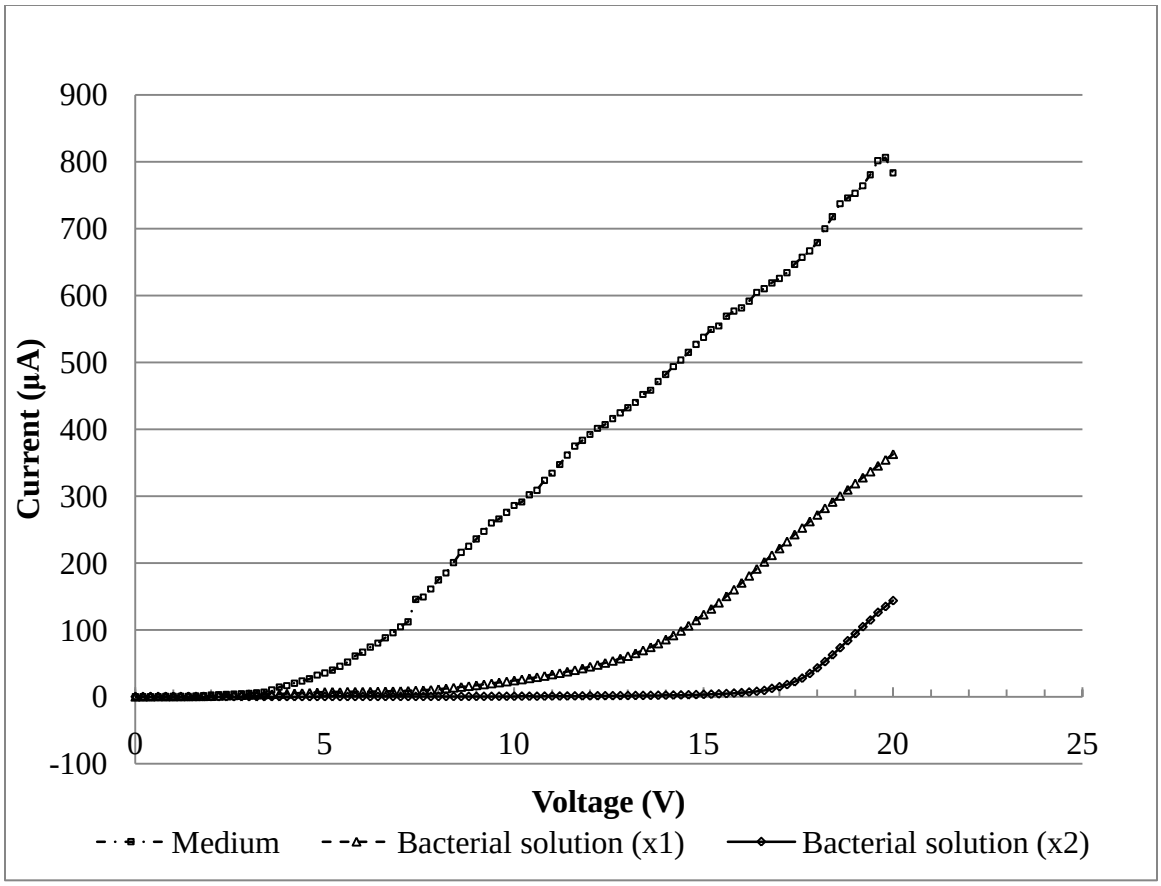

Fig.7.14 Comparison of electrical properties of different solutions with different input of current

During the experiment, the biological specimens inside the reservoirs and microchannel will modify the surfaces of electrodes. It will introduce the capacitance created from the oxide separation of the electrodes. So the electrodes were cleaned after each experiment and new electrodes were patterned in the device for each set of experiments to reduce the effects by modified electrode surfaces.

7.5 Conclusions

In this chapter, design and manufacturing of biomedical devices to measure electrical parameters of biological species is introduced. Laser micromaching is capable of fabricating portable biomedical devices. In many cases, electrical characterization of biological tissues

can be interpreted as an indication of biological activities. So devices to characterize electrical properties of bio-tissue have great potential demand and application. With its flexibility and versatility, laser micromachining is a good candidate for manufacturing of biomedical devices to measure electrical characteristics of bio-tissues.

CHAPTER 8

CONCLUSIONS AND FUTURE RESEARCH WORK

The main objectives of this research are to study laser micromachining techniques and explore its applications in manufacturing of biomedical devices in micro scale. Basically two aspects of problems were discussed. Firstly of all, laser micromachining was investigated from manufacturing perspective. Machining parameters, machined surface error analysis and application of CAD/CAM in laser micromachining were studied. Then from the biomedical application point of view, design and manufacturing of biomedical devices using laser micromachining was discussed. In this chapter, we will summarize this research work and discuss the future research work

8.1 Conclusions

The work of this research is summarized as follows:

- Laser micromachining is a material-dependent manufacturing process. To use laser micromachining to fabricate desirable microstructures, the relationship between laser parameters, equipment parameters and machining parameters has to be set up for specific materials. We designed three experiments to study the machining performance under different laser parameters for three biocompatible polymers. Based on the comparison, polyethylene and PMMA show better surface quality than PDMS. Laser-ablation depth is linearly dependent on the number of laser pulses per area in our experiments, which is a merit for manufacturing purpose. The quantitative relationship between cutting depth/width and laser energy/laser beam size was built based on statistical results from plenty of experiments. This mapping relationship provides a good basis for proper selection of laser parameters to achieve desirable machining parameters.

- Machined surface error is a major problem in manufacturing. Unlike conventional machining process, there are some special issues in laser micromachining when the machined surface error problem is brought up. The overlapping effects, which are caused by two adjacent laser pulses, were introduced. An analytical model to calculate and predict machined surface errors considering overlapping effects had been proposed based on the mechanism of laser ablation and energy profile of laser beam. Via this model, machined surface errors can be calculated given the input including cutting width, depth and distance between two adjacent laser pulses. Also, give a specific tolerance an optimal parameter can be generated for the purpose of process planning. Experiment results and simulation results have been compared. It showed good match between our model and experiment measurement.
- Manufacturing process and biological living cells are two vital components in biomanufacturing. An integrated biomanufacturing system was proposed including laser micromachining, surface analysis, biological deposit techniques and biological species.
- Proteins play an important role in biomedical research. The adsorption of Bovine Serum Albumin on laser micromachined polyethylene and PDMS surfaces was studied. The adsorption of protein on laser micromachined surfaces is time-dependent. EDS on SEM was utilized to analyze the laser micromachined surface after samples were incubated with BSA solution for different time periods. Fluorescent images were captured using UV microscope and were used to analyze the protein adsorption. With the capability of fabricating microstructures by laser micromachining and the adsorption of proteins on laser micromachined surfaces, biomedical devices were fabricated to guide the adherence of protein as biointerfaces and deliver proteins from reservoir to specific spot.
- Electrical properties of biological tissues are usually interpreted as indicators of biological activities in biosensor. A biomedical device to characterize the electrical properties of biological tissues was fabricated using laser micromachining. Electrical parameters of Magnetotactic bacteria were analyzed using our device.

8.2 Future Research Work

In this work laser micromachining technique was studied for manufacturing of biomedical devices combined with biological species. It demonstrated the capability of laser micromachining in biomanufacturing and biomedical applications of laser micromachining. Based on the developed techniques in this work, future research can be extended in the following directions:

- We already built a model to calculate the machined surface error in laser micromachining. The results shows good match with the experiments. However, those studies are on the flat surfaces. In many cases curved surfaces are needed in microstructures. So it's necessary to study the machined surface errors on curved surface machined by curved surfaces. More modeling and simulation work is needed to explore the machined surface errors on curved surfaces
- In our laser micromachining system, laser beam was shot vertically on the materials surfaces. That being said, this system is a 3-axis machining system. The process of laser ablation when laser beam has a tilt angle related to material surfaces may worth some research efforts. This future work may also provide some clues for 5-axis laser micromachining systems.
- In our machined surface errors analysis, we assume the laser energy is conservative along the propagation path in the air. In a very short path, this assumption is valid. While more accurate energy profile can be achieved by integral of energy flux considering energy loss. Based on this, a better analytical model will be available when we analyze the process of laser micromachining.
- As mentioned in chapter 3 and chapter 4, the heat effect is neglectable in excimer laser micromachining on polymers. However, in other laser process on other materials, heat effects may become an important factor when we are trying to model the laser micromachining process. So incorporating the heat effect into an analytical model to analyze laser micromachining process will be meaningful in some cases.

The problems mentioned above are by no means a complete list. It shows there are still

lots of in-depth unknown areas in laser micromachining and its applications. It is expected that related research will continue to boom involving various engineering and science disciplines.

REFERENCES

[Abbasi 2006] Abbasi, F., Mirzadeh, H., & Simjoo, M. (2006). Hydrophilic interpenetrating polymer networks of poly(dimethyl siloxane) (PDMS) as biomaterial for cochlear implants, *Journal of Biomaterials Science, Polymer Edition, 17*(3), 341-355.

[Alphandery 2008] E. Alphandery, A. T. Ngo, C. Lefevre, I. Lisiecki, L. F. Wu, & M. P. Pileni (2008). Difference between the Magnetic Properties of the Magnetotactic Bacteria and Those of the Extracted Magnetosomes: Influence of the Distance between the Chains of Magnetosomes, *J. Phys. Chem. C, 112*(32), 2304-12309.

[Alphandery 2009] E. Alphandery, Y. Ding, A. T. Ngo, Z. L. Wang, L. F. Wu, & M. P. Pileni (2009). Assemblies of Aligned Magnetotactic Bacteria and Extracted Magnetosomes: What Is the Main Factor Responsible for the Magnetic Anisotropy, *ACS Nano, 3*(6), 1539-1547.

[Arcos 2001] D. Arcos, C. V. Ragel & M. Vallet-Reg (2001). Bioactivity in glass/PMMA composites used as drug delivery system, *Biomaterials, 22*(7), 701-708.

[Asgari 2004] S.A. Asgari, A.M.S. Hamouda, & S.B. Mansora，et al (2004), Finite element modeling of a generic stemless hip implant design in comparison withconventional hip implants, *Finite Elements in Analysis and Design, 40*, 2027-2047.

[Bahaj 1995] AS. Bahaj & P.A.B. James (1995). Metal Uptake and Separation Using Magnetotactic Bacteria, *IEEE TRANSACTIONS ON MAGNETICS, 30*(6), 4707-4709

[Bahaj 1998] A.S. Bahaj, I.W. Croudace, P.A.B. James, F.D. Moeschler, & P.E. Warwick (1998). Continuous radionuclide recovery from wastewater using magnetotactic bacteria, *Journal of Magnetism and Magnetic Materials, 184*, 241-244.

[Bahaj 2002] A.S. Bahaj, P. A. B. James, & F. D. Moeschler (2002). Efficiency enhancements through the use of magnetic field gradient in orientation magnetic separation for the removal of pollutants by magnetotactic bacteria, *Separation Science and Technology, 37*(16), 3661-3671.

[Barsch 2003] N. Barsch, K. Korber, A. Ostendorf, & K. H. Tonshoff (2003), Ablation and cutting of planar silicon devices using femtosecond laser pulses, *Appl. Phys. A 77*, 237-242.

[Baudach 2000] S. Baudach, J. Bonse, J. Kruger, & W. Kautek (2000). Ultrashort pulse laser ablation of polycarbonate and polymethylmethacrylate, *Applied Surface Science, 154-155*, 555-560.

[Black 1992] Jonathan Black(1992). *Biological performance of materials: fundamentals of biocompatibility*. New York: Marcel Dekker.

[Blakemore 1982] Richard P. Blakemore (1982), Magnetotactic bacteria, *Annu. Rev. Microbiol.,36*, 217-238

[Blau 1997] Blau J (1997), European effort refines medical prototyping. *Machine Design*, 36-38

[Bobyn 1982] Bobyn JD, Cameron HU, Abdulla C, Pilliar RM, & Weatherly GC(1982). Biologic fixation and bone modeling with an unconstrained canine total knee prosthesis, *Clinical Orthopedic, 166*, 301-312.

[Böhlen 2003] Ines Stassen Böhlen, Jim Fieret, Andrew Holmes, & Kin Wei Lee (2003). CAD/CAM software for an industrial laser manufacturing tool, *Proc. SPIE, 4977*, 198.

[Chemla 1999] Y. R. Chemla, H. L. Grossman, T. S. Lee, John Clarke, M. Adamkiewicz & B.

B. Buchanan (1999). A New Study of Bacterial Motion: Superconducting Quantum Interference Device Microscopy of Magnetotactic Bacteria, *Biophysical Journal, 76*, 3323-3330.

[Chemla 2000] Y. R. Chemla, H. L. Grossman, Y. Poon, R. McDermott, R. Stevensi, M. D. Alper & J. Clarke (2000). Ultrasensitive magnetic biosensor for homogeneous immunoassay, *PNAS, 97*(26), 14268-14272.

[Cheng 2004] Ji-Yen Cheng, Cheng-Wey Wei, Kai-Hsiung Hsu & Tai-Horng Young (2004). Direct-write laser micromachining and universal surface modification of PMMA for device development, *Sensors and Actuators B, 99*, 186-196.

[Choi 1998] Choi BK & Jerard RB (1998). *Sculptured surface machining*. Dordrecht: Kluwer Academic Publishers.

[Choi 2004] Kyung Hyun Choi, Johan Meijer, Takahisa Masuzawa & Dae-Hyun Kim (2004). Excimer laser micromachining for 3D microstructure, *Journal of Materials Processing Technology, 149*, 561–566

[Dear 2008] Fraser C. Dear, Jonathan D. Shephard, Xin Wang, Julian D. C. Jones & Duncan P. Hand (2008). Pulsed Laser Micromachining of Yttria-Stabilized Zirconia Dental Ceramic for Manufacturing, *Int. J. Appl. Technol., 5*(2), 188-197.

[Denomme 2007] Ryan C Denomme, Zhao Lu & Sylvain Martel (2007). A Microsensor for the Detection of a Single Pathogenic Bacterium Using Magnetotactic Bacteria-based Bio-carriers: Simulations and Preliminary Experiments, *Conf Proc IEEE Eng Med Biol Soc. 1*, 99-100.

[Ducheyne 1977] P. Ducheyne, P. De Meester, E. Aernoudt, M. Martens, & J. C. Mulier

(1997). Influence of a functional dynamic loading on bone ingrowth into surface pores of orthopedic implants, *Journal of Biomedical Materials Research 11*, 811-838.

[Duracher 2004] David Duracher, Raphael Veyret, Abdelhamid Elaıssari & Christian Pichot (2004), Adsorption of bovine serum albumin protein onto amino-containing thermosensitive core-shell latexes, *Polym Int, 53,* pp 618–626.

[Emr 2005] Sally A. Emr & Alexander M. Yacynych (2005). Use of polymer films in amperometric biosensors, *Electroanalysis, 7*(10), 913-923

[Fadda 1998] Fadda M, Marcacci M, Toksvig-Larsen S, Wang T, & Meneghello R (1998). Improving accuracy of bone resections using robotic tool holder and a high speed milling cutting tool, *J Med Eng Technol 22*(6), 280–284.

[Fang 2005] Zhibin Fang, Binil Starly, Ali Shokoufandeh, William Regli & Wei Sun (2005). A Computer-aided Multi-scale Modeling and Direct Fabrication of Bone Structure, *Computer-Aided Design & Applications, 2*(5), 627-634.

[Fouladi 2007] Jaouad El Fouladi, Zhao Lu, Yvon Savaria & Sylvain Martel (2007). An Integrated Biosensor for the Detection of Bio-entities Using Magnetotactic Bacteria and CMOS Technology, *Proceedings of the 29th Annual International Conference of the IEEE EMBS Cit é Internationale,* Lyon, France.

[Fujii 2002] Teruo Fujii (2002). PDMS-based microfluidic devices for biomedical applications, *Microelectronic Engineering, 61-62,* 907-914

[Gai 1992] H. Gai & G.A. Voth (1992). A computer simulation method for studying the ablation of polymer surface by ultraviolet laser radiation, *J. Appl. Phys. 71*(3), 1415–1420.

[Gerard 2002] Manju Gerard, Asha Chaubey & B. D. Malhotrab (2002). Application of conducting polymers to biosensors, *Biosensors and Bioelectronics,17*(5), 345-359.

[Galantucci 1998] L.M. Galantucci (1998). Excimer laser cutting: experimental characterization and 3D numerical modeling for polyester resins, *Ann. CIRP, 47*(1), 141-144.

[Griffith 1996] Griffith, A. Glidle & J. M. Cooper (1996). Probing enzyme polymer biosensors using X-ray photoelectron spectroscopy: Determination of glucose oxidase in electropolymerised films, *Biosensors and Bioelectronics, 11*(6-7), 625-631.

[Griffith 1997] Alun Griffith, Andrew Glidle, Graham Beamson & Jonathan M. Cooper (1997). Determination of the Biomolecular Composition of an Enzyme−Polymer Biosensor, *J. Phys. Chem. B, 101*(11), 2092-2100.

[Harrysson 2001] Harrysson Ola L.A (2001). *Customization of Knee Implants and Optimization of Bone-Implant Interface*. Ph.D Thesis, University of Central Florida,

[Harrysson 2003] Harrysson Ola L.A, Cormier Denis R, Marcellin-Little Denis J & Jajal Ketan (2003). Rapid prototyping for treatment of canine limb deformities, *Rapid Prototyping Journal, 9*(1), 37-42.

[Harrysson 2007] Ola L. A. Harrysson, Yasser A. Hosni & Jamal F. Nayfeh (2007). Custom-designed orthopedic implants evaluated using finite element analysis of patient-specific computed tomography data: femoral-component case study, *BMC Musculoskeletal Disorders, 8*, 91.

[Hieu 2002] Hieu L.C., Bohez E., Phien H.N. & et al (2002). Design and manufacturing of personalized and standardized templates for cranioplasty applications, *IEEE ICIT*, Bangkok, Thailand.

[Ishihara 1999] Kazuhiko Ishihara, Kikuko Fukumoto, Yasuhiko Iwasaki & Nobuo Nakabayashi (1999). Modification of polysulfone with phospholipid polymer for improvement of the blood compatibility. Part 2. Protein adsorption and platelet adhesion, *Biomaterials,20*, 1553-1559.

[Jajal 2003] Ketankumar R. Jajal (2003). *Custom design and manufacturing of canine knee implants*. Master thesis, North Carolina State University.

[Kahiert 1992] H.-J. Kahiert, U. Sarbach, B. Burghardt & B. Klimt (1992). Excimer Laser Illumination and Imaging Ontics for Controlled Microstructure Generation, *SPIE Excimer Lasers 1835*(1992), 110–118.

[Khine 2005] M. Khine, A. Lau, C. Ionescu-Zanetti, J. Seo & L. P. Lee (2005). A single cell electroporation chip, *Lab on a Chip, 5*, 38-43.

[Klank 2002] Henning Klank, Jörg P. Kutter & Oliver Geschke (2002). CO_2-laser micromachining and back-end processing for rapid production of PMMA-based microfluidic systems, *Lab Chip, 2*, 242-246.

[Klenkler 2005] B.J. Klenkler, M. Griffith, C. Becerril, J.A. West-Mays & H. Sheardown (2005). EGF-grafted PDMS surfaces in artificial cornea applications, *Biomaterials*, *26*(35), 7286-7296.

[Krajnovich 1997] D. Krajnovich (1997). Near-threshold photoablation characteristics of polyimide and ploy (ethylene terephthalate), *J. Appl. Phys. 82*, 427.

[Küper 1989] S. Küper & M. Stuke (1989). UV-excimer-laser ablation of polymethylmethacrylate at 248 nm: Characterization of incubation sites with Fourier transform IR- and UV-Spectroscopy, *Appl. Phys. A 49*, 211-215.

[Lee 1996] Y . S . LEE, & T.C. CHANG (1996). Machined surface error analysis for 5-axis machining, *International Journal of Production Research, 1996, 34*(1), 111-135.

[Lee 1997] LEE, Y. S. & JI, H.(1997). Surface interrogation and machining strip evaluation for 5-axis CNC die and mold machining, *International Journal of Production Research, 1997, 35*(1), 225- 252.

[Lee 2005] Lee S, Maronian N, Most SP & et al.(2005). Porous high-density polyethylene for orbital reconstruction, *Arch Otolaryngol Head Neck Surg 131*(5), 446-50.

[Lin 1997] Lin TW, Corvelli AA, Frondoza CG, Roberts, JC & Hungerford DS(1997). Glass peek composite promotes proliferation and osteocalcin production of human osteoblastic cells, *J Biomedical Materials Research, 36*(2), 37-144.

[LIU 2004] JAMES K. LIU, M.D., OREN N. GOTTFRIED, M.D. & et al. (2004). Porous polyethylene implant for cranioplasty and skull base reconstruction, *Neurosurg Focus 16*(3), Clinical Pearl 1.

[Lu 1997] Z. Lu and S. Martel (1997). CONTROLLED BIO-CARRIERS BASED ON MAGNETOTACTIC BACTERIA, *The 14th International Conference on Solid-State Sensors, Actuators and Microsystems*, Lyon, France.

[Martel 2006] Sylvain Martel, Charles C. Tremblay, Serge Ngakeng & Guillaume Langlois (2006). Controlled manipulation and actuation of micro-objects with magnetotactic bacteria, *APPLIED PHYSICS LETTERS,89*, 233904

[Matsunaga 1987] Tadashi Matsunaga & Shinji Kamiya (1987). Use of magnetic particles isolated from magnetotactic bacteria for enzyme immobilization, *Appl Microbiol Biotechnol,26*, 328-332.

[Matsunaga 2004] Tadashi Matsunaga, Yoshiko Okamura & Tsuyoshi Tanaka (2004). Biotechnological application of nano-scale engineered bacterial magnetic particles, *Journal of Materials Chemistry, 14*, 2099-2105.

[McMurray 2007] Amanda A McMurray, Zulfiqur Ali, Jan Kyselovik and et al.(2007). A Novel Point of Care Diagnostic Device: Impedimetric Detection of a Biomarker in Whole Blood, *Conf Proc IEEE Eng Med Biol Soc., 1*, 115-118.

[Mousa 2000] Weam F. Mousa, Masahiko Kobayashi, Shuichi Shinzato and etc.(2000). Biological and mechanical properties of PMMA-based bioactive bone cements, *Biomaterials, 21*(21), 2137-2146.

[Mutapcic 2003] Mutapcic E, Iovenitti P & Hayes JP (2003). Overlay error effects on polycarbonate structures produced by 248 nm UV laser ablation tool, *Proceedings of the 3rd Asia-Pacific Forum on Precision Surface Finishing and Deburring Technology*, Melbourne, Australia, 269-280.

[Mutapcic 2006] Mutapcic, E., Iovenitti, P. & Hayes (2006). A prototyping and micromachining CAD/CAM tool for excimer laser micromachining process, *Int J Adv Manuf Technol., 30*, 1076-1083

[Naessens 2003] Kris Naessens (2003). *Excimer laser ablation of microstructure in polymers for photonic application.* PhD dissertation, Universiteit Gent.

[Park 2002] Hun K. Park, Manuel Dujovny, Fernando G. Diaz & Murali Guthikonda (2002). Biomechanical properties of high-density polyethylene for pterional prosthesis, *Neurological Research,24*, 671-676.

[Park 2004] Kwideok Park, Gladius Lewis & Joon B. Park (2004). Ultra-High Molecular

Weight Polyethylene (UHMWPE), *Encyclopedia of Biomaterials and Biomedical Engineering, 1*(1), 1690-1696.

[Paterson 1999] C. Paterson, A.S. Holmes & R.W. Smith (1999). Excimer Laser Ablation of Microstructures: a Numerical Model, *Journal of Applied Physics, 86*(11), 6538-6547.

[Pokrandt 1997] Pokrandt P, Both A & Hekmat A (1997). Computer assisted surgery planning and robotics by orto MAQUET, *Proceedings of the 4th International Workshop on Rapid Prototyping in Medicine & Computer-Assisted Surgery,* Erlangen, Germany.

[Radke 2004] Stephen M. Radke & Evangelyn C. Alocilja (2004). Design and Fabrication of a Microimpedance Biosensor for Bacterial Detection, *IEEE SENSORS JOURNAL, 4*(4).

[Ramakrishna 2001] S. Ramakrishna, J. Mayer, E. Wintermantel & Kam W. Leong (2001). Biomedical applications of polymer-composite materials: a review, *Composites Science and Technology, 61*(9), 1189-1224.

[Ren 2005] Jun Ren, Michael Kelly & Lambertus Hesselink (2005). Laser ablation of silicon in water with nanosecond and femtosecond pulses, *Optics Letters, 30*(13).

[Ren 2009] Deyao Ren, Roger Narayn & Yuan-Shin Lee (2009), "Machined surface analysis in laser micromachining of biocompatible polymers for medical devices manufacturing", *Computer-Aided Design & Applications, 6*(6), 781-793.

[Ren 2009a] Deyao Ren, Roger Narayan & Yuan-Shin Lee (2009), "Laser micromachining and its application in manufacturing of micro medical devices" (working paper).

[Ren 2009b] Deyao Ren, Roger Narayan & Yuan-Shin Lee (2009), "Modeling of excimer laser micromachining and its application in machined surface error analysis" (working paper).

[Roberts 1997] Matthew A. Roberts, Joel S. Rossier, Paul Bercier & Hubert Girault (1997). UV Laser Machined Polymer Substrates for the Development of Microdiagnostic Systems, *Anal. Chem., 69*, 2035-2042

[Sachlos 2003] E. Sachlos & J.T. Czernuszka (2003). Making tissue engineering scaffolds work: review on the application of solid freeform fabrication technology to the production of tissue engineering scaffolds, *European Cells and Materials, 5*, 29-40.

[Salernitano 2003] E. Salernitano & C. Migliaresi (2003). Composite materials for biomedical applications: a review, *Journal of Applied Biomaterials & Biomechanics, 1*, 3-18.

[Sathasivam 1999] Sathasivam S, Walker PS, Pinder IM, Cannon SR & Briggs TWR (1999). Custom constrained condylar total knees using CAD-CAM, *The Knee, 6*, 49-53.

[Scharver 2004] Chris Scharver, Ray Evenhouse, Andrew Johnson & Jason Leigh (2004). Pre-surgical Cranial Implant Design using the PARIS™ Prototype， IEEE Virtual Reality, Chicago, IL, USA.

[Schmidt 1998] H. Schmidt, J. Ihlemann, B. Wolff-Rottke, K. Luther, & J. Troe (1998). Ultraviolet laser ablation of polymers: spot size, pulse duration, and plume attenuation effects explained, *J. Appl. Phys., 83*, 5458.

[Schuler 1999] D. Schuler & R. B. Frankel (1999). Bacterial magnetosomes: microbiology, biomineralization and biotechnological applications, *Appl Microbiol Biotechnol, 52*, 464-473.

[Simmons 2008] Anne Simmons, Ajay Devidas Padsalgikar, Lynn Marie Ferris & Laura Anne Poole-Warren(2008). Biostability and biological performance of a PDMS-based polyurethane for controlled drug release, *Biomaterials*, *29*(20), 2987-2995.

[Srinivasan 1986] R. Srinivasan, M. Smrtic & S. Babu (1986). Excimer laser etching of polymers, *J. Appl. Phy., 59*, 3861.

[Suwanprateeb 2006] J. Suwanprateeb & R. Chumnanklang (2006). Three-Dimensional Printing of Porous Polyethylene Structure Using Water-Based Binders, *J Biomed Mater Res Part B: Appl Biomater, 78B*, 138-145.

[Taylor 1987] Taylor, R. S., Singleton, D. L. & Paraskevopoulos, G.(1987). Effect of optical pulse duration on the XeCl laser ablation of polymers and biological tissue, *Applied Physics Letters, 50*(25), 1779-1781.

[Thoma 2000] Thoma W, Schuster C, Schuster L (2000). Custom-made knee endoprosthetics using subtraction data of 3-dimensional CT scans. A new approach, *Der Orthopade, 29*(7), 641-4

[Tsuruta 1993] T. Tsuruta, T. Hayashi, K. Kataoka, K. Ishihara & Y. Kimura (1993). *Biomedical Applications of Polymeric Materials*. CRC Press, Boca Raton, FL, USA.

[Turner 1989] Thomas M. Turner , Robert M. Urban, Dale R. Sumner, Anastasia K. Skipor, Jorge O. Galante, Bone ingrowth into the tibial component of a canine total condylar knee replacement prosthesis, *Journal of Orthopedic Research, 7*(6), 893-901.

[Verret 2006] DJ Verret. Implants (2006). *Soft Tissue, High-Density Porous Polyethylene (Medpor)*. Retrived Auguest 24, 2009, from http://www.emedicine.com.

[Wei 2009] Jianhua Wei, Toshio Igarashi, and et al.(2009). Influence of surface wettability on competitive protein adsorption and initial attachment of osteoblasts, *Biomed. Mater., 4*.

[Williams 1999] DF Williams (1999). *The Williams Dictionary of Biomaterials.* Liverpool,

UK: Liverpool University Press.

[Williams 2008] David F. Williams (2008). On the mechanisms of biocompatibility, *Biomaterials*, *299*(20), 2941-2953.

[Yang 2003] Yunzhi Yang, Renee Cavin & Joo L Ong (2003). Protein adsorption on titanium surfaces and their effect on osteoblast attachment, *Journal of Biomedical Materials Research Part A, 67A*(1), 344-349.

[Yang 2002] Zhongping Yang, Michael J. Ebert & James M. Anderson (2002). Branched polyethylene oxide terminated biomedical polymers and their use in biomedical devices, U. S. Patent 6,961,610, April 25, 2002.

[Zee 2001] Frank Zee & Jack W. Judy (2001). Micromachined polymer-based chemical gas sensor array, *Sensors and Actuators B, 72*, 120-128.

[Zhou 2005] Jun Zhou, Jiang Yuan, Xiaopeng Zang, Jian Shen & Sicong Lin (2005). Platelet adhesion and protein adsorption on silicone rubber surface by ozone-induced grafted polymerization with carboxybetaine monomer, Colloids and Surfaces B, *Biointerfaces*, *41*, 55–62.